



UNIVERSITY OF CAPE TOWN
IYUNIVESITHI YASEKAPA • UNIVERSITEIT VAN KAAPSTAD

Factors Influencing The Morphology Of Sea Ice

*A Dissertation in Fulfilment of the Requirements for the Degree of
Master of Science in Chemical Engineering*

Prepared By:

Boitumelo Matlakala

Supervisor:

Dr. Tokoloho Rampai

Co-supervisor:

A/Prof. Marcello Vichi



Date of submission: March 2022

The copyright of this thesis vests in the author. No quotation from it or information derived from it is to be published without full acknowledgement of the source. The thesis is to be used for private study or non-commercial research purposes only.

Published by the University of Cape Town (UCT) in terms of the non-exclusive license granted to UCT by the author.

Plagiarism Declaration

- I know that plagiarism is wrong. Plagiarism is to use another's work and pretend that it is my own.
- I have used the Harvard referencing system for citation and referencing. In this report, all contributions to, and quotation from, the work(s) of other people have been cited and referenced.
- This report is my own work, and it is in my own words (except where others are quoted).
- I have not allowed and will not allow anyone to copy my work with the intention of passing it off as their own work.

Boitumelo Matlakala

March 2022

Signed by candidate

Acknowledgements

“For I know the plans that I have for you, declares the Lord, plans for your welfare and peace and not for evil, to give you hope in your final outcome” - Jeremiah 29:11. Glory be to the Almighty God for He has carried me, and His words assured me when the journey was rocky.

I would like to thank my supervisor, Dr. Tokoloho Rampai, for making it possible for me to go on the 2019 SCALE Spring Cruise because this is where I was intrigued. Thank you for your guidance and support throughout. To Prof. Marcello Vichi, thank you for sharing knowledge and provision of funding. To Sharon, for tirelessly assisting with administrative issues, it is appreciated.

I would like to give special gratitude to Mr. Joachim Macke, from the Mechanical Workshop, for willing to assist with designs and equipment making. Thanks to the staff at X-Sight X-Ray. Thanks to Ameen Jakoet, Curwin Nomdoe, and Justin Pead for assisting whenever my equipment failed, as well as always checking in. To Siobhan, thank you for sharing knowledge and always willing to help. Research colleagues, Lisa, Felix, Tamuka, and Safiyyah, with whom deep, meaningful friendships were formed, thank you for your tireless assistance and availing yourselves for both research and personal support. Please continue being kind to each other, it goes a long way.

Special thanks to Nondumiso, Tebogo, Omphemetse, Ntokozo, Sindy and Sinazo, Takunda, Tsepang, the Pather and the Kumadiro families, for your love, prayers and consistent support.

I am grateful for the National Research Fund (Grant No. 118745) for making this study possible.

A huge gratitude to my family, baTlhaping ba ba tlhapang ka maswi ba tsaya tlhoa ba itshogore. Ke leboga go menagane ka thego ya lona. Le nkeme nokeng fa e sa le ke simolola dithutu tsa me. Jaaka papa a bua “Yo o re tshepisiseng, o a tshepagala”, a leina la Matlakala le itsege le tlotlomale. Go weditsewe bagaetsho!

Abstract

Due to the continuous melting of sea ice and rising sea levels, more studies are conducted on sea ice morphology and factors influencing the growth of ice. Sea ice is an integral part of the global climate system. It plays a vital role in the polar ecosystem, providing a habitat for organisms. Sea ice growth and behaviour has been observed to be largely affected by climate change and global warming. However, the consequences thereof, on sea ice extent and seasonal changes are still being studied.

Artificial sea ice experiments have been used as they offer an advantage of control and help isolate variables during sea ice growth. Additionally, *in-situ* experiments are expensive, and can present logistical difficulty for measuring these variables long term.

Factors such as growth dynamics, crystal texture and brine inclusions were investigated by variation of ambient temperature, starting artificial ocean salinity, reactor volume and the presence of microorganism' secretions: extracellular polymeric substances (EPS). Salinities of 10 psu, 20 psu, and 30 psu, were used at the following temperatures: -20°C, -10°C and -5°C.

The temperature and salinity data showed that the growth rate of ice, increases with the decreasing ambient temperature, decreasing starting artificial sea ice salinity, decreasing reactor volume, as well as in the presence of microorganisms' secretions. The cross-polarisation results revealed a decreasing percentage of granular texture with increasing starting artificial ocean salinity and increasing ambient temperature. Similarly, the same trend was observed for increasing reactor volume. In the presence of microorganisms, however, a blotchy granular and a disordered columnar texture were observed. An increase in artificial sea ice porosity due to brine inclusions was revealed by the micro-ct scanning data for an increasing starting artificial ocean salinity. Furthermore, overall porosity increased with decreasing ambient temperature and in the presence of microorganism secretion.

Table of Contents

	Page
Plagiarism Declaration	ii
Acknowledgements	iii
Abstract.....	iv
List of Tables	viii
List of Figures.....	xi
Glossary	xvii
Nomenclature.....	xviii
1 Introduction	1-1
1.1 Background.....	1-1
1.2 Problem Statement	1-2
1.3 Scope and Limitations.....	1-2
2 Literature Review.....	2-1
2.1 Sea ice formation	2-1
2.2 Crystallization	2-2
2.3 Sea ice texture and crystal structure.....	2-3
2.4 Temperature and Salinity profiles of sea ice.....	2-6
2.5 Brine channel evolution	2-10
2.6 Factors affecting sea ice texture and brine inclusions	2-13
2.6.1 The effect of ambient temperature on sea ice texture and sea ice crystal structure.....	2-13
2.6.2 The effect of salinity on sea ice texture and sea ice crystal structure.....	2-16
2.6.3 The effect of microorganisms secretions on sea ice texture and sea ice crystal structure.....	2-17
2.7 Artificial sea ice growth.....	2-19
2.7.1 Reactor size, shape and material of construction.....	2-20
2.7.2 Insulation.....	2-22
2.7.3 Mixing.....	2-22
2.8 Sea ice physical properties and growth dynamics.....	2-23

2.9	Analytical techniques of studying sea ice crystal structure	2-25
2.9.1	Cross Polarisation	2-25
2.9.2	X-ray Micro-Computed Tomography (μ CT)	2-27
3	Aim, Objectives and Key Questions	3-1
3.1	Aim and Objectives	3-1
3.2	Key Questions	3-1
4	Methodology	4-1
4.1	Experimental matrix and setup	4-1
4.2	The Experimental Procedure	4-3
4.2.1	Artificial sea ice growth procedure	4-3
4.2.2	Artificial sea ice sampling procedure	4-4
4.2.3	Ice Salinity and Temperature Profile Measurements	4-6
4.3	Analytical methods for crystal structure visualisation	4-6
4.3.1	Cross Polarisation	4-6
4.3.2	X-ray Micro-Computed Tomography (μ CT)	4-8
5	Results	5-1
5.1	Justification of mixing speed	5-1
5.2	Artificial sea ice growth dynamics	5-4
5.2.1	Method of analysis	5-4
5.2.2	Effects of varying the starting artificial ocean salinity on artificial sea ice growth dynamics	5-8
5.2.3	Effects of varying ambient temperature on artificial sea ice growth dynamics	5-13
5.2.4	Effects of varying reactor volume on artificial sea ice growth dynamics	5-17
5.2.5	Effects of the presence of EPS on artificial sea ice growth dynamics	5-21
5.3	Artificial sea ice textural analysis	5-25
5.3.1	Method of analysis	5-25
5.3.2	Effect of varying the starting artificial ocean salinity on artificial sea ice crystal structure	5-28
5.3.3	Effect of varying the ambient temperature on artificial sea ice crystal structure	5-31
5.3.4	Effect of varying the reactor volume on artificial sea ice crystal structure	5-35
5.3.5	Effect of the presence of EPS addition on artificial sea ice crystal structure	5-38
5.4	Artificial sea ice brine analysis	5-41
5.4.1	Method of analysis	5-41
5.4.2	Effect of varying the starting artificial ocean salinity on artificial sea ice porosity	5-44

5.4.3	Effect of varying the ambient temperature on porosity.....	5-48
5.4.4	Effect of the presence of EPS addition on porosity.....	5-51
5.5	Analysis of artificial sea ice porosity computed from micro-CT scanning data vs. Frankenstein & Garner (1967) equations.....	5-56
5.5.1	Effect of varying the starting artificial ocean salinity on artificial sea ice porosity.....	5-57
5.5.1	Effect of varying the ambient temperature on porosity.....	5-60
6	Overall Discussion	6-1
6.1	Varying starting artificial ocean salinity.....	6-1
6.2	Varying ambient temperature.....	6-2
6.3	Varying reactor volume	6-4
6.4	Presence of EPS	6-4
6.5	Theoretical vs. experimental methods for brine analysis	6-6
7	Conclusions and Recommendations	7-1
8	References.....	a
	Appendices	i
A.	Study Ethics Clearance.....	i
B.	Standard Operating Procedures.....	j
B. 1	Artificial sea ice growth	j
B. 2	Reactor Insulation.....	k
B. 3	Artificial sea ice sampling procedure	m
C.	Thermodynamics and Physical Properties of Artificial Sea Ice	o
D.	Salinity data	q
E.	Cross polarisation	t
F.	CT scans	w
G.	Calculations with Frankenstein & Garner equations	z

List of Tables

Table 2.1 Textural classification by size and grain shape (adapted from Eicken and Lange (1989))	2-5
Table 2.2 Comparison of reactors used for artificial sea ice growth experiments from literature	2-21
Table 4.1 Experimental matrix labelled alphabetically for the conducted experiments	4-1
Table 5.1 Summary of findings from the Temperature time graph showing the growth dynamics for ice grown at -10°C from a solution of starting artificial ocean salinity of 10 psu.	5-7
Table 5.2 Summary of findings from the Temperature time graphs showing the growth dynamics for ice grown at -10°C from solutions of starting artificial ocean salinities of 10 psu, 20 psu and 30 psu.	5-9
Table 5.3 Summary of findings from the Temperature time graphs showing the growth dynamics for ice grown at -20°C and -10°C from solutions of starting artificial ocean salinity of 30 psu.....	5-14
Table 5.4 Summary of findings from the Temperature time graphs showing the growth dynamics for ice grown from the 3 L and 30 L reactor at -20°C and starting artificial ocean salinity of 30 psu.....	5-18
Table 5.5 Summary of findings from the Temperature time graphs showing the growth dynamics for ice grown at -10°C from solutions of starting artificial ocean salinity of 30 psu with and without EPS.	5-22
Table 5.6 Fraction of the artificial sea ice texture and the corresponding crystal size for samples obtained at -20 °C from a solution of starting artificial ocean salinity of 10 psu for 0 rpm stirring.	5-27
Table 5.7 Fraction of the artificial sea ice texture and the corresponding crystal size for samples obtained at -10 °C from solutions of starting artificial ocean salinities of 10 psu, 20 psu and 30 psu.....	5-30
Table 5.8 Fraction of each ice texture and corresponding crystal size for samples obtained from ice grown from solutions of starting artificial ocean salinity of 30 psu at -20°C, -10°C and -5°C.....	5-34

Table 5.9 Fraction of each ice texture and corresponding crystal size for samples grown from a 3 L and 30 L reactor at -20°C from starting artificial ocean salinity of 30 psu. .5-37	
Table 5.10 Fraction of each ice texture and corresponding crystal size for samples obtained at -10 °C from solutions of starting artificial ocean salinity of 30 psu with and without EPS.....5-40	
Table 5.11 Size description of brine and air inclusions for the top part of ice grown at -10°C from a solution of starting artificial ocean salinity of 10 psu.....5-43	
Table 5.12 Size description of brine and air inclusions for the top part of ice grown at -10°C from solutions of starting artificial ocean salinities of 10 psu, 20 psu, and 30 psu. 5-46	
Table 5.13 Size description of brine and air inclusions for the top part of ice grown from solutions of starting artificial ocean salinity of 30 psu at -20°C, -10°C, and -5°C... 5-50	
Table 5.14 Size description of brine and air inclusions for the top part of ice grown from solutions of starting artificial ocean salinity of 30 psu at -10°C with and without EPS.5-54	
Table D. 1 Salinity measurements for ice grown at -10°C from a solution of 10 psuq	
Table D. 2 Salinity measurements for ice grown at -10°C from a solution of 20 psuq	
Table D. 3 Salinity measurements for ice grown at -10°C from a solution of 30 psuq	
Table D. 4 Salinity measurements for ice grown at -20°C from a solution of 30 psu r	
Table D. 5 Salinity measurements for ice grown at -5°C from a solution of 30 psu r	
Table D. 6 Salinity measurements for ice grown at -10°C from a 30 psu solution with EPS.... r	
Table D. 7 Salinity measurements for ice grown from a 30 L reactor at -20°C from a solution of 30 psu s	
Table G. 1 Definitions of variables used in the calculations of brine, air and ice volumez	
Table G. 2 Equations used to calculate the artificial sea ice brine volume developed by Frankenstein and Garner (1967).....Z	

Table G. 3 Equations used in Table G. 5 for brine, air and ice volume calculations	aa
Table G. 4 Constants used for calculating $F_3(T)$, the constant used for brine volume calculation (Cox and Weeks, (1982))	aa
Table G. 5 The illustration of normalising bulk sea ice salinities (Cox and Weeks, 1988)	aa
Table G. 6 The table used to calculate the brine, air and ice volume for ice grown at -10°C from an artificial ocean salinity of 10 psu (Cox and Weeks, 1982)	bb
Table G. 7 The table used to calculate the brine, air and ice volume for ice grown at -10°C from an artificial ocean salinity of 20 psu (Cox and Weeks, 1982)	bb
Table G. 8 The table used to calculate the brine, air and ice volume for ice grown at -10°C from an artificial ocean salinity of 30 psu (Cox and Weeks, 1982)	bb
Table G. 9 The table used to calculate the brine, air and ice volume for ice grown at -20°C from an artificial ocean salinity of 30 psu (Cox and Weeks, 1982)	cc
Table G. 10 The table used to calculate the brine, air and ice volume for ice grown at -10°C from an artificial ocean salinity of 30 psu (Cox and Weeks, 1982)	cc
Table G. 11 The table used to calculate the brine, air and ice volume for ice grown at -5°C from an artificial ocean salinity of 30 psu (Cox and Weeks, 1982)	dd
<i>Table G. 12. Data for overall porosity of artificial sea ice for varying starting artificial ocean salinity computed from FG equations and ct-scan data</i>	<i>ee</i>
Table G. 13 Data for overall porosity of artificial sea ice for varying ambient temperature computed from FG equations and CT-scan data.	ff

List of Figures

Figure 2-1 Sea ice growth and formation. A - Frazil ice (Garcia, 2017), B - Nilas ice (Nilas Sea ice, 2016), C - Pancake ice (Garcia, 2017), and D - Consolidated ice (Koeng, 2019).	2-2
Figure 2-2 Schematic showing ice textures, growth conditions and typical winter temperature and salinity profiles for first-year sea ice (adapted from Petrich and Eicken, 2017).	2-4
Figure 2-3 Normalised salinity curves. A show a C-type curve where ice salinities are high at the top and bottom of the sample. B shows an S-type curve where salinities are high at the top, remain constant or decrease towards the bottom. C shows an opposite of the S-type, the ?-type. D shows the I-type curve with salinities remaining almost constant throughout the sample taken from Eicken (1992).	2-8
Figure 2-4 A shows sea ice skeletal layer taken from (Løset et al., 2006) and B shows the sea ice core showing (1) feeder channel and (2) brine tube extending outwards taken from (Kovacs, 1996).	2-10
Figure 2-5 Vertical (V) and horizontal (H) thin sections obtained from cross polarisation imaging showing sample at the end of growth (14 November), warming period (17 November), and cooling period (20 November) in the current, quiet and biochemical tank (Tison et al., 2002).	2-14
Figure 2-6 Paracetamol crystals grown at (a) 3°C and (b) 47°C (Shekunov et al., 1996) ...	2-15
Figure 2-7 (A) shows first-year ice and (B) shows multi-year ice taken from Timco and Weeks (2010).	2-16
Figure 2-8 Microscope images of artificial ice grown at -10 °C. A and B show ice texture at low magnification under polarised light, C and D with contrast staining, and E and F showing pore structure at high magnification. A, C and E was EPS free while, B, D and F had EPS added. Sourced from (Krembs et al., 2011)).	2-18
Figure 2-9 Heat fluxes during ice growth - 1D-approach (Wiese, 2012).	2-23
Figure 2-10 The temperatures recorded by the thermistors as function of time for sea ice experiments performed at -20°C ambient temperature, adapted from Wettlaufer et al. (1997)	2-24

Figure 2-11 Cross polarisation images of ice grown at 24 psu saline water with (a) showing the vertical and (b) showing the horizontal section, taken from Wei et al. (2020).2-26

Figure 2-12 Three-dimensional visualisation of sea ice (A) showing all brine channels (B) showing brine channels by volume where the one greater than 0.0337 mm³ are in green, the channels between 0.0067 mm³ and 0.0337 mm³ are in orange, and channels less than 0.00067 mm³ are blue (image adapted from Lieb-lappen (2016))2-28

Figure 4-1 Experimental set-up of artificial sea ice growth in the 3 L reactor with temperature probes installed (the 30 L set-up was similar, with 13 temperature probes installed)4-3

Figure 4-2. Top view of reactor after ice growth experiments showing where ice specimen were sampled from the reactor.....4-5

Figure 4-3 Thermal macrotome set-up showing a hot nichrome wire before sample thin sectioning.4-7

Figure 4-4 Micro-CT scanning set-up with the scanning chamber inside the scanner, the cooling bath on the floor and the user computers.4-9

Figure 5-1 Visual results of ice grown at -20°C from a 10 psu solution at (A) 0 rpm, (B) 800 rpm and (C) 1800 rpm stirring speed.5-2

Figure 5-2 Salinity profiles for ice grown from a solution of 10 psu at -20°C for 0 rpm, 800 rpm and 1800 rpm stirring speed.5-3

Figure 5-3 Reactor schematic showing the arrangement of temperature probes5-4

Figure 5-4 Temperature time graph showing the growth dynamics for ice grown at -10°C from a solution of starting artificial ocean salinity of 10 psu.....5-6

Figure 5-5 Temperature profiles for ice grown at -10°C from solutions of starting artificial ocean salinities of 10 psu, 20 psu, and 30 psu.5-10

Figure 5-6 Salinity profiles for ice grown at -10°C from solutions of starting artificial ocean salinities of 10 psu, 20 psu, and 30 psu.5-11

Figure 5-7 Temperature profiles for ice grown from solutions of starting artificial ocean salinity of 30 psu at -20°C, -10°C, and -5°C at the end of 16 hours.5-15

Figure 5-8 Salinity profiles for ice grown at -20°C, -10°C, and -5°C from solutions of starting artificial ocean salinity of 30 psu at the end of 16 hours.5-16

Figure 5-9 Temperature profiles for ice grown from solutions of starting artificial ocean salinity of 30 psu at -20°C from a 3 L and 30 L reactor.....	5-19
Figure 5-10 Salinity profiles for ice grown from solutions of starting artificial ocean salinity of 30 psu at -20°C from a 3 L and 30 L reactor.....	5-20
Figure 5-11 Temperature profiles for ice grown at -10°C from solutions of starting artificial ocean salinity of 30 psu with and without EPS.....	5-23
Figure 5-12 Salinity profiles for ice grown at -10°C from solutions of starting artificial ocean salinity of 30 psu with and without EPS.	5-24
Figure 5-13 Cross polarisation results of ice grown at -20°C from a 10 psu solution showing the (A) process of crystal measurement and (B) the corresponding stratigraphy diagram.	5-25
Figure 5-14 Graph illustrating ice textures and corresponding mean crystal sizes for ice grown at -20°C from a solution of starting artificial ocean salinity of 10 psu for 0 rpm stirring.	5-28
Figure 5-15 Stratigraphy diagrams for ice grown at -10°C from solutions of starting artificial ocean salinities of 10 psu, 20 psu and 30 psu.	5-29
Figure 5-16 Graph illustrating ice textures and corresponding mean crystal sizes for ice grown at -10°C from solutions of starting artificial ocean salinities of 10 psu, 20 psu and 30 psu.	5-31
Figure 5-17 Stratigraphy diagrams for ice grown from solutions of starting artificial ocean salinity of 30 psu at -20°C, -10°C and -5°C (thickness of ice at the end of 16 hours shown by red dashed-line)	5-32
Figure 5-18 Graph illustrating ice textures and corresponding mean crystal sizes for ice grown from solutions of starting artificial ocean salinity of 30 psu at -20°C, -10°C and -5°C	5-35
Figure 5-19 Stratigraphy diagram of ice grown at -20°C from solutions of starting artificial ocean salinity of 30 psu from a 3 L and 30 L reactor (with the red line showing the thickness of the 30 L sample after 16 hours).	5-36
Figure 5-20 Graph illustrating ice textures and corresponding mean crystal sizes for ice grown at -20°C and starting artificial ocean salinity of 30 psu from a 3 L and 30 L reactor.	5-37

Figure 5-21 Stratigraphy diagrams for ice grown from solutions of starting artificial ocean salinity of 30 psu at -10°C with and without EPS.	5-39
Figure 5-22 Graph illustrating ice textures and corresponding mean crystal sizes ice grown at -10°C from a solution of starting artificial ocean salinity of 30 psu with and without EPS.....	5-40
Figure 5-23 Visual result showing the process of brine and air pockets analysis from CT-scanning for ice grown at -10°C from a 30 psu solution with (A) and (B) showing the brine, air and ice in white, black and grey respectively, and (C) and (D) showing brine volume through colour coding.....	5-41
Figure 5-24 Micro-CT scan visuals for the (A) top and (B) bottom section of ice grown at -10°C from a solution of 10 psu starting artificial ocean salinity.	5-42
Figure 5-25. Artificial sea ice porosity of ice grown at -10°C from a solution of starting artificial ocean salinity of 10 psu.	5-44
Figure 5-26 Micro-CT scan visuals for the top part of ice grown at -10°C from solutions of starting artificial ocean salinities of (A) 10 psu, (B) 20 psu, and (C) 30 psu.....	5-45
Figure 5-27. Porosity of artificial sea ice grown at -10°C from solutions of starting artificial ocean salinities of 10 psu, 20 psu, and 30 psu.	5-47
Figure 5-28 Micro-CT scan visuals for the top part of ice grown from solutions of starting artificial ocean salinity of 30 psu at (A) -20°C, (B) -10°C, and (C) -5°C.....	5-49
Figure 5-29. Porosity of artificial sea ice grown from solutions of starting artificial ocean salinity of 30 psu at -20°C, -10°C, and -5°C.....	5-51
Figure 5-30 Micro-CT scan visuals for the top part of ice grown at -10°C from solutions of starting artificial ocean salinity of 30 psu (A) without EPS, (B) with EPS.....	5-52
Figure 5-31 Porosity of artificial sea ice grown from solutions of starting artificial ocean salinity of 30 psu at -10°C with and without EPS.	5-55
Figure 5-32 Theoretical porosity of artificial sea ice grown at -10°C from solutions of starting artificial ocean salinities of 10 psu, 20 psu, and 30 psu calculated from FG methods.	5-58
Figure 5-33 Graph showing the comparison between artificial sea ice porosity computed from micro-CT data and from Frankenstein and Garner (FG) methods for ice grown at -10°C from solutions of varying starting artificial ocean salinity.	5-59

Figure 5-34 Theoretical porosity of artificial sea ice grown from solutions of starting artificial ocean salinity of 30 psu at -20°C, -10°C, and -5°C calculated from Frankenstein and Garner (FG) methods.	5-60
Figure 5-35 Graph showing the comparison between artificial sea ice porosity computed from micro-CT data and from Frankenstein and Garner (FG) methods for ice grown from solutions of starting artificial ocean salinity of 30 psu at varying ambient temperatures.	5-61
Figure B. 1 Experimental set-up showing reactor side and bottom insulation	j
Figure B. 2 (A) Top view of reactor after ice growth experiments showing where ice specimen was sampled from the reactor (B) Top view of artificial sea ice after growth	m
Figure C. 1 Temperature time graphs for ice grown at -10°C from solutions of starting artificial ocean salinities of 10 psu, 20 psu and 30 psu	o
Figure C. 2 Temperature time graphs for ice grown from solutions of starting artificial ocean salinity of 30 psu at -20 °C and -10°C.....	o
Figure C. 3 Temperature time graphs for ice grown from solutions of starting artificial ocean salinity of 30 psu from a 30 L and 3 L reactor at -20 °C.	p
Figure C. 4 Temperature time graphs for ice grown from solutions of starting artificial ocean salinity of 30 psu at -10 °C with and without EPS.	p
Figure E. 1 Cross polarisation results of samples grown at -10°C from solutions of starting artificial ocean salinities of (A) 10 psu, (B) 20 psu, and (C) 30 psu	t
Figure E. 2 Cross polarisation results of samples grown from solutions of starting artificial ocean salinity of 30 psu at (A) -20°C, (B) -10°C, and (C) -5°C.....	t
Figure E. 3 Cross polarisation results of samples grown at -20°C from solutions of starting artificial ocean salinity of 30 psu from a (A) 3 L and (B) 30 L reactor.	u
Figure E. 4 Cross polarisation results of samples grown from solutions of starting artificial ocean salinity of 30 psu at -10°C (A) with and (B) without EPS	v

Figure F. 1 Micro-CT scan visuals for the top part of ice grown at -10°C from solutions of starting artificial ocean salinities of (A) 10 psu, (B) 20 psu, and (C) 30 psu..... w

Figure F. 2 Micro-CT scan visuals for the bottom part of ice grown at -10°C from solutions of starting artificial ocean salinities of (A) 10 psu, (B) 20 psu, and (C) 30 psu..... w

Figure F. 3 Micro-CT scan visuals for the top part of ice grown from solutions of starting artificial ocean salinity of 30 psu at (A) -20°C , (B) -10°C , and (C) -5°C x

Figure F. 4 Micro-CT scan visuals for the bottom part of ice grown from solutions of starting artificial ocean salinity of 30 psu at (A) -20°C and (B) -10°C x

Figure F. 5 Micro-CT scan visuals for the top part of ice grown at -10°C from solutions of starting artificial ocean salinity of 30 psu (A) without EPS, (B) with EPS..... y

Figure F. 6 Micro-CT scan visuals for the bottom part of ice grown at -10°C from solutions of starting artificial ocean salinity of 30 psu (A) without EPS, (B) with EPS..... y

Figure G. 1 Graph showing the relationship between the relative volume of brine, air, and ice generated as per the values inputted in the Table G. 6..... ee

Figure G. 2 Graph of overall porosity of artificial sea ice for varying starting artificial ocean salinity computed from FG equations and CT-scan data. ff

Figure G. 3 Graph of overall porosity of artificial sea ice for varying ambient temperature computed from FG equations and CT-scan data gg

Glossary

Ambient Temperature	Air or atmospheric temperature in the laboratory at which artificial sea ice was grown
Anthropogenic	Human activities resulting in environmental pollution
Diatoms	Single-celled algae
Detritus	Organic matter derived from decomposition of organisms
Congelation	Coming together and taking shape to form a solid whole
Columnar ice	Uniform structured ice showing pronounced elongation parallel to the direction of heat flow
Consolidated ice	A solid whole ice with a uniform surface
Constitutional supercooling	This is the cooling of water below its freezing point without any phase change due to more rapid diffusion of heat than salt
Convection	The transfer of heat and salt by the tendency of hotter, less dense particles rising to the top in the ice layer and cold, dense particles sinking to the water underneath
Cross polarisation	The crystal structure visualisation technique that uses cross-polarised sheets and camera for imaging
Cryoprotectants	Substance preventing a tissue or cell from damage due to freezing
Frazil ice	Fine needle-like new ice suspended on the surface of water
Granular ice	Upper most section of ice formed by ice granules of frazil ice and snow
Ice extent	Total area or region covered by ice
Ice nucleation	Process of formation of small ice crystal embryos on membrane proteins that act as nucleation sites

In-situ temperature	Temperature of the ice layer
Nilas	Thin elastic layer of ice, formed on a quiet surface by direct freezing or from grease ice, which bends on waves and swells.
Pancake ice	Disk-shaped ice floes with raised rims due to the pieces striking against one another
Scanning Temperature	Temperature at which the cooling chamber was maintained at during scanning artificial sea ice samples
Thermohaline circulation	Temperature-dependent pattern of seawater movement, resulting in changes in salt content and density

Nomenclature

EPS:	Extracellular Polymeric Substances
IPCC:	International Panel on Climate Change
PSU:	Practical Salinity Units

1 Introduction

1.1 Background

Sea ice is an integral part of the global climate system. Its physical qualities, such as having the bright surface, enables heat transfer, thereby, keeping the ocean and polar regions cool. Sea ice has attracted attention with the observed continuous melting of sea ice and rising sea levels, attributed to global warming due to anthropogenic activities. The decreasing sea ice extent has been of concern and attracted more attention towards the study of the ocean and sea ice (International Panel on Climate Change, 2014). This is reported to have been caused by anthropogenic climate change experienced over the past years to date. The changing ice composition has also been observed and it's attributed to ice being more seasonal than perennial (International Panel on Climate Change, 2014), which will have effects on the feedback mechanism of the Earth's climate system (Middleton et al., 2016).

Investigating the relationship between sea ice, the ocean and the atmosphere will provide more understanding of the feedback mechanism of the climate system and thermohaline circulation, leading to more understanding of the factors affecting sea ice morphology. Previous sea ice studies have focused on the Arctic Ocean and its ice morphology, while little is known about the Antarctic Ocean. The main reported difference between the Arctic and Antarctic Sea ice formation is the influence of atmospheric conditions. The Antarctic sea ice grows under turbulence from wind and wave actions, while, the Arctic ice grows under calm conditions (Weeks and Ackley, 1982). Thus, making it important to investigate the effect of different growth conditions on sea ice texture.

1.2 Problem Statement

Generally, sea ice microstructure has been investigated with the focus being on thermal evolution of brine and gas inclusions, mainly of the Arctic Sea ice. The gap identified lies in the limited study of how different growth conditions such as temperature and salinity, as well as the presence of microorganisms in the ice matrix, affect the sea ice crystal structure and texture. Furthermore, there are equations developed to estimate brine and gas volume in sea ice (Frankenstein and Garner, 1967). However, there is uncertainty with the use of these equations due to the conflicting assumptions made by researchers to back up the development of the calculations (Assur, 1960; Frankenstein and Garner, 1967; Cox and Weeks, 1982).

Research involving sea ice is generally challenging in that sea ice is seasonal, and it is logistically difficult and expensive to obtain (Cox and Weeks, 1974). In addition, it is difficult to isolate variables in such a way that enhances the investigation of a particular growth aspect of interest *in-situ*. It is, therefore, necessary to have laboratory-based experiments to allow isolation of variables, and study how they affect sea ice growth dynamics and properties. Also, this would allow for a better understanding of how different growth conditions affect sea ice properties, and how in turn these properties feedback into the environment.

1.3 Scope and Limitations

In this report, sea ice morphology will be studied by simulating the Arctic Sea ice since ice will be grown in the laboratory with no simulation of wind and wave actions. In addition, the investigation will be limited to small volume reactors (3 L and 30 L), and the small range of varying ambient temperature (-20°C to -5°C) and salinity (10 psu, to 30 psu). The properties under investigation are limited to sea ice texture, brine inclusions, and sea ice growth dynamics such as the freezing point, time taken to freeze, and average growth rate.

2 Literature Review

The IPCC report (International Panel on Climate Change, 2014) states that the Arctic sea ice extent has been decreasing over the past few years due to anthropogenic climate change. Sea ice composition is also reported to be changing as the ice becomes seasonal rather than perennial, with large amounts of first-year ice observed compared to multi-year ice (Maslanik *et al.*, 2011; Weeks, 2010). The growth and decay processes of sea ice leads to brine expulsion into the seawater, thereby, increasing the seawater salt concentration. This causes disturbances to the global thermohaline circulation and the movement of seawater due to density changes. It is therefore important to study sea ice texture and morphology in order to understand the effects of different growth conditions such as temperature, salinity and presence of microorganisms in brine channels, on sea ice growth, ocean circulation and on the interaction between the ocean and the atmosphere.

2.1 Sea ice formation

Sea ice formation is as a result of cooling of the surface of the ocean to temperatures around -1.8°C in seawater having salinities around 34 ppt (Thomas, 2017; Weeks and Ackley, 1982). The freezing process can occur in calm or turbulent sea conditions such as in the Arctic or Antarctic oceans respectively. In calm conditions, a thin skim of large crystals is formed quickly on the water surface, while, free-floating crystals are formed in the turbulent conditions due to wind and wave actions (Løset *et al.*, 2006). The latter leads to the formation of a non-coherent ice sheet on the sea surface. This is mixed and dispersed downwards into the sea, exposing more seawater to the cooler atmospheric temperature to initiate freezing (Doble *et al.*, 2003). Accumulation of these initial ice crystals (typically less than 2 mm in diameter) is called frazil ice and can be seen in Figure 2-1 A. The crystals later freeze together to form a thin ice layer called nilas (Figure 2-1 B) due to the calm atmospheric conditions. Conversely, the abrasive

crystal action observed because of turbulence, enhances disk-shaped ice growth. Thereafter, crystals agglomerate to form pancake ice as shown in Figure 2-1 C (Løset *et al.*, 2006). Pancakes are initially a few centimetres in diameter and grow to more than 50 cm in thickness (Doble *et al.*, 2003). Wind actions and ocean swells penetrating deep in the ocean brings about the bumping and grinding of pancakes against each other, eventually congealing to form consolidated ice, which can be seen in Figure 2-1 D (Petrich and Eicken, 2017).

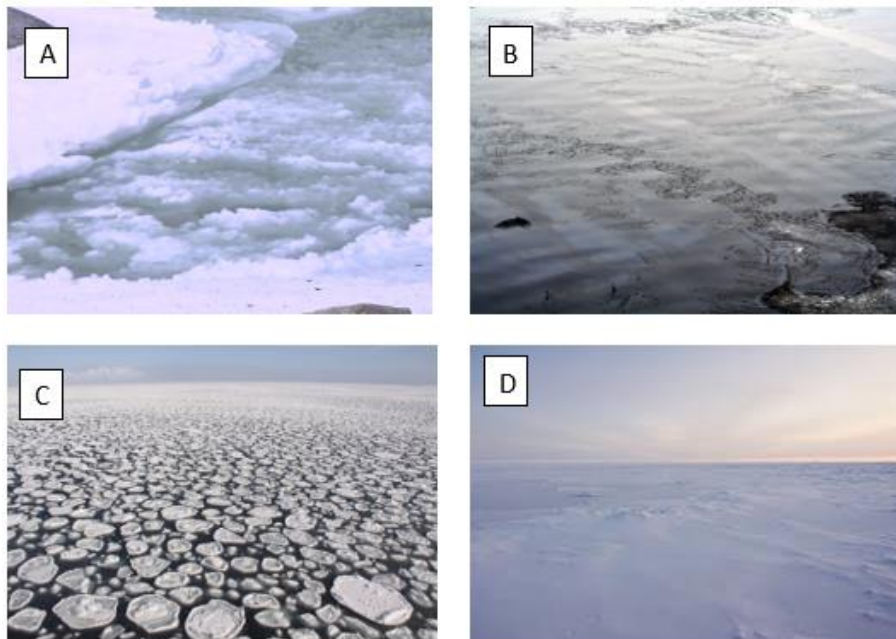


Figure 2-1 Sea ice growth and formation. A - Frazil ice (Garcia, 2017), B - Nilas ice (Nilas Sea ice, 2016), C - Pancake ice (Garcia, 2017), and D - Consolidated ice (Koeng, 2019).

2.2 Crystallization

Nucleation and crystal growth are two phase change phenomena that bring about the formation of crystals from a solution or melt. Crystallisation depends on supersaturation induced by either one of the following disturbances from equilibrium; increased solute concentration, decreased temperature, or increased pressure of the liquid (Genck, 1969; Lewis *et al.*, 2015).

Nucleation is the process of crystal nuclei formation from a solution or melt (Lewis *et al.*, 2015). There are two types of nucleation, primary and secondary nucleation. Primary nucleation occurs when crystals are formed from a clear solution, while secondary nucleation is as a result of prior presence of the same crystals, referred to as parent crystals. Primary nucleation is further divided into two types, homogeneous and heterogeneous. The latter is induced by the presence of foreign particles such as dust or dirt forming initial points of nucleation, while the former is a spontaneous process where solute particles cluster together in a solution.

Once crystal nuclei have formed and stabilised, given the favourable conditions, crystals start growing. Genck (1969) states that for crystals to grow, the solute particles must diffuse to the crystal surface and be integrated into the crystal lattice (Genck, 1969; Lewis *et al.*, 2015). Depending on the solubility of compounds, either diffusion of particles to the surface or surface integration can be a growth rate determining factor. Surface integration does not limit the growth rate of highly soluble compounds. Likewise, the growth rate of poorly soluble compounds is not limited by diffusion but by surface integration.

2.3 Sea ice texture and crystal structure

The typical textural structure of sea ice is made up of three layers; granular, transitional and columnar (Tucker *et al.*, 1992). The initial formation of ice, as explained in Section 2.1, commences with the frazil ice formation. This ice can be thought of as frozen slush (Cox and Weeks, 1988). It is called granular ice because it contains randomly oriented, isomeric or prismatic crystals with typical grain diameters in the range of a few millimetres to a few tens of millimetres (Petrich and Eicken, 2017). The granular ice crystal size ranges from a fraction of centimetres to a few centimetres in the Arctic and more in the Antarctic, increasing with the depth of the ice sheet (Cox and Weeks, 1988; Petrich and Eicken, 2017). The granular structure is shown by a yellow boarder in Figure 2-2, which is made up of snow, infiltrated snow ice and the initial skim (Løset *et al.*, 2006).

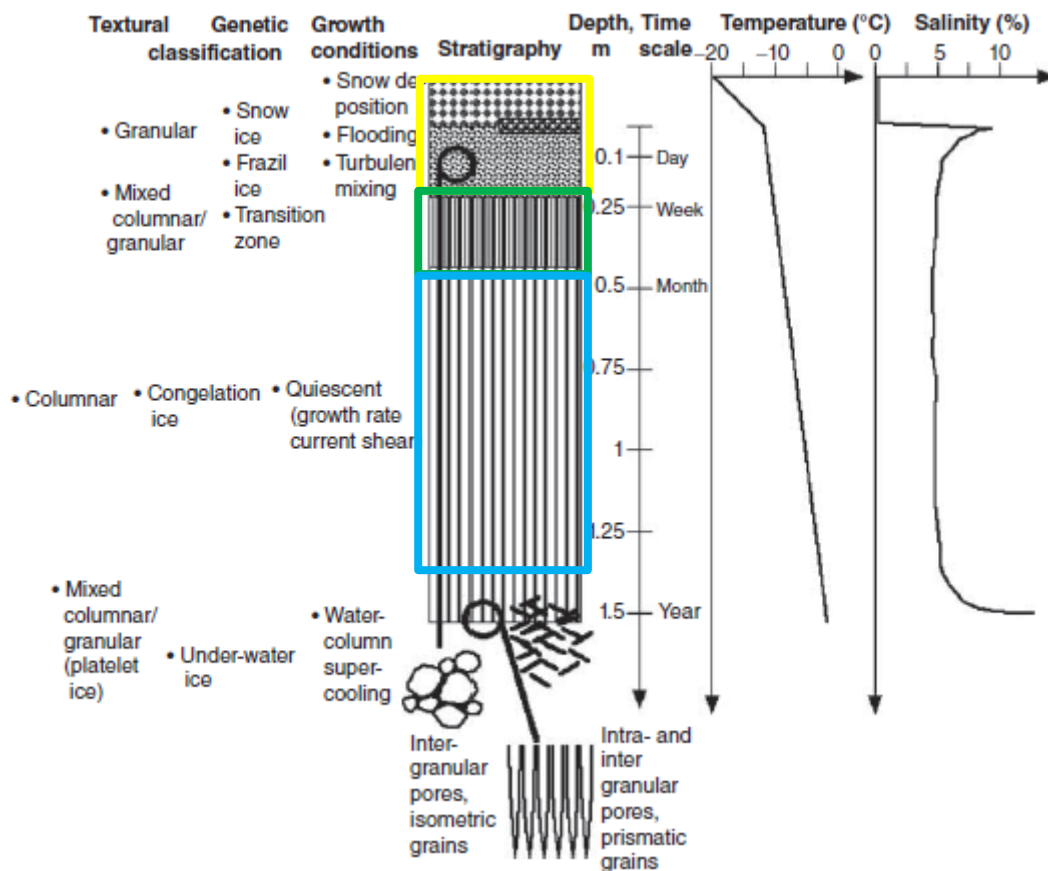


Figure 2-2 Schematic showing ice textures, growth conditions and typical winter temperature and salinity profiles for first-year sea ice (adapted from Petrich and Eicken, 2017).

The columnar zone is characterised by crystals extending vertically downwards, parallel to the direction of heat flow (illustrated by blue boarder in Figure 2-2). These crystals can grow several centimetres in diameter and tens of centimetres in length (Tucker *et al.*, 1992; Petrich and Eicken, 2017). The columnar ice grain size varies, with the diameter being the order of tenths to several centimetres (Tucker *et al.*, 1992). Each grain in this structure contains pure ice plates separated by parallel layers of brine inclusions formed as a result of constitutional supercooling, which, allows for brine entrapment. Constitutional supercooling is evident when some seawater remains in liquid form (brine inclusions) when seawater is exposed to low ambient temperatures below the solution freezing point. This is caused by the more rapid diffusion of heat than salt in the freezing interface (Tucker *et al.*, 1992). The

intermediate/transition zone is where both granular and columnar textures co-exist, and granular is slowly phased out by geometric selection, favouring the pronounced vertical elongation of ice crystals (as seen from the green boarder in Figure 2-2). The transition zone is fairly thin, ranging from 5 cm to approximately 30 cm (Løset *et al.*, 2006). This is an illustration of an intermediate process of going from one well-defined structure to another.

Eicken and Lange (1989) constructed Table 2.1 as a reference for classifying sea ice crystals according to their textures. Different crystal textures are found on ice samples grown at a particular environment with unique growth conditions.

Table 2.1 Textural classification by size and grain shape (adapted from Eicken and Lange (1989))

Textural class	Grain size (mm)	Grain shape	Brine inclusions
Polygonal granular	< 10	Isometric, planar boundaries meeting at 120°	Spherical droplets at grain junctions
Orbital granular	< 10	Isometric; convex, rounded grain boundaries	Irregular pockets and droplets between grains
Columnar	10 - > 100	Elongate	Parallel layers within grains
Intermediate columnar/granular	10 - 100	Slightly elongated; grains indented and interlocked	Oblong; strings of isolated pockets
Mixed columnar/granular	< 10 - > 100	Domains of granular and columnar texture occurring next to each other	

2.4 Temperature and Salinity profiles of sea ice

Sea ice growth dynamics are dependent on atmospheric temperature. Seawater freezes at sub-zero temperatures, below the freezing point temperature of freshwater. This is because of the presence of salt, which depresses the freezing point of the solution according to Equations 2-1 to 2-4 as shown below:

$$T_f = -0.003 - 0.0527S_w - 0.00004S_w^2 \quad \text{Equation 2-1}$$

$$T_f = (-5.33 \times 10^{-7}S^3) - (9.37 \times 10^{-6}S^2) - 0.0592S \quad \text{Equation 2-2}$$

$$S = -2.2330 - 19.3188T_f - 0.6574T_f^2 - 0.0110T_f^3 \quad \text{Equation 2-3}$$

$$T_f = -0.0966S - 0.0000035S^3 \quad \text{Equation 2-4}$$

where T_f is the freezing temperature of the solution and S_w or S is the water salinity in parts per thousands (ppt).

Equation 2-1 (Maykut, 1985) was derived from Neumann and Pierson (1966) temperature and salinity correlations, while, Equation 2-2 (Notz *et al.*, 2005) was derived from the experimental data obtained by Weast (1971). Equation 2-3 (Butler *et al.*, 2016) and Equation 2-4 (Nelson and Thompson, 1954) were developed with the focus on the precipitation of salts as sea water freezes by following the liquid phase composition at varying temperatures. These equations yield similar results, however, the difference lies in the experimental conditions used to acquire data, such as; apparatus and instruments used and growth period (Vancoppenolle *et al.*, 2019).

Once the initial layer of ice has formed on the water surface, conduction rather than convection becomes the dominant heat transfer mechanism. Earlier studies of sea ice reported ice

temperature profiles following an increasing linear trend (Figure 2-2) with increasing depth of a floe (Petrich and Eicken, 2017). This follows from the direction of heat exchange in the ocean – moving vertically up, away from the underlying water to the atmosphere. Thus, the surface layer and the ice provide cooling to the water.

Salinity distribution is as a result of salt expelled during sea ice formation. Sea ice salinity at the surface is typically high due to brine expulsion. This is the desalination process dominant at the initial stages of ice formation (Notz and Woster, 2009). As atmospheric temperature decreases, sea water densities increase and this heavy water sinks to the bottom, displacing the subsurface water to the top. This density-driven water circulation resulting in convective overturning is termed thermohaline circulation (Apeal, 1999). This circulation keeps the salinity at its minimum, thus resulting in minimum sea ice salinities at the middle of the ice, resulting in a C shape salinity profile in the ice as seen in Figure 2-3 A.

Another salinity profile identified by (Eicken, 1992). is an S-shape curve profile (Figure 2-3 B). This profile is similar to the C-shape profile for the top part of the floe and start decreasing or remaining constant towards the bottom. The “? – profile”, shown in Figure 2-3 C, has an inverse pattern to the “S-shape” with salinity decreasing towards the top of the floe (desalination and melt water flushing), increasing in the middle and decreasing towards the bottom. Figure 2-3 D shows an “I-type” profile. This is reported for general linear salinity profiles decreasing towards the bottom of the floe.

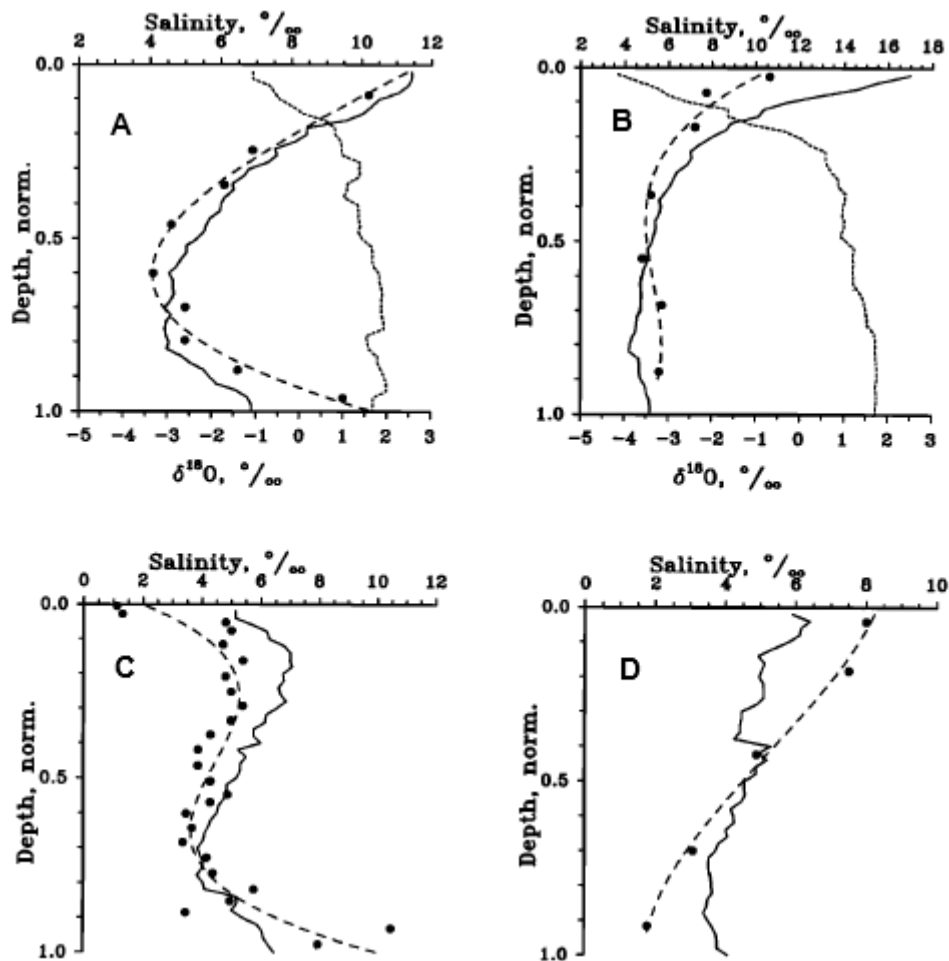


Figure 2-3 Normalised salinity curves. A show a C-type curve where ice salinities are high at the top and bottom of the sample. B shows an S-type curve where salinities are high at the top, remain constant or decrease towards the bottom. C shows an opposite of the S-type, the ?-type. D shows the I-type curve with salinities remaining almost constant throughout the sample taken from Eicken (1992).

2.5 Sea ice salinity and temperature dependence on ice growth rate

The knowledge of sea ice growth conditions enables the understanding of its properties. Sea ice growth temperature, salinity, crystal structure, and air content, influence the quality of sea ice (Nakawo and Sinha, 1981). Studies relating sea ice growth rates are mostly limited to first-year ice of thickness less than 30 cm (Fukutomi *et al.*, 1951; Nakawo and Sinha, 1981). These studies were based on the principle that temperature distribution in the ice sheet is dependent on the surface temperature, the freezing temperature of seawater, and the ice thickness (Cox

and weeks, 1988). Models used by Nakawo and Sinha (1981) to determine growth rates in sea ice assumed a linear temperature distribution in the ice sheet. A 68% accuracy was achieved upon comparing the computed temperatures to those measured for the natural Arctic sea ice during the winter season. Thus, growth rate is dependent on the mean ambient temperatures.

Growth rates are enhanced by cold (low) ambient temperatures, while they are also slowed by warmer ambient temperatures. Nakawo and Sinha (1981) observed a low salinity of 4 psu at a depth between 10 cm and 30 cm related to a slow growth rate. Higher salinities of 7.5 psu were recorded for thicker ice at colder growth period. Similarly, Cox and Weeks (1988) found that the thicker the ice, the lower its temperature at any level in the ice. Hence, this ice surface temperature was closer to the ambient temperature. Thus, implying that ice thickness also influences the ice properties. The crystal structure of sea ice was also featured in Nakawo and Sinha (1981) results. They observed a granular texture for the first 2 cm of ice thickness, and discontinuous columnar crystals between 2 cm and 25 cm. A high salinity of 11.4 psu and a corresponding growth rate of 0.6 cm/day was seen for the top granular section.

As discussed in this section, the ice salinity dependence on growth velocity and the salt concentration of the underlying seawater can be expressed as follows (Cox and Weeks, 1988):

$$S_i = k_{eff} S_w \quad \text{Equation 2-5}$$

Where:

S_i is the ice salinity

S_w is the sea water salinity

k_{eff} is the effective distribution coefficient dependant on sea ice growth velocity,

$$k_{eff} = 0.12, \text{ for } v < 2.0 \times 10^{-6} \text{ cm. s}^{-1} \quad \text{Equation 2-6}$$

$$k_{eff} = 0.8925 + 0.0568 \ln(v) \text{ for } 2 \times 10^{-6} \text{ cm. s}^{-1} < v < 3.6 \times 10^{-5} \text{ cm. s}^{-1} \quad \text{Equation 2-7}$$

$$k_{eff} = 0.26 / (0.26 + 0.74 \exp(-72438 * v)) \text{ for } v > 3.6 \times 10^{-5} \text{ cm} \cdot \text{s}^{-1}$$

Equation 2-8

Equation 2-3 can be used to quantify the initial ice salinity during the initial salt entrapment process, preceding brine expulsion (Cox and Weeks, 1988).

2.6 Brine channel evolution

As sea ice forms, impurities (salts) are rejected from the ice lattice. A boundary layer is formed with high salinity at the top, since salt is expelled from ice, and low salinity at the bottom. This creates a downward flux of salt. Simultaneously, an upward flux of heat is produced since temperature at the ice-water interface is lower than in the water (Maykut, 1985). With continued cooling, and thus, ice growth, columnar crystals are found above this saline boundary. A system of parallel, vertically aligned cells, referred to as the 'skeletal layer' is formed within crystals of the columnar ice, shown in Figure 2-4 A (Ackley and Weeks, 1990; Maykut, 1985).

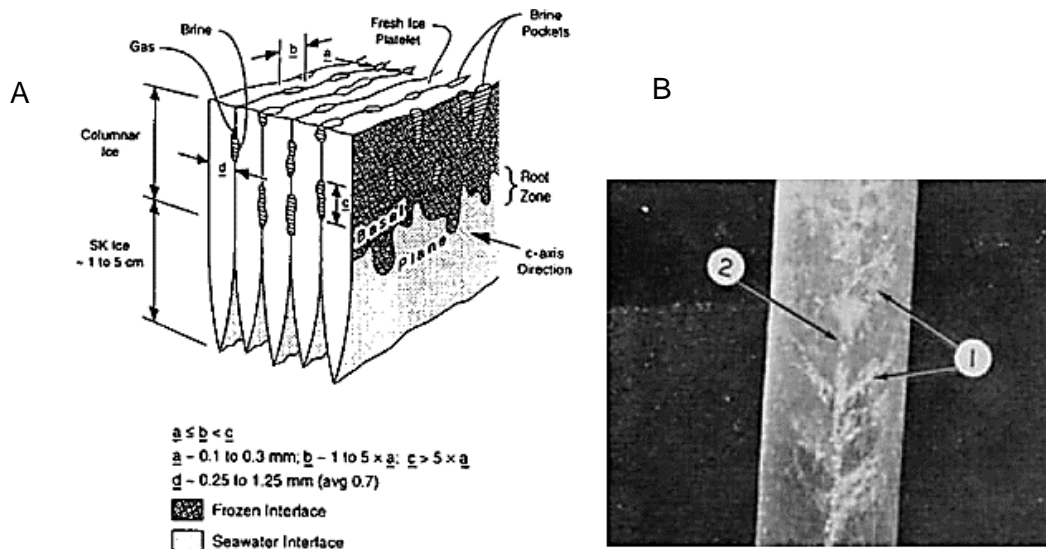


Figure 2-4 A shows sea ice skeletal layer taken from (Løset et al., 2006) and B shows the sea ice core showing (1) feeder channel and (2) brine tube extending outwards taken from (Kovacs, 1996).

Small bridges entrapping brine (and gas pockets), typically long and narrow, with average diameters of 0.7 mm (Kovacs, 1996), form between adjacent parallel cells. As ice thickness increases, the volume of brine in the pockets decreases due to freezing of water surrounding ice and salt expulsion (Løset *et al.*, 2006). In frazil ice however, pockets of high brine concentrations are found between individual ice crystals (Ackley and Weeks, 1990). Brine expulsion occur through the flow route explained by Kovacs (1996) as a 'trunk and branches of a tree', the drainage tube and brine channels respectively (Figure 2-4 B), and it is enhanced by faster growth rate (Kovacs, 1996). Brine pocket migration, brine expulsion, and gravity drainage mentioned by Weeks and Ackley (1982) as sea ice desalination mechanisms are discussed.

2.6.1 Brine pocket migration

Whitman (1926) states that at phase equilibrium, the temperature gradient in ice establishes a concentration gradient in a brine pocket. During winter, this causes the diffusion of solute from the cold upper saline part of the brine pocket to the warm lower part that is less saline. The ice part of the warm end of the brine pocket melts while the water part of the cold side freezes. This temperature and concentration gradient results in the migration of brine pockets out of the ice structure (Weeks and Ackley, 1982). The disadvantage with this mechanism is that brine pockets are very small (diameter approximately 4 – 80 μm), which inhibits convection, and therefore, results in extremely slow movement of brine pockets.

2.6.2 Brine expulsion

Changes in the atmospheric temperature leading to growth and decay of sea ice, causes changes in the volume of brine inclusions, and this subsequently leads to pressure gradients which drive brine expulsion (Notz and Worster, 2009). However, analytical studies by Cox and

Weeks (1975) show that brine velocity during brine expulsion is less than the growth rate of ice at the interface, implying that brine expulsion by expansion of inclusions cannot be the only mechanism responsible for desalination. Thus, Notz and Worster (2009) suggested that transportation of salt to the lower parts of the mushy layer and increasing porosity as a result of brine expulsion only enhances gravity drainage.

2.6.3 Gravity drainage

This phenomenon is observed when brine drains from ice into sea water under the influence of gravity. The ice temperature gradient determines the brine density distribution, and this causes convective overturning of brine within the mushy layer and the replacement of denser brine in the ice with seawater near the interface (Notz and Worster, 2009; Weeks and Ackley, 1982). Experiments performed by (Cox and Weeks, 1975) show that the increase in temperature within the ice or increasing brine volume, increases the rate of change of salinity, and this appear to be the dominant brine drainage mechanism (Weeks and Ackley, 1982). In this case, brine drainage rate is dependent on the ice temperature gradient, which determines the brine density gradient, brine volume and permeability.

Weeks and Ackley (1982) makes three concluding marks about brine drainage mechanism; increasing diameter of the brine channels reduces viscous drags on downward-moving brine, the pressure drop responsible for stalactites formation facilitates brine drainage, and the cooling of ice surrounding the brine channel causes brine expulsion into the channel.

2.7 Factors affecting sea ice texture and brine inclusions

2.7.1 The effect of *in-situ* temperature on sea ice texture and sea ice crystal structure

Sea ice texture and brine inclusions strongly depend on the ice *in-situ* temperature and salinity (Perovich and Gow, 1991). This was supported by the study of thermal evolution of brine inclusions in natural sea ice by Eicken *et al.* (2000). An increase in the mean inclusion size and elongation, and a decrease in their number density as a result of the vertical coalescing of pores when the scanning temperature was increased from -10°C to -6°C were observed. Perovich and Gow (1996) also investigated the effect of increasing brine volume on inclusions as the scanning temperature increases. This was done through warming horizontal thin sections extracted from the bottom of lead ice, from -20°C to -1°C . As the brine volume increased with increasing temperature, the mean area of brine inclusions increased. Like Eicken *et al.* (2000), Perovich and Gow (1996) explained that this observation is due to the coalescing of inclusions thus, observing the same effect as Eicken *et al.* (2000). They further indicated that there are many small inclusions present at low ambient temperatures that were not identified as they merged to form enlarged inclusions with increasing temperatures.

Figure 2-5 shows the growth-melt-growth cycle of artificial sea ice over a 14-day period, 09 - 22 November 1998, from the study conducted by Tison *et al.* (2002). It was observed that warming of ice from -15°C to -2°C changed the crystals structure by increasing the overall crystal size.

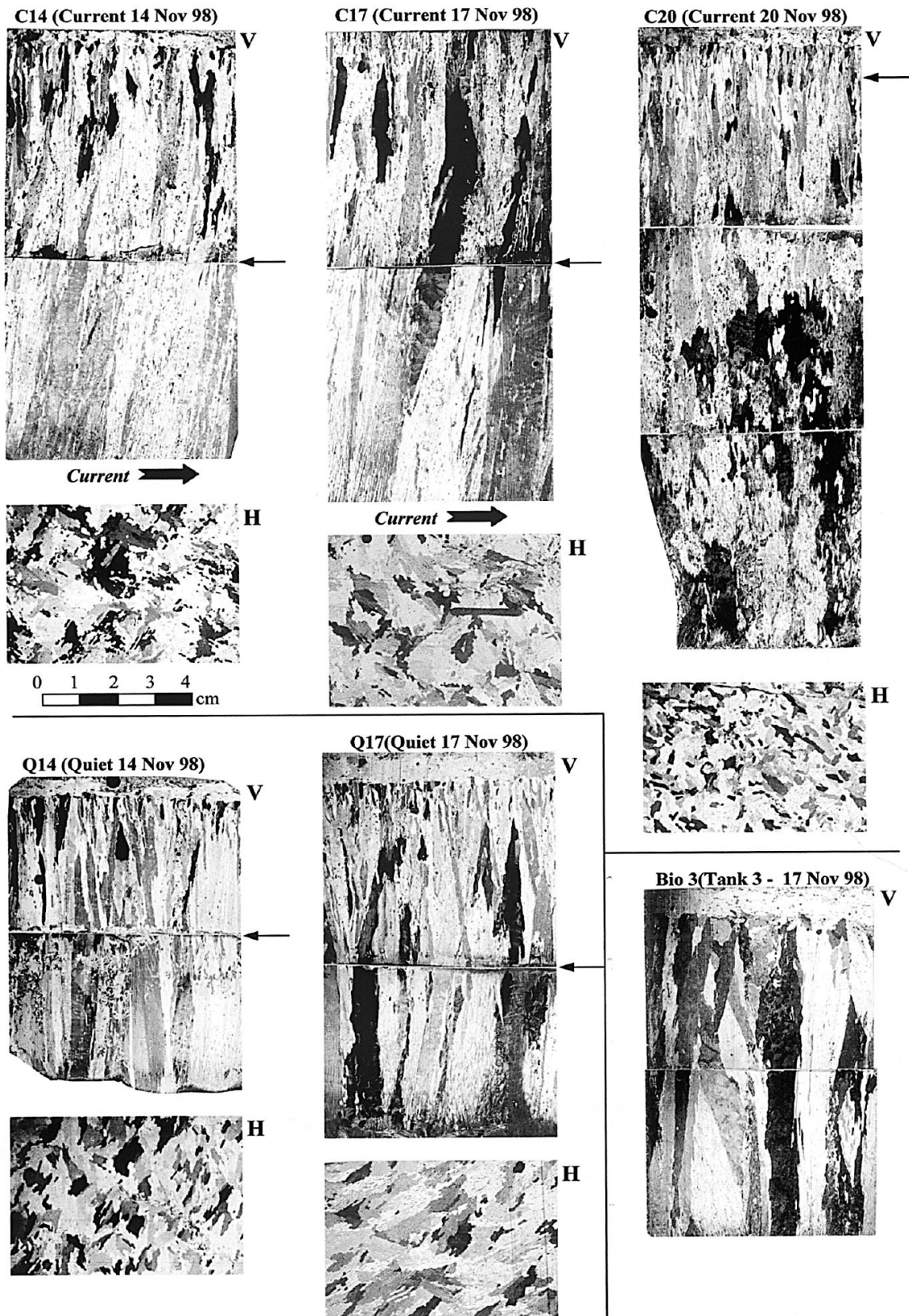


Figure 2-5 Vertical (V) and horizontal (H) thin sections obtained from cross polarisation imaging showing sample at the end of growth (14 November), warming period (17 November), and cooling period (20 November) in the current, quiet and biochemical tank (Tison et al., 2002).

Vertical thin sections from each sample of artificial sea ice grown at -15°C from a starting artificial ocean salinity of 35 psu, during turbulent and calm conditions are shown in Figure 2-5. The visuals obtained for growth under turbulent conditions, C14, C17, and C20, corresponds to the end of growth (-15°C), warming (-2°C), and cooling (-22°C) respectively. For the calm conditions, Q14 and Q17 were obtained at the end of growth and warming respectively. In their observations, Tison *et al.* (2002) found that at the end of the warming period, both the turbulent and calm condition samples revealed an increase in congelation ice crystals, and an overall decrease in bulk salinity. At the end of cooling phase, retexturing was observed and there was a net salt increase to the system. This increase applied to both samples grown during turbulent and calm conditions.

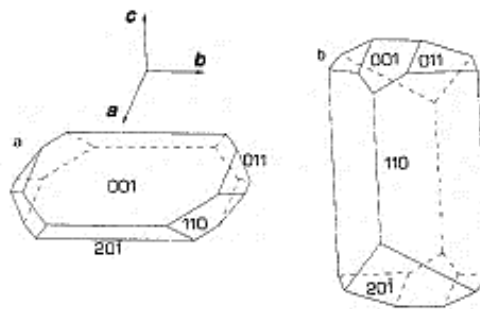


Figure 2-6 Paracetamol crystals grown at (a) 3°C and (b) 47°C (Shekunov *et al.*, 1996)

Palermo and Grove (1964) reported the effect of temperature on the rate of crystal growth of potassium alum crystals in a batch experiment. They found that crystals grow larger at high ambient temperatures. Shekunov *et al.* (1996), in their study of temperature effects on crystal growth and crystal properties of paracetamol, they found that at low ambient temperatures there were more crystals and inclusions, and the crystals were of poor quality or strength. They also identified a change in the dominant crystal shape at different temperatures. Prismatic shapes with 110 faces crystals were dominant at high temperatures, while, at low temperatures crystals were plate-like with 001 faces (Figure 2-6). At high ambient temperatures, crystals were stronger with more resistance to fracture, as well as more elastic (Shekunov *et al.*, 1996).

2.7.2 The effect of salinity on sea ice texture and sea ice crystal structure

Sea ice, in contrast to freshwater or glacial ice, is characterised by the presence of salt entrapped within its structure, with most of it expelled during the freezing process. This is evident through studies of sea ice microstructure including bulk salinity measurements. Sea ice bulk salinity ranges between 4 psu and 6 psu (Weeks and Ackley, 1982), which is significantly lower than that of initial seawater, typically 32 psu to 35 psu (Timco and Weeks, 2010). The effect of salt in sea ice can be explained using the structure of first-year and multi-year ice. This is because first-year ice is more saline since it was grown for no more than one winter season and has not undergone a cycle of desalination (Løset *et al.* 2006). Whereas, ice that has survived at least one summer melt season and undergone a full cycle of desalination is termed multi-year ice (Løset *et al.*, 2006; Timco and Weeks, 2010; Weeks and Ackley, 1982). Multi-year ice is characterised by having lower salinities compared to first-year ice. Thus, multi-year ice is less porous, hence mechanically stronger compared to first-year ice (Timco and Weeks, 2010).

Figure 2-7 is an illustration of the microstructure of first-year ice showing the salt entrapped in brine pockets as seen from the zoomed area.

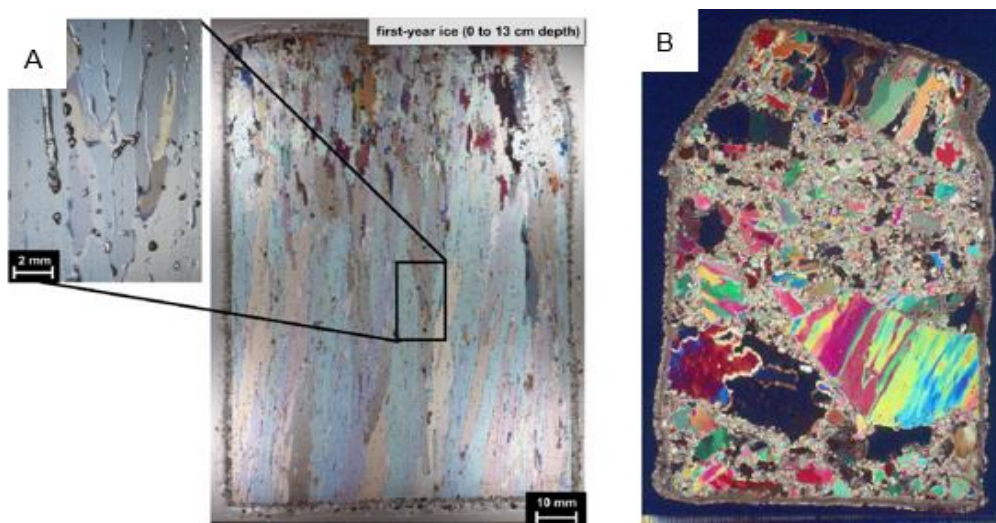


Figure 2-7 (A) shows first-year ice and (B) shows multi-year ice taken from Timco and Weeks (2010)

Studies performed by Gow *et al.* (1987) for the Weddell sea ice, and Cox and Weeks (1973) for the Arctic sea ice, confirm that the salinity of first-year ice is higher than that of multi-year ice, albeit the Weddell sea ice measured salinities slightly higher than those for the Arctic ice for comparable thickness among first-year and multi-year ice of both regions (Gow *et al.*, 1987).

Studies of brine analysis of sea ice show that longer freezing periods result in lower brine volumes in sea ice as water around the brine pockets keep freezing (Løset *et al.*, 2006). Additionally, at lower atmospheric temperatures, brine flux in the mushy layer is enhanced (Wettlaufer *et al.*, 1997). The increasing salt content increases brine pocket sizes, and the overall brine volume. Thus, porosity of the ice increases (Weeks and Ackley, 1982). Hence, Cottier *et al.* (1999) describes brine channels as flaws to the ice cover since porosity affects the mechanical properties, flexural strength and fracturing (Cottier and Wadhams., 1999; Løset *et al.*, 2006). However, increasing porosity is not synonymous to increasing permeability as the pores may be clogged or tortuous (Krembs *et al.*, 2011).

2.7.3 The effect of microorganisms secretions on sea ice texture and sea ice crystal structure

Sea ice is reported to be a habitat for microorganisms such as algae, bacteria, and protozoa, which reside in the brine channels and pockets inside sea ice (Weeks and Ackley, 1982; Middleton *et al.*, 2016). Organic matter is reported by Dumont *et al.* (2009) to be either allochthonous i.e. trapped as the ice forms or autochthonous i.e. formed within the ice cover. Weeks and Ackley (1982) explain the presence of organic matter to be due to microorganism accumulation through ice crystal scavenging and ice nucleation of suspended organic material. Dumont *et al.* (2009) allude to the fact that ice-active microorganism substances – dimethylsulphoniopropionate (DMSP) and extracellular polymeric substances (EPS) are enhanced by extreme environmental conditions (low temperature and high salinity). Transparent exopolymeric particles, derived from EPS have been found on the sea ice cover.

EPS are defined as organic materials of high surface area and complex behaviour in aqueous solutions (Krembs *et al.*, 2011). They are microscopically observed to exist in brine inclusions, serving as cryoprotectants and osmoprotectants (Krembs *et al.*, 2011) with brine fluid viscosity strongly dependent on the quantity of EPS within the brine channel (Brierley and Thomas, 2002). The presence of EPS in water is suggested to increase the ice porosity and salinity by modifying the pore spaces and salt expulsion processes (Krembs *et al.*, 2011).

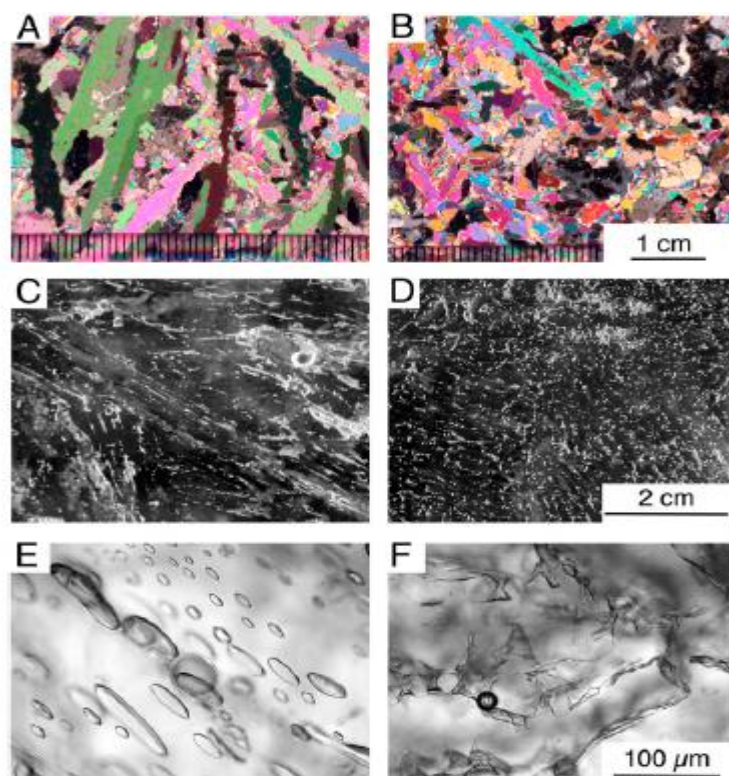


Figure 2-8 Microscope images of artificial ice grown at -10 °C. A and B show ice texture at low magnification under polarised light, C and D with contrast staining, and E and F showing pore structure at high magnification. A, C and E was EPS free while, B, D and F had EPS added. Sourced from (Krembs *et al.*, 2011)).

Microscopic analysis of brine inclusions of artificially grown ice with and without EPS, as well as salt retention measurements were carried out by Krembs *et al.* (2011). Xanthan gum (XG) – the EPS reference standard in marine bacterium was used to examine EPS effects on salt

retention and ice microstructure. High uronic acid content found in sea ice is suggested to be evidence of the gelling properties increasing fluid viscosity, thus, altering the ice crystal morphology (Krembs *et al.*, 2011).

High concentrations of EPS were found at the bottom layer of natural sea ice. It showed brine inclusions arranged in subparallel arrays with approximately 52% of them containing stained EPS. Analysis of the pores with EPS showed the presence of diatoms and detritus, and they were observed to have a complex angular shape (Krembs *et al.*, 2011).

Fine-grained columnar ice with intergranular brine inclusions poorly arranged, and possessing an irregular complex shape were revealed, as shown in Figure 2-8 B, D and F. On the contrary, EPS-free artificially-grown ice revealed coarse-grained ellipsoidal brine channels with a lamellar inclusion and a number of lamellar crystal features (Figure 2-8 A, C and E). Approximately 15% more pores were observed in EPS-containing ice than in EPS-free ice, as seen in Figure 2-8 C and D respectively (Krembs *et al.*, 2011). A 12–35% higher bulk salinity was observed in artificially-grown ice with EPS at the ice/water interface.

2.8 Artificial sea ice growth

Studies investigated the effect of growth factors such as temperature on sea ice brine inclusions (Eicken *et al.*, 2000), effects of deformation on mechanical behaviour of sea ice (Schulson *et al.*, 2015), sea ice optical properties (Marks *et al.*, 2017), and the effects of air-sea CO₂ flux on sea ice growth (Nomura *et al.*, 2006). These studies were performed in the laboratory since variables can be controlled and isolated unlike in the field, where ice growth is affected by many variables at the same time.

2.8.1 Reactor size, shape and material of construction

There are different reactor set-ups, dimensions, material of construction, and reactor fittings used for artificial sea ice growth. Each design is made to suit the function of the reactor or the purpose of the experiment. These include the conventional three-dimensional (3D) cylindrical and cubic tanks, as well as the semi two-dimensional (2D) tanks with very small widths. The use of the former is mostly dominant in sea ice crystal structure studies involving sampling and imaging of sea ice (Nomura *et al.*, 2006). While, the latter is used for extracting thermodynamic data, and in recent advances, it also allows visualisation of brine drainage features as ice forms (Middleton *et al.*, 2016). Usually, studies of sea ice growth from semi 2D tanks uses a cold lid with a circulating coolant to enhance unidirectional top down artificial sea ice growth (Cox and Weeks, 1988; Wettlaufer *et al.*, 1997), placed in a room temperature laboratory or a chamber independent of temperature control (Wettlaufer *et al.*, 1997).

Haas (1999) study of small-scale properties and processes of artificial sea ice, grown at different conditions, used a large indoor reactor with the volume of 180 000 L. They state that for studies which prioritise control over boundary conditions, smaller reactors are preferred. While, larger reactors are better suited for the experiments involving analysis of crystal structure since they allow for sufficient areas for sampling (Haas, 1999). The effect of growing ice from reactors of different volumes on sea ice morphology and crystal structure have not been reported yet. The commonly used reactor material of construction are polyethylene and acrylic, with fibre glass and Nalgene used less frequently. Cubic reactors are often reported, however, Marks *et al.* (2017) allude to the fact that the use of a cylindrical reactor minimises mechanical stress in the reactor.

Different studies have used different reactor volumes ranging from 50 L to as large as 180 000 L basins (Haas *et al.*, 1999; Tison *et al.*, 2002), as seen in Table 2.2. However, there is no clear justification for the choice of reactor type, volume and shape used.

Table 2.2 Comparison of reactors used for artificial sea ice growth experiments from literature

Author	Tank Dimensions	Insulation	Heating	Temperature delivery method	Mixing method
Wiese (2012)	V= 308 L, H= 1.94 m, D= 0.66 m Water Height = 0.9 m	Tank walls and bottom: Styrofoam plates Thickness = 0.05 m	Heating plates installed around tank Heating wire – bottom of tank to mimic oceanic heat flux	Cold room (-20 °C)	2 pumps pre-experiment since calm conditions required
Schulson, <i>et al.</i> (2015)	2 tanks: V= 800 L and 57 L H= 1.02 m D=1 m	Wall: 2, 25 mm layers Thickness= 0.05 m		Capped with cooling plate of aluminium (22 to 30 cm ice depth)	Pump used for mixing
Marks <i>et al.</i> (2017)	V= 2000 L H= 1.32 m D= 1.39 m	Tank bottom: Placed on insulated pallets. Walls: 1 cm black neoprene and wooden boards with mould resistant paint on a 3 cm polystyrene insulation	Close pipe run around the bottom of the tank connected to the heater – Set at 0 °C	Cold lab	Pump circulates water at 10 L/min
Kuehn <i>et al.</i> (1987)	V= 946 L H= 1.23 m D= 0.91 m	Sides were insulated (material and thickness not stated)		Capped with cold plate. Placed in the Cold lab Set at 0 °C	
Aussillous <i>et al.</i> (2006) (Solution is sugar water not salt)	V= 0.2 L H= 0.18 m D= 0.037 m	Walls: Surrounded by a glass jacket set at -3 °C Polystyrene placed above glass plate/ lid		Capped with 2 mm cold glass plate	
Wettlaufer <i>et al.</i> (1997)	V= 15 L H= 37.6 W= 0.2 m L = 0.2 m	Walls: 5 cm polystyrene		Cooling brass lid - ethylene glycol	
Nomura <i>et al.</i> (2006)	Square tank V= 49.5 L H=0.650 m L=0.300 m W=0.300 m Water H = 0.55 m	Tank Thickness =0.010 m Insulation Thickness =0.10 m (material not specified)		Cold lab	Magnetic Stirrer used

2.8.2 *Insulation and temperature delivery method*

The sea ice formation process begins on the ocean surface then proceed downwards into the sea water, in the direction of increasing heat flux. Generally, artificial sea ice reactors are housed in a cold laboratory which can be temperature controlled between ranges of -30°C to 30°C. To promote unidirectional freezing from the top and make sure the solution does not freeze from the walls and bottom, tanks are insulated (Wiese, 2012).

Styrofoam and polystyrene are the common insulation materials used (Havik, 2011; Marks *et al.*, 2017; Wiese, 2012; Wettlaufer *et al.*, 1997). A range of 3 cm to 10 cm of insulation thickness is used. This is determined by heat transfer calculations. It is noted in Table 2.2 that the largest ice growing reactor has the smallest insulation thickness as compared with the smallest one. However, it is not known if there is a relationship to this observation since there were no calculations or justifications given. Some experiments were conducted with the addition of side heating to the insulation (Havik, 2011; Wiese, 2012; Marks *et al.*, 2017). Wiese (2012) installed heating plates in between the tank walls and the insulating material. Furthermore, Marks *et al.* (2017) and Wiese (2012) also added a heating wire at the bottom of the reactor to simulate the oceanic heat flux. This warms the reactor bottom and prevent freezing to ensure ice grows only from the top.

2.8.3 *Mixing*

To keep the water well mixed and avoid temperature and salinity stratification, mixing is induced in the reactors using pumps or magnetic stirrers as seen in Table 2.2 (Marks *et al.*, 2017; Wiese, 2012; Schulson *et al.*, 2015) . However, Wiese (2012) states that pumps are not necessary during growth since there is convection due to brine loss, which keeps the solution mixed. Thus, pumps can be switched on to mix the starting solution and kept off during the

experiment. Conversely, Nomura *et al.* (2006) used magnetic stirrers to provide homogeneous mixing.

2.9 Sea ice physical properties and growth dynamics

Sea ice thermodynamics can be described by cooling or warming of the ice due to a conductive heat flux gradient and internal heat sources. The oceanic heat flux is primarily exchanged in the vertical direction due to thermohaline circulation since the cold air source is the atmosphere, exchanging heat with the underlying ocean water. Subsequently, the horizontal ocean circulation is due to the wind stress at the ocean surface. Figure 2-9 illustrates the heat fluxes involved during ice growth, where Q_a and Q_w represent the atmospheric and oceanic heat flux respectively. $Q_{c,t}$ and $Q_{c,b}$ corresponds to the ice top and bottom conductive heat fluxes respectively, and Q_L represents the latent heat due to ice growth (Wiese, 2012).

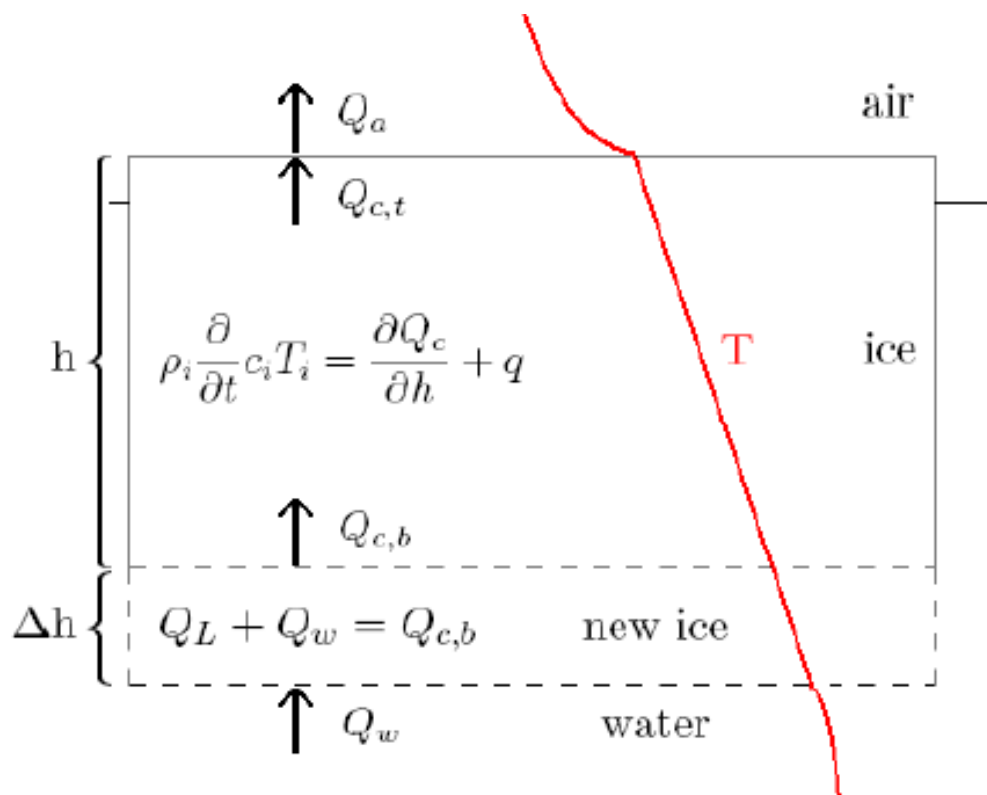


Figure 2-9 Heat fluxes during ice growth - 1D-approach (Wiese, 2012).

A few assumptions are made for calculating ice growth using Stefan's law. It is assumed that the thermal inertia is negligible ($c_i = 0$), the surface of the ice has a temperature of the air above it, while the temperature of the bottom of the ice is equal to that of the water below it. Thus, the conduction heat is constant throughout the ice sheet, and the conductive heat flux Q_c is equal to the atmospheric heat flux at the top, latent and the oceanic heat flux at the bottom ($Q_{c,t} = Q_{c,b}$). Therefore, Stefan's law allows the calculation of the ice thickness h , where L_i is the latent heat of fusion (Lepparanta, 1993).

The data from artificial sea ice temperature measured during growth was reported by Wettlaufer *et al.* (1997), from seven thermistors (B to H) in the ice, and E, F, G, and H in the water underneath the ice is shown in Figure 2-10.

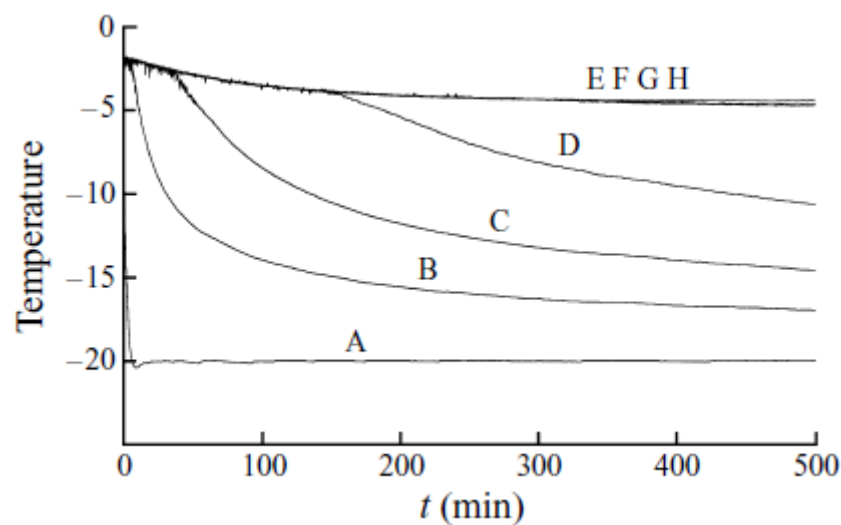


Figure 2-10 The temperatures recorded by the thermistors as function of time for sea ice experiments performed at -20°C ambient temperature, adapted from Wettlaufer *et al.* (1997)

Probe A, which measures the ambient temperature, drops quickly after the initiation of ice growth. Probe B, C, and D show temperature slowly decreasing in an effort to approach the ambient temperature. Probe E, F, G, and H initially show a slight decrease in temperatures and remain constant at the freezing point of the solution. These are the probes that remain in the water under ice (Wettlaufer, *et al.*, 1997).

2.10 Analytical techniques of studying sea ice crystal structure

Sea ice is made up of individual ice crystals with different shapes, size and orientation. The typical average reported crystal size is 1 – 5 mm (Svensson, 2004; Wilen, 2000). When ice flows, its crystal structure changes, and the orientation and size influences ice deformation. Thus, ice crystal structure can be used to determine the ice flow and deformation processes.

2.10.1 Cross Polarisation

Cross polarisation is a visualisation technique that provides information on the crystal structure through examination of ice thin section (Durand *et al.*, 2006). It relies on the polarisation and propagation of light to reveal the orientation of different ice crystals. Previous ice texture studies were manual and time-consuming (Durand *et al.*, 2006; Wilen, 2000) until the development of automatic ice texture measurements including the automatic ice-fabric analyser (AIFA) developed by Yun and Azuma (1999). This technique uses optical thin sectioning, which require samples less than 1 mm (Langway, 1958; Yun and Azuma, 1999). To achieve this, ice samples are cut into thick sections of 1 cm using a bandsaw and ground down to 0.5 mm using a sandpaper or microtome (Langway 1958; Thorsteinsson, 1996).

The standard biological microtome modified with a vacuum plate produces smooth and parallel planes. It allows removal of 1 to 20 μm at each pass under the blade, while enabling reduction to 0.1 mm (Langway, 1959). Microtomes are divided into two groups; manual and automatic. The manual microtomes can produce thin samples ranging from 0.5 to 60 μm (Mahammed *et al.*, 2012). An example is a rotary microtome, which uses a hand-wheel like device which moves the sample to the rigid blade (Handley, 1903). Examples of automatic microtomes are the cryostat, laser, and computerised (Mahammed *et al.*, 2012). The first two are enclosed, with cooling abilities and laser technology respectively. They can cut samples ranging from 2 to 16 μm for cryostat, and 5 to 100 μm for the laser microtome (Bancroft and Gamble, 2008;

Lubatschowski, 2007). The computerised microtome uses a semi-conductor freezing cryoplate which can slide sections from 1 to 25 μm (Mahammed *et al.*, 2012).

The main challenges faced with the microtome technique include the loss of brine and alteration of the ice microstructure during storage and processing. Furthermore, since samples are very thin, it is assumed that there might be some stereological implications on the results (Underwood, 1970; Eicken *et al.*, 2000). Thus, non-destructive tomographic methods such as magnetic resonance imaging (MRI) and computed tomography (CT) scanning are reported to be the potential solution (Eicken *et al.*, 2000).

Crystal structure visuals are obtained with a camera positioned perpendicular to the crossed polariser sheets. Irregular shaped crystals with different colours and sizes are revealed as in Figure 2-11. The resultant crystal colours are dependent on the thickness of the sample, with the optimal thickness corresponding to brown-yellow colours (Gay and Weiss, 1999).

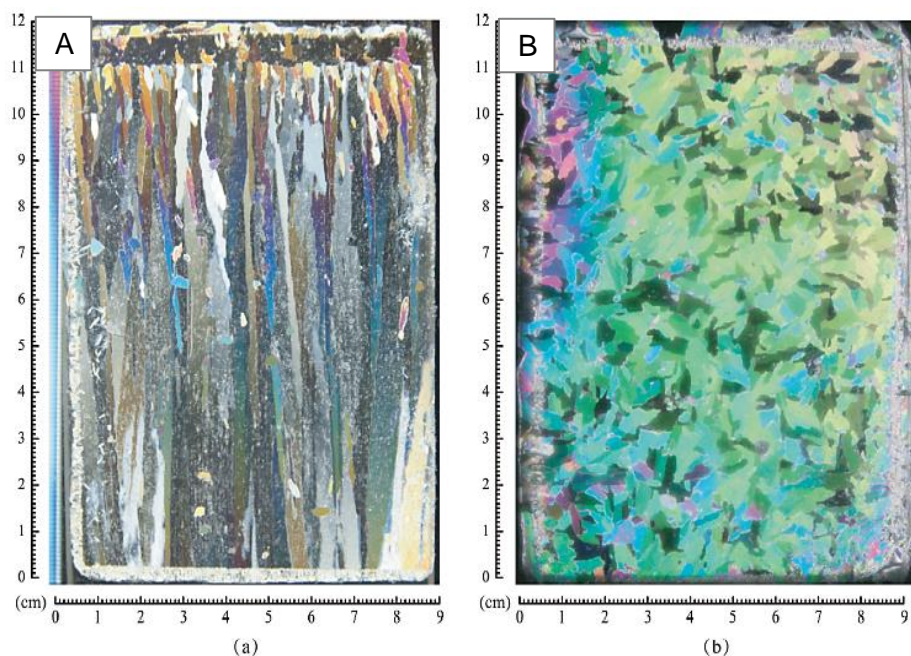


Figure 2-11 Cross polarisation images of ice grown at 24 psu saline water with (a) showing the vertical and (b) showing the horizontal section, taken from Wei *et al.* (2020).

2.10.2 X-ray Micro-Computed Tomography (μ CT)

X-ray micro-computed tomography (μ CT) offer a three-dimensional non-destructive tomographic method for sea ice structural analysis (Kawamura, 1990; Lieb-lappen, 2016). X-ray computed tomography, originally a medical-science invention, has bred the development of industrial x-ray computed tomography scanners (Stock, 2008), enabling the visual studies of the crystal structure of metals, ceramic, plastic and wood (Hopkins *et al.*, 1981). The application was also extended to the fields of geoscience and biology (Campbell *et al.*, 2007). Previously, x-ray computed tomography was found extremely useful in the crystallography field for its non-destructive features, however, overtime developments lead to pore structure analysis (Prodanovic *et al.*, 2006).

X-ray micro-computed tomography employs the fact that materials of different composition and density absorb and transmit x-ray radiation differently (Lieb-lappen, 2016). Furthermore, photoelectric effect is used to explain that heavier phases absorb x-rays better, allowing different phases down to several microns to be distinguished from a material. For this reason, micro-CT is well suited for analysing sea ice since it is a material that consists of three phases: ice, brine and air. The results from scanning are both qualitative and quantitative, producing high resolution three-dimensional images of density contrast. The geometry and size of the x-ray source determines the scan acquisition time and special resolution (Landis and Keane, 2010). Thus, best results are obtained when the x-ray beam passes through equal amount of sample per cycle of rotation. The qualitative results allow visualisation of 3-D features as seen in Figure 2-12 and through colour-coding by volume size. The software also provides quantitative data that allows for analysis of volume, porosity, and surface area.

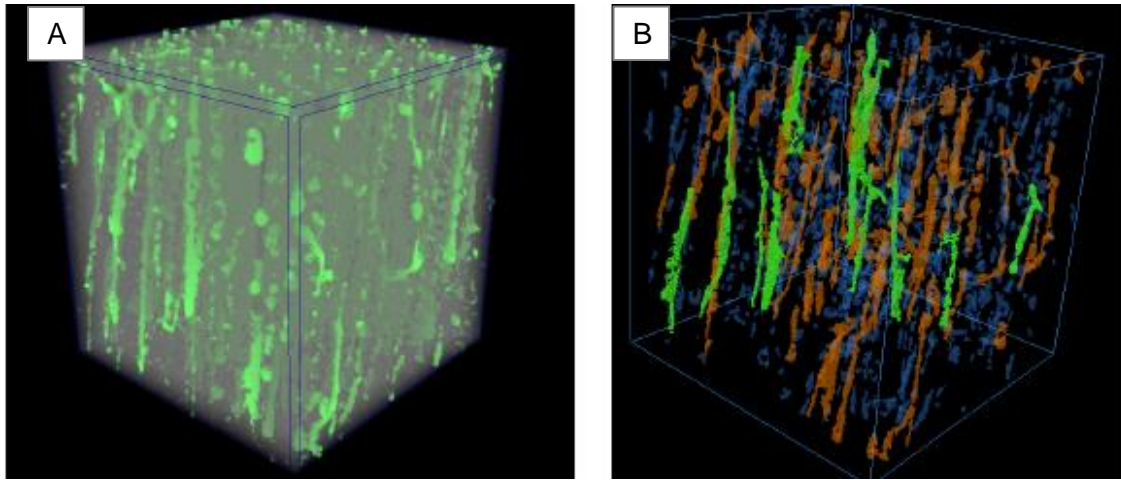


Figure 2-12 Three-dimensional visualisation of sea ice (A) showing all brine channels (B) showing brine channels by volume where the one greater than 0.0337 mm^3 are in green, the channels between 0.0067 mm^3 and 0.0337 mm^3 are in orange, and channels less than 0.00067 mm^3 are blue (image adapted from Lieb-Iappen (2016))

Changes in brine channel connectivity at varying temperatures were investigated by Golden *et al.* (2007) through analysing CsCl-doped artificial sea ice through micro-ct scanning. Later, Maus *et al.* (2009) developed scanning methods that involved centrifugation of samples and storing at sub-zero temperatures to minimise brine loss, thus alteration of the structure. The downside to this was that the protocol could not characterise air pockets from brine inclusions and ice. Recent research use algorithms to analyse the pore network of materials through micro-ct scanning to obtain quantitative results (Golden *et al.*, 2007; Prodanovic *et al.*, 2006)

3 Aim, Objectives and Key Questions

3.1 Aim and Objectives

The aim of this study is to investigate the factors affecting sea ice crystal structure focusing on ambient temperature, starting artificial ocean salinity and the presence of EPS.

The objectives are, therefore, to:

- To determine the effect of varying temperatures and salinities on sea ice texture and porosity
- To determine the effect of varying reactor volume on sea ice texture and porosity
- To determine the effect of the presence of EPS on sea ice texture and porosity

3.2 Key Questions

- How does starting artificial ocean salinity affect sea ice growth dynamics and physical properties?
- How does ambient temperature affect sea ice growth dynamics and physical properties?
- How does reactor volume affect sea ice growth dynamics and physical properties?
- How does the presence of EPS affect sea ice growth dynamics and physical properties?
- How does starting artificial ocean salinity affect sea ice texture and porosity?
- How does ambient temperature affect sea ice texture and porosity?
- How does reactor volume affect sea ice texture and porosity?
- How does the presence of EPS affect sea ice texture and porosity?
- What is the disparity between the artificial sea ice brine volume estimated using the Frankenstein-Garner approach and the Computer Tomography analytical method?

4 Methodology

4.1 Experimental matrix and setup

Artificial sea ice was grown at the University of Cape Town Polar Engineering Research Group mobile sub-zero laboratory (also known as the polar lab). Firstly, artificial sea ice was grown from solutions of varying starting artificial ocean salinity at the same ambient temperature (A, B, and C in Table 4.1). Secondly, the ambient temperature was varied for artificial sea ice growth from solutions of the same starting artificial ocean salinity (D, C, and E in Table 4.1). Thirdly, artificial sea ice was grown from reactors of varying volumes at the same ambient temperature and starting artificial ocean salinity (D and F in Table 4.1). Lastly, artificial sea ice was grown with and without EPS from 3 L reactors at the same ambient temperature and starting artificial ocean salinity (C and G in Table 4.1).

Table 4.1 Experimental matrix labelled alphabetically for the conducted experiments

3 L reactor				30 L reactor	EPS added
	10 psu	20 psu	30 psu	30 psu	
-20 °C			D	F	
-10 °C	A	B	C		G
-5 °C			E		

It should be noted that each experiment was performed in two different reactors. The first reactor set-up involved the installation of temperature probes for analysis of physical properties and growth dynamics. While, the second reactor had no temperature probes for ease of sampling for crystal structure visualisation and brine analysis.

Each 3 L reactor was placed on top of a magnetic stirrer with two 5 mm layers of insulation underneath, a polystyrene sheet and wooden board as seen in Figure 4.1. The layers were

necessary to provide reactor bottom insulation. The artificial sea ice was allowed to grow to no more than 10 cm in the 3 L reactor. This is because it was observed during trial experiments that growth beyond 10 cm induced freezing from the reactor bottom and walls, which was undesired. It was assumed that beyond the 10 cm ice thickness, the insulative properties of artificial sea ice had a dominating effect over the insulation material used around the walls and at the bottom of the reactor. A fan was placed 1 m away and pointed towards the surface of the reactors to allow for even distribution of cold air into the reactors.

For the reactors with temperature probes, five temperature probes were arranged on a PVC scaffold in the reactor (as seen in Figure 4-1). This allowed for the probes to be placed at the desired location for maximum resolution (Hall, 2019). The probes measuring the temperature during artificial sea ice growth were probe 1, 3, and 5, which were placed 1 cm, 3 cm, and 5 cm below the water line respectively. The probe measuring the atmospheric temperature was positioned 1 cm above the water line. The last probe was placed 14 cm below the water line and was used to measure the artificial ocean temperature. This arrangement of temperature probes was adapted from the study of small-scale system design of growth of artificial sea ice by (Hall, 2019). Hall (2019) explained the choice of probe placement and distance between probes by the concept of Ice focus. This permits the vertical spacing between probes to be small enough to allow for maximum resolution and analysis of temperatures within the ice without interference.

To study the effect of varying reactor volume on artificial sea ice morphology, a 30 L reactor was used to grow artificial sea ice at -20°C from a starting artificial ocean salinity of 30 psu. The results of which will be compared to the results obtained for artificial sea ice growth from a 3 L reactor at the same ambient temperature and starting artificial ocean salinity. These growth conditions were chosen because -20°C offers a higher cooling rate, thus, faster ice growth rate, and significantly reduces the growth time.

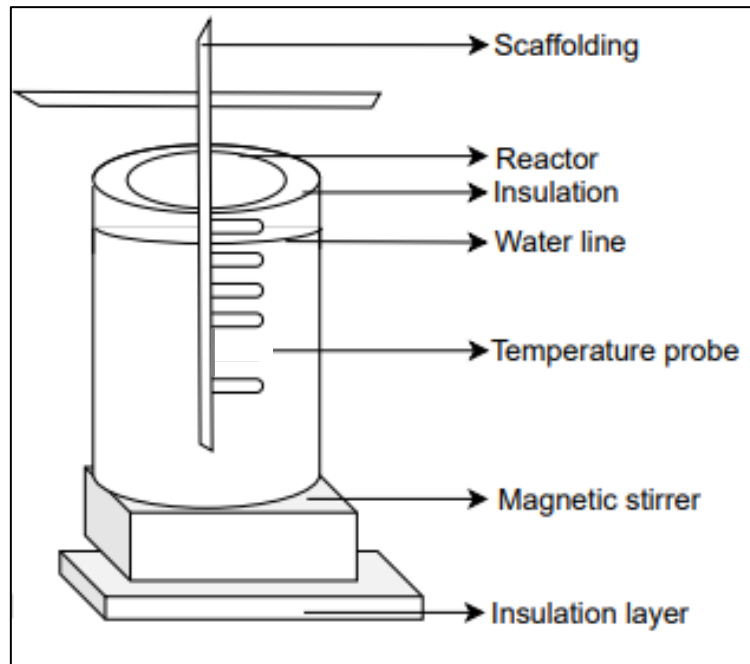


Figure 4-1 Experimental set-up of artificial sea ice growth in the 3 L reactor with temperature probes installed (the 30 L set-up was similar, with 13 temperature probes installed)

4.2 The experimental procedure

4.2.1 Artificial sea ice growth procedure

Artificial seawater solutions were prepared using deionised water with Aquaforest Sea Salt to make solutions of starting artificial ocean salinities of 10 psu, 20 psu, and 30 psu. Deionised water was used to avoid introducing impurities to the system. Since part of this study investigates the effect of varying starting artificial ocean salinity, natural seawater would not be suitable as it has salinities typically constant in the range of 30 psu to 35 psu (Weissenberger *et al.*, 1992; Nomura *et al.*, 2006), and it is expensive to source. The use of synthetic sea salt mixtures such as Aquaforest Sea Salt is widely reported for the growth of artificial sea ice (Cottier and Wadhams, 1999; Papadimitriou *et al.*, 2004; Marks, 2017).

The polar lab was cooled to 1°C for approximately 12 hours to allow for pre-cooling of the saline solutions close to their respective freezing temperatures. The magnetic stirrers were activated for mixing the solution to maintain homogeneity (Nomura et al., 2006). A handheld AZ 8303 Cond./Temp./Logger was used to check each solutions' temperature to see whether they were uniform at 1°C. After cooling, the reactor walls were then insulated using a 15 cm insulation made of Styrofoam wrapped with black plastic (for ease of handling), and the lab temperature was decreased to the desired ambient temperature to start the experiment. The insulation served to prevent artificial sea ice growth from the walls of the reactor, since top-down growth of the ice nucleated at the surface is desired. The solutions were monitored until the freezing point temperature for each respective solution was reached. At this point, the solutions were seeded with ice shavings to create nucleation points.

4.2.2 Artificial sea ice sampling procedure

After the ice growth experiment, the temperature data was collected from the data logger and artificial sea ice was sampled at -10°C for visualisation through cross polarisation and ct-scanning.

A Stanley 2000W heat gun was used to free the artificial sea ice from the reactor walls for ease of removal. The ice was sectioned for analysis through cross polarisation, micro ct-scanning, and for artificial sea ice bulk salinity measurements as seen in Figure 4-2. The salinity specimen was further cut into 2 cm sections from the top to bottom and allowed to melt in plastic containers. The CT and X-P specimen were covered in bubble wrap and stored in the -18°C freezer for later analyses. The choice of dimensions for each section was influenced by the reactor diameter, as well as both the length of the thermal macrotome wire and the cooling chamber housing the sample during micro ct-scanning.

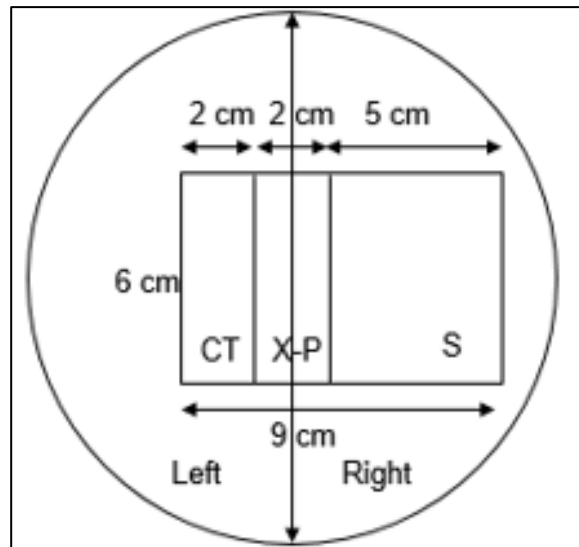


Figure 4-2. Top view of reactor after ice growth experiments showing where ice specimen were sampled from the reactor.

The traditional method used for cutting ice into thin sections for texture analysis involved the use of a microtome (Gow and Weeks, 1977), sanding and hot plate (Chester and Langway, 1958). It was observed that the mechanical abrasion from the use of a microtome and sanding techniques often loosens the poorly bonded specimen. This may result in the alteration of the natural form of the individual grains in the ice sample. Additionally, the microtome metal blades run a risk of rusting with time since they will be in contact with salt water. Furthermore, using heat may melt the sample and introduce bubbles, which alters the original ice structure (Chester and Langway, 1958). Thus, for this study, the adapted thermal macrotome technique involving the use of a 0.5 mm diameter nickel-chromium (80:20) wire was used. This wire sliced ice to create thin sections without exposing the sample to heat for longer as is the case with the hot plate. The thermal exposure and effects to the ice samples were kept negligible by following the procedure outlined by Johnson (2021).

4.2.3 Ice Salinity and Temperature Profile Measurements

A handheld AZ 8303 Cond./Temp./Logger was used to take conductivity and temperature readings from the melted sections of the artificial sea ice (as tabulated in Appendix D). This data was used to calculate artificial sea ice salinity using the [Practical Salinity Calculator](#). Thus, the artificial sea ice salinity profiles shown in Section 5.2 were plotted.

The CR5000 Campbell Scientific data logger was set to record temperature readings every 5 minutes for each probe. At the end of the experiment, data was collected as a Microsoft Excel csv file and saved as a Microsoft Excel file for further processing. Temperature readings at the end of each experimental run were used to plot the temperature profiles as seen in Appendix C. This data was also used for the investigation of artificial sea ice growth dynamics.

4.3 Analytical methods for crystal structure visualisation

4.3.1 Cross Polarisation

The maximum thickness of the artificial sea ice samples grown for this study was 9 cm, which is less than the maximum allowable thickness of 10 cm for using the cross polarisation thermal macrotome, designed by Johnson (2020), as seen in Figure 4-3. This is because it was discovered that samples with thickness greater than 10 cm broke as they were being processed into thin sections of less than 1 mm using the thermal macrotome. On average, it took 2 minutes to cut the samples with cutting time dependent on each sample's length and how smooth the ice surface was.

Since the exposure to heat is likely to change the crystal structure and size, Johnson (2020) conducted tests to prove that an average of 3 minutes exposure to heat for a thick ice section

of 10 cm length was small enough to melt the ice and change the crystal shape and size. Using the relationship between ice crystal growth and temperature during melting (Rozmanov and Kusalik, 2011), and the calculated temperature gradients of ice, Johnson (2020) found that the top 3 mm of the ice experienced greatest growth rates which caused melting of crystals. Hence, the resulting thin sections will lose the top 3 mm as the crystals would be melted and not clearly seen through cross polarisation. This implies that crystals grow and change slightly, however, the resulting cross polarisation images are a very close depiction of how they would look like *in-situ* and are representative of the ice crystal structure and texture (Johnson, 2020).

A light box and Cannon SX430 IS camera were used to take images of the further sectioned species within cross polarised sheets. The images were saved for processing later. This involved measuring the average crystal size and identifying the existing crystal textures on that section using 20 randomly selected crystals. The stratigraphy diagrams were constructed accordingly.

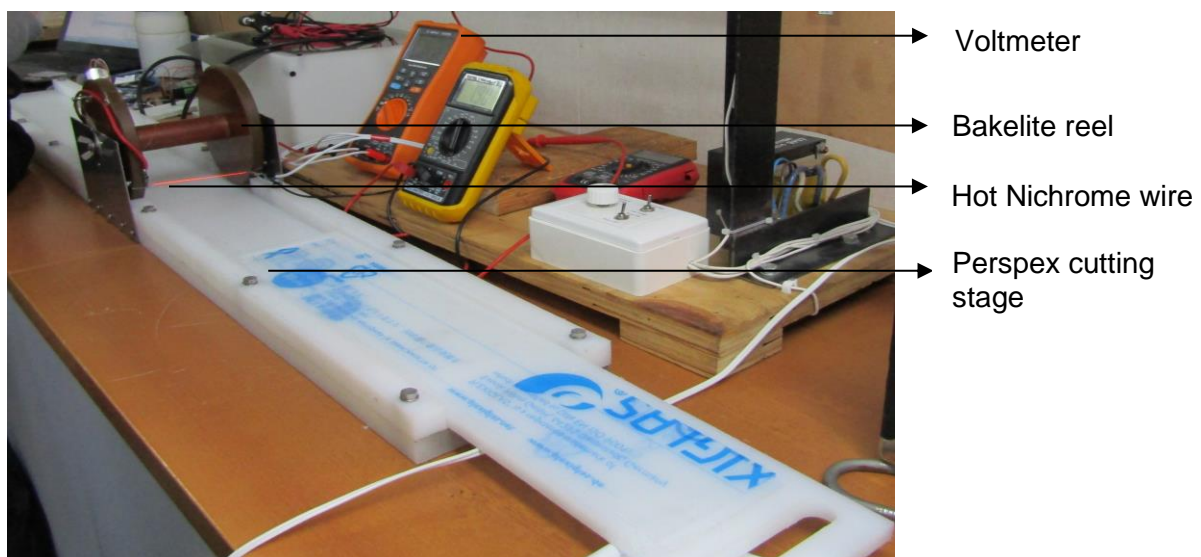


Figure 4-3 Thermal macrotome set-up showing a hot nichrome wire before sample thin sectioning.

4.3.2 X-ray Micro-Computed Tomography (μ CT)

The sections having a thickness greater than 6 cm were cut vertically in half to allow them to fit into the scanning chamber as seen in Figure 4-4.

For this work, artificial sea ice samples were scanned at the X-Sight X-Ray Services in Somerset West, Cape Town. This facility uses a high-performance and high-resolution Nikon XT H 225 Industrial scanner, using 225 kV microfocus X-ray source. The scanner has a minimum focal spot and a maximum power of the X-ray source of 1 μ m and 225 W respectively.

Each CT-scan sample that was stored after ice growth and sample was further prepared to 2 cm x 2 cm x 2 cm (length x width x height). Since the thickness of ice grown from a 3 L reactor was about 9 cm, the ice was cut into 2 sections (top and bottom), from which the 2 cubic cm sample was obtained. The sample were wrapped again and transported to the facility using a mobile cooler at -18°C. During scanning, each sample was placed inside a cooling chamber which consists of a glass jacket with ethylene glycol as a circulating coolant, maintaining a temperature of -10°C. The sample was rotated 360° for 66 minutes for data acquisition. The sample was then removed from the scanner and chamber, wrapped and placed back into the transporting cooler.

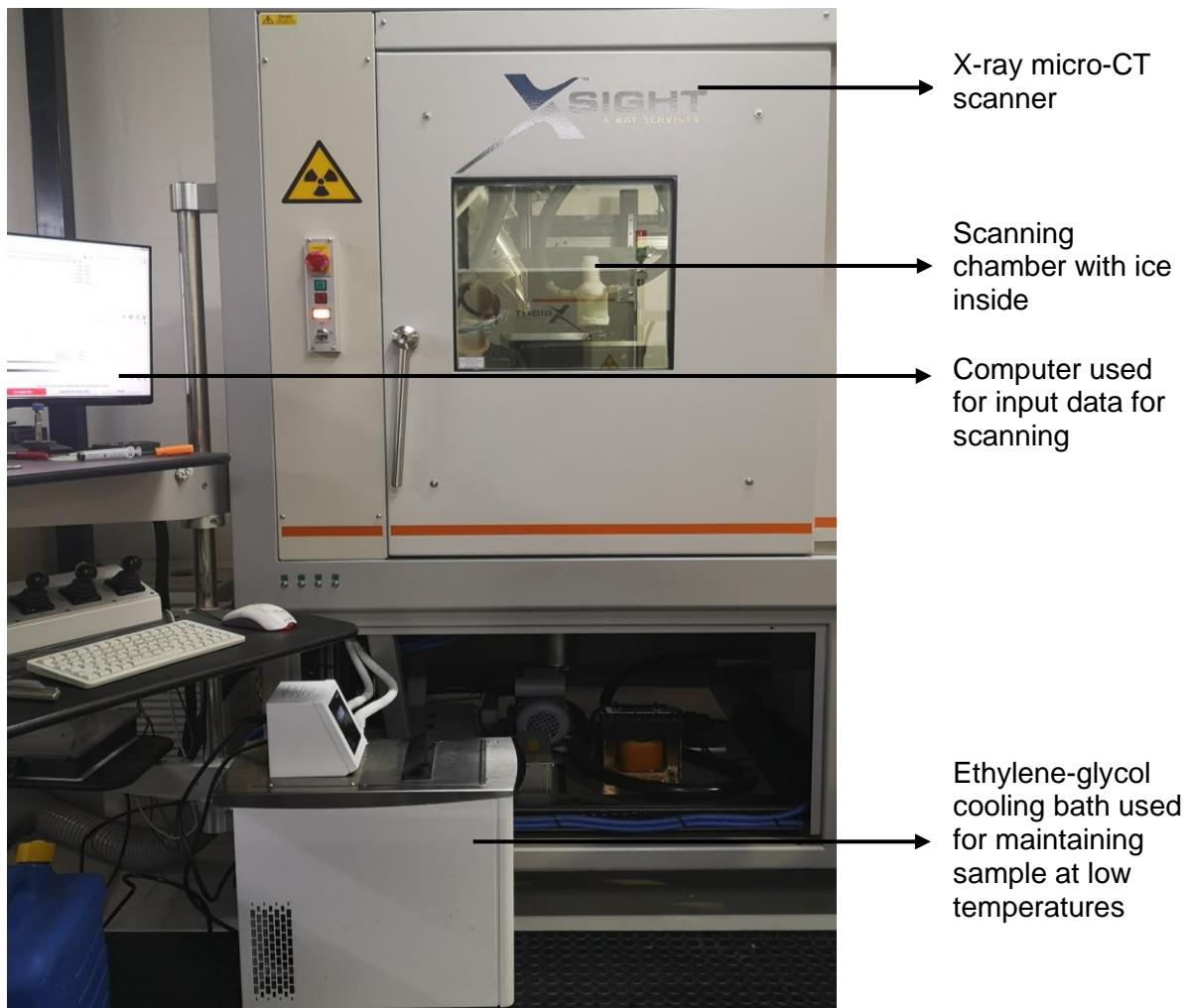


Figure 4-4 Micro-CT scanning set-up with the scanning chamber inside the scanner, the cooling bath on the floor and the user computers.

Processing of the scanner results data was done at the facility by the well-trained staff using the Volume Graphics voxel manipulation software called VGSTUDIO MAX. To analyse this data, the three-dimensional Porosity Analysis and three-dimensional Inclusion Analysis modules were used to identify and characterise brine and air inclusions within the sample. As this analysing software is exclusively for use by the facility, myVGL, a free filtered and analysed data viewer application was used to view image scans and export the sample brine and air inclusion volumes for further analysis and reporting. The data was used to explain differences in the shape and sizes of brine and air inclusions, as well as to investigate sea ice porosity.

5 Results

5.1 Justification of mixing speed

Research associated with artificial sea ice growth in the 30 L and 300 L reactors has previously been conducted by the UCT Polar Research Group, hence, for this study, the previously developed standard operating procedure (SOP) for artificial sea ice growth was followed. This SOP, however, was modified for ice growth in the 3 L reactor. The reason for downscaling of experiments was so that ice could be grown within the timeframe of this research project, thereby extending the experimental matrix and investigating several parameters.

Among other variables that had to be downscaled was the stirring speed since the one used for the 30 L reactor could not be used for the 3 L reactor. When compared to the 30 L reactor, the 3 L reactor has a small surface area, hence when the 30 L reactor stirring speed was used a vortex was created. Thus, the study for mixing parameters was necessary to determine the speed suitable for the 3 L reactor. The upper and lower limits for mixing were chosen as 0 rpm (no stirring) and 1800 rpm (the speed used for the 30 L reactor). Ice was grown at -20°C from a 10 psu starting artificial ocean salinity and the crystal structure was visualised through cross polarisation for the two mixing speeds.

Figure 5-1 A shows the cross polarisation image for ice grown without mixing. The textures observed, and their distribution through out this visual; granular, transitional, and columnar are similar to textures generally observed for natural sea ice (Eicken and Lange, 1989). However, it is necessary to stir the artificial sea water to create homogeneity and avoid the solution freezing at different temperatures. Furthermore, the salinity profile of this sample in Figure 5-2 shows that when the solution is not mixed there is a higher salt uptake and retention in the ice. From the starting artificial ocean salinity of 10 psu, the final salinity of the underlying water was

11.7 psu and the average salinity of the sample was 4.7 psu, indicating low expulsion and high retention of salt.



Figure 5-1 Visual results of ice grown at -20°C from a 10 psu solution at (A) 0 rpm, (B) 800 rpm and (C) 1800 rpm stirring speed.

Figure 5-1 C shows the cross polarisation image for ice grown at the upper speed limit, 1800 rpm, which shows the granular and transitional textures. Since this study aims to simulate the arctic conditions, it is desired to grow artificial sea ice under calm conditions, which are indicated by the presence and dominance of columnar crystals throughout the sample. Thus, the fact that this sample is dominated by the granular crystals implies that there was too much mixing in the reactor, resulting in bulk agitation. Additionally, the salinity profiles for this sample shows a slightly open “C” curve (Figure 5-2) with the least salinity uptake and retainment. The final salinity of the underlying water in this case was 12.8 psu and the average salinity was 3.2 psu. This means that more salt was expelled into the underlying water and less was retained in this sample compared to the one without mixing.

Thus, for small volume reactors, a speed less than 1800 rpm is desired to simulate artificial sea ice growth conditions suitable and comparable across different reactor volumes. A stirring speed of 800 rpm was chosen randomly as an intermediate between 0 rpm and 1800 rpm. Ice was grown and the results are shown in Figure 5-1 B, and the corresponding salinity profile in

Figure 5-2. Figure 5-1 B shows all three sea ice textures and crystal sizes that are comparable to the sample that was grown without mixing.

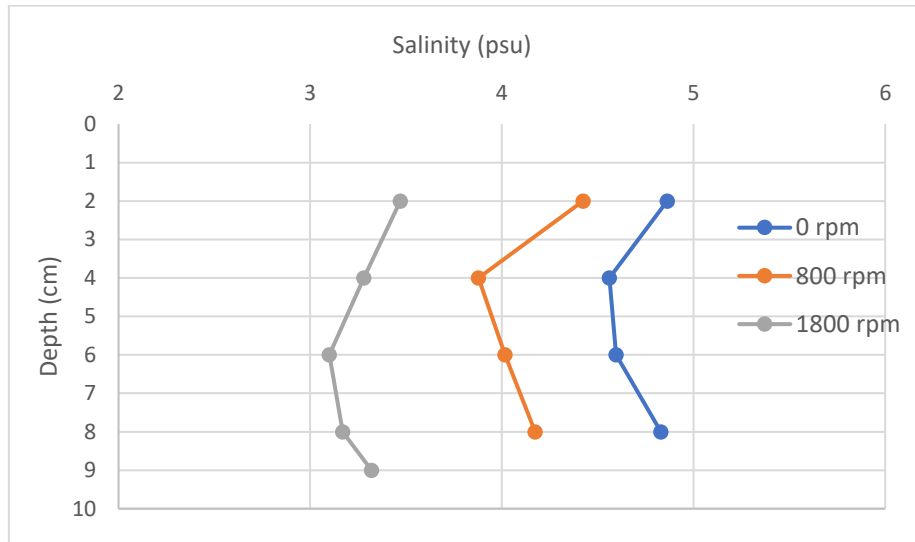


Figure 5-2 Salinity profiles for ice grown from a solution of 10 psu at -20°C for 0 rpm, 800 rpm and 1800 rpm stirring speed.

The salinity profile for the sample grown at 800 rpm stirring shows a more defined “C” shape compared to the 1800 rpm sample. The underlying water salinity was found to be 12.5 psu and average salinity of this sample was 4.1 psu. The underlying salinity of this sample was close to that of the 1800 rpm sample (with a difference of 0.3 psu), while the average salinity was close to that of the sample without mixing.

It was therefore decided to use the 800 rpm stirring speed for all experimental runs seeing that this speed does not create turbulence in the reactor, and salt retainment and the bulk artificial sea ice salinity are both between those of the samples grown at the lower and upper mixing limits.

5.2 Artificial sea ice growth dynamics

5.2.1 Method of analysis

To study sea ice thermodynamics and obtain temperature profiles, temperature data was collected during ice growth. The probe labelled T_{atm} measured the atmospheric temperature and was placed 1 cm above the water line. The next three probes were placed 1 cm, 3 cm and 5 cm below the water line respectively. These are the probes that recorded the temperature of the advancing ice cover during the growth period and used to construct the ice temperature profile at the end of the experiment. The probe 14 cm below the ice surface records the temperature of water underneath the ice. The reason for this arrangement of probes is that there is rapid ice growth at the onset of experiments which gradually decreases overtime due to the insulative properties of sea ice. Hence, a higher resolution of temperature probes is chosen at the top to capture the growth of artificial sea ice during this period. Ice grown from a solution of starting artificial ocean salinity of 10 psu at -10°C will be used to explain the process of data analysis and the construction of temperature profiles.

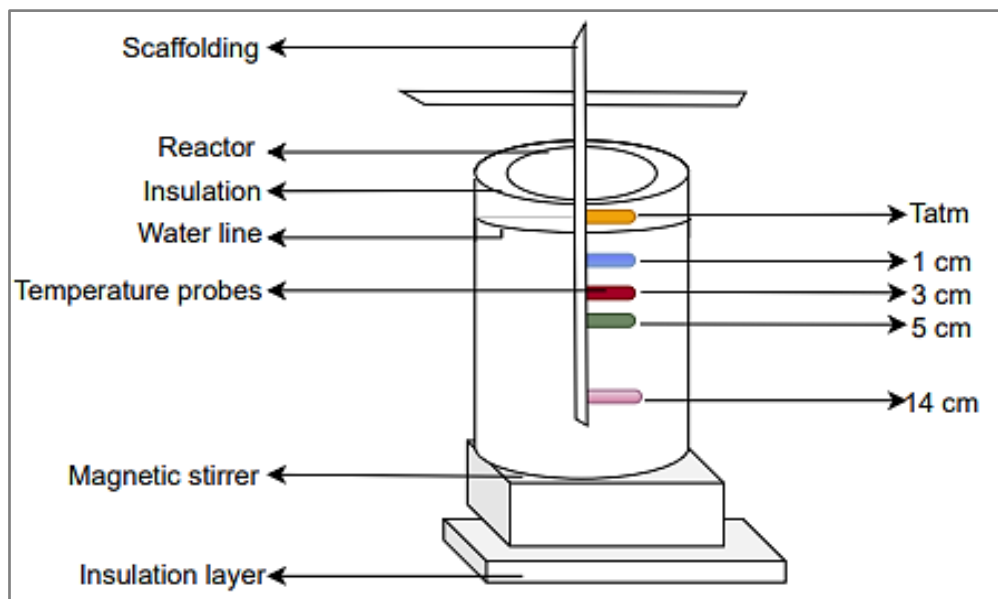


Figure 5-3 Reactor schematic showing the arrangement of temperature probes

Temperature vs. time graphs were drawn for each probe in the reactor and these are shown in Figure 5-4. Each probe in the reactor is illustrated with the same colour on Figure 5-4 as coded on the probes in Figure 5-3. From Figure 5-4, the solution freezing point, time taken to freeze, and ice growth rate can be deduced. The starting point of all curves (shown by a red arrow in Figure 5-4) is at a temperature of -0.69°C and 0 hours. This shows that the surface of the 10 psu solution started freezing at a temperature of -0.69°C . The drop of each curve from -0.69°C , shown by orange arrows, indicates ice formation at the specific depth below the ice surface. This also shows how long it took for the ice front to move from one location to the other. Hence this can be used to estimate how long it took for the ice to grow by a certain thickness. Probe 1 started freezing after 0.9 hours, probe 3 after 4.2 hours, and probe 5 after 8.5 hours. As expected, this implies that ice formation starts at the top of the reactor and grows downwards.

The gradient of each curve, indicating the cooling rate at the given position, was calculated for the first four hours (indicated by green ovals) after freezing began. The gradient of probes 1, 3, and 5 were 1.08°C/hr , 0.49°C/hr , and 0.37°C/hr respectively. It can be seen that the gradient decreases with ice depth. This implies that the rate of change of temperature is higher near the surface of the ice and decreases as ice thickness increases. The rate of change of temperature decreases because as ice grows thicker, the water is further separated from the cold source at the surface. The ice sheet now serves as an insulator thus providing resistance to the exchange of heat between the air and the artificial ocean. Thus, the growth rate of ice at this point depends on the temperature gradient in the ice sheet and its conductivity. The growth rate of this ice was estimated to 0.33 cm/hr . This was estimated by working out how long it took for ice to grow by 2 cm (from 1 cm to 3 cm and 3 cm to 5 cm, shown by black double headed arrows) for a given temperature point or, how long each probe takes to reach any given temperature.

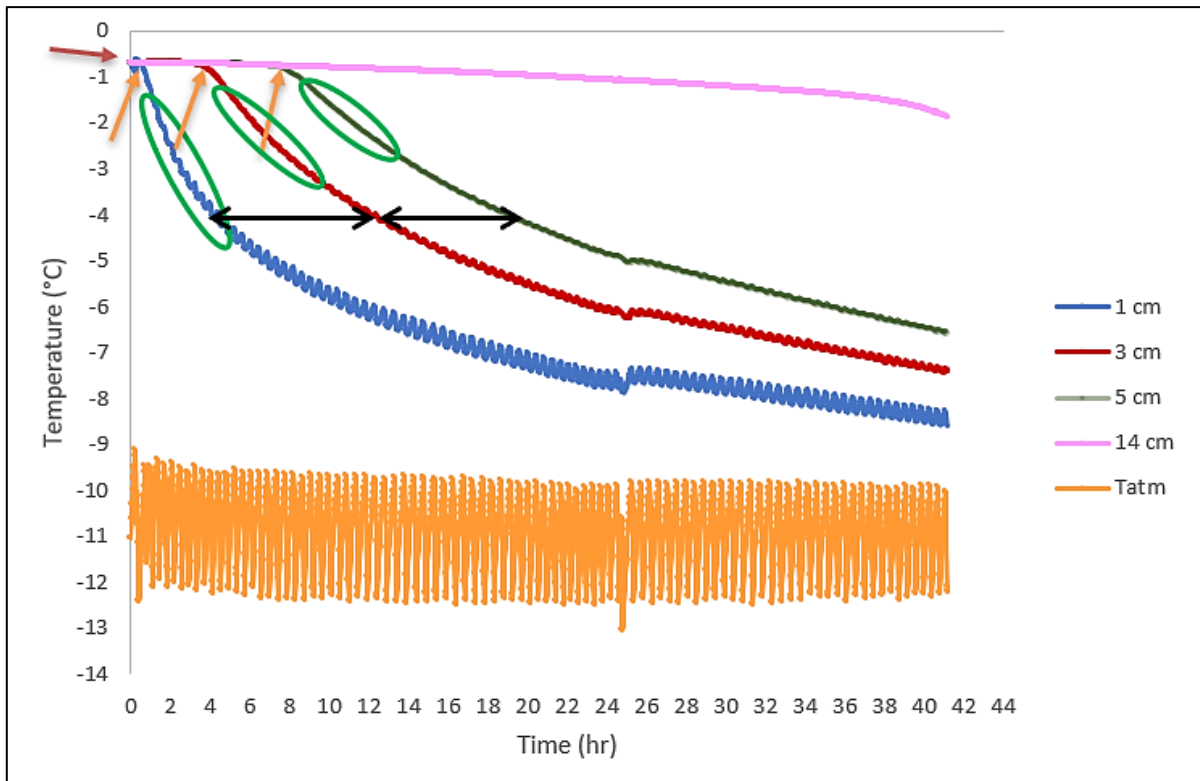


Figure 5-4 Temperature time graph showing the growth dynamics for ice grown at -10°C from a solution of starting artificial ocean salinity of 10 psu.

To estimate the growth rate using -4°C for example, it takes 4 hours for probe 1 to reach -4°C , 12 hours for probe 3, and 20 hours for probe 5. Since probe 1 and 3 are 2 cm apart, the growth rate between these two points will be given as the ratio between 2 cm and 8 hours (the difference between 12 hours and 4 hours), yielding 0.25 cm/hr . The average for all temperature points gives a growth rate of 0.33 cm/hr . This ice grew to a thickness of 8 cm for a total duration of 42 hours. This, however, does not agree with the average growth rate estimated. This is because the average growth rate gives an indication of how long the ice would have grown per time unit over the entire duration of the experiment. However, it does not show how the ice front progressed during the experiment, how fast the ice grew during the initial stages, nor how it slowed down at the end.

Table 5.1 illustrates the summary of findings as discussed in this section for ice grown at -10°C from a solution of starting artificial ocean salinity of 10 psu. In the following sections, 5.2.2 to 5.2.5, only summary tables will be shown and the temperature vs. time graphs can be seen in Appendix C.

Table 5.1 Summary of findings from the Temperature time graph showing the growth dynamics for ice grown at -10°C from a solution of starting artificial ocean salinity of 10 psu.

	Probe 1	Probe 3	Probe 5
Freezing point ($^{\circ}\text{C}$)	-0.7	-0.72	-0.74
Time taken to freeze (hr)	0.9	4.2	8.5
Gradient ($^{\circ}\text{C/hr}$)	1.08	0.49	0.37
Average growth rate (cm/hr)	0.33		
Ice thickness after 42 hr (cm)	8		

Probe 14 was positioned 14 cm below the surface of the water, such that it records the temperature of the water underneath ice during growth. This probe measured the freezing point of the solution, -0.7°C , as established above, and slightly dropped below -1°C after 16 hours of the experiment. This change in the probe temperature at this location is due to the change in the freezing point of the solution as the ice is forming due to the increase in salinity of the underlying solution by the process of gravity drainage. Hence, the temperature is maintained at the freezing point. This also explains the observed slight drop of the curve.

The T_{atm} probe was expected to read -10°C , the growth temperature. However, it fluctuated between -9.5°C and -12.5°C , which averages to -11°C , 1°C off the set temperature.

5.2.2 Effects of varying the starting artificial ocean salinity on artificial sea ice growth dynamics

To study the effects of changing salinity on artificial sea ice thermodynamics, a similar graph to the one shown in Figure 5-4 was constructed for ice grown at -10°C from solutions of varying starting artificial ocean salinities; 10 psu, 20 psu, and 30 psu (Figure C. 1 in Appendix C). These graphs were analysed as per Section 5.2.1 and, results were summarised in Table 5.2.

It can be seen from Table 5.2 that the freezing point decreases with increasing salinity. This is because the presence of salt depresses the freezing point of the solution. Equation 2-1, developed by Maykut (1986) shows a relationship between freezing point and salinity of any given solution. However, freezing points calculated from this equation deviate slightly (± 0.2) from the freezing points obtained from the temperature data. This could be attributed to assumptions made and the geometry of the system used, which were not stated from the development of Equation 2-1. Additionally, time taken to freeze the solution increases with increasing salinity. This follows from the fact that the more saline the solution is, the longer it will take to reach its freezing point, which is lower than that of the less saline solution.

Looking at the gradient of each curve for the three solutions, the rate of change in temperature at the same depth in ice is greater for a less saline solution. This rate of change in temperature gives an indication of the cooling rate of the ice. Thus, implying that a different degree of cooling is experienced at the same depth in ice for solutions of different salinity. The average growth rates for the 10 psu and 20 psu ice are the same, but decrease for the 30 psu ice by 0.11 cm/hr. It was noted that the 30 psu ice grew to the same thickness as the 20 psu ice, 1 cm more than the 10 psu ice. It was expected that the 10 psu ice would grow thicker than the 20 psu, which would be thicker than the 30 psu for the same growth period. This could be due to the underlying solution reaching a critical salt concentration at which growth is impeded, hence hindering ice growth.

Looking at the growth rates, it can be deduced that the 30 psu ice reached this critical state after the 10 psu and 20 psu ice. Thus, it can be assumed that beyond this critical point, the effect of starting artificial ocean salinity becomes negligible.

Table 5.2 Summary of findings from the Temperature time graphs showing the growth dynamics for ice grown at -10°C from solutions of starting artificial ocean salinities of 10 psu, 20 psu and 30 psu.

	10 psu	20 psu	30 psu
Freezing point (°C)	-0.7	-1.0	-1.8
Time taken to freeze (hr)	0.9	1.8	3.4
Gradient – 1 cm (°C/hr)	1.08	0.55	0.24
Gradient – 3 cm (°C/hr)	0.49	0.33	0.16
Gradient – 5 cm (°C/hr)	0.37	0.22	0.14
Growth rate (cm/hr)	0.33	0.33	0.22
Thickness after 42 hr (cm)	8	9	9

Temperature profiles for the three ice samples were constructed using the average of the last 10 entries of the temperature time data to give the temperature attained by each probe (depth) at the end of the growth period. These are shown in Figure 5-5.

The temperature profiles all follow a linear trend which is characteristic of a temperature profile of first-year natural sea ice (Eicken and Petrich, 2017). The temperature 1 cm above the ice surface was around -8.8°C, -7.9°C, and -6.3°C for 10 psu, 20 psu, and 30 psu respectively. This implies that the surface of the ice grown at 10 psu experienced temperatures closer to the ambient temperature (-10°C) compared to the 20 psu and 30 psu ice. The probes in the 10 psu ice recorded lower temperatures for each depth in ice at the end of the experiment compared to the 20 psu and 30 psu ice. This is in agreement with the results in Table 5.2 since

the rate of change of temperature per unit depth is greater during the course of the experiment for the 10 psu ice, followed by the 20 psu, and lastly the 30 psu. The average gradients of the curves: 0.5 °C/cm, 0.4 °C/cm, and 0.29 °C/cm for the 10 psu, 20 psu, and 30 psu samples respectively, show that the cooling rate of the 10 psu was higher than that of the 20 psu and 30 psu at the same depth in ice.

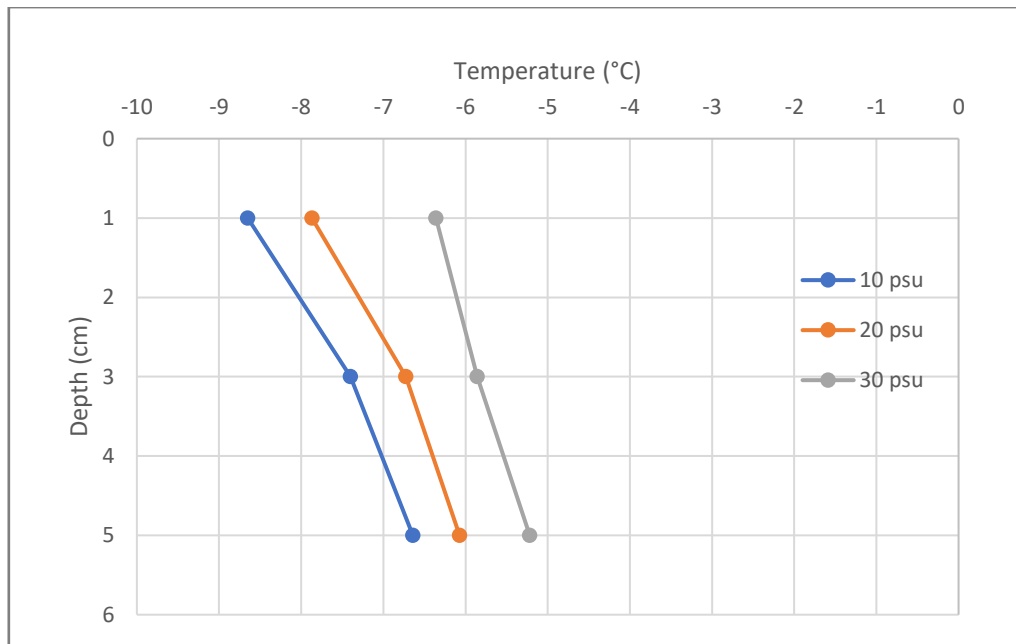


Figure 5-5 Temperature profiles for ice grown at -10°C from solutions of starting artificial ocean salinities of 10 psu, 20 psu, and 30 psu.

Salinity profiles for the three ice samples are shown in Figure 5-6. The salinities of the top 2 cm of 10 psu and 20 psu samples were 3.5 psu and 5.0 psu respectively, while that of the 30 psu sample was significantly higher at 10.6 psu as seen in Figure 5-6. This is a result of the solution having a higher starting artificial ocean salinity than the 10 psu and 20 psu solutions. The salinity of the 10 psu sample first decreases for the first 4 cm, increases slightly for the next 2 cm, and further increase towards the bottom of the sample. The salinity of the 20 psu sample decreases gentler than the 10 psu sample for the upper 4 cm and increases at a slightly higher rate than the 10 psu sample at the bottom part of the sample. The salinity of the 30 psu

sample decreases sharply in the upper 4 cm of the sample, increases gently in the next 2 cm, and increase sharply for the bottom part of the core.

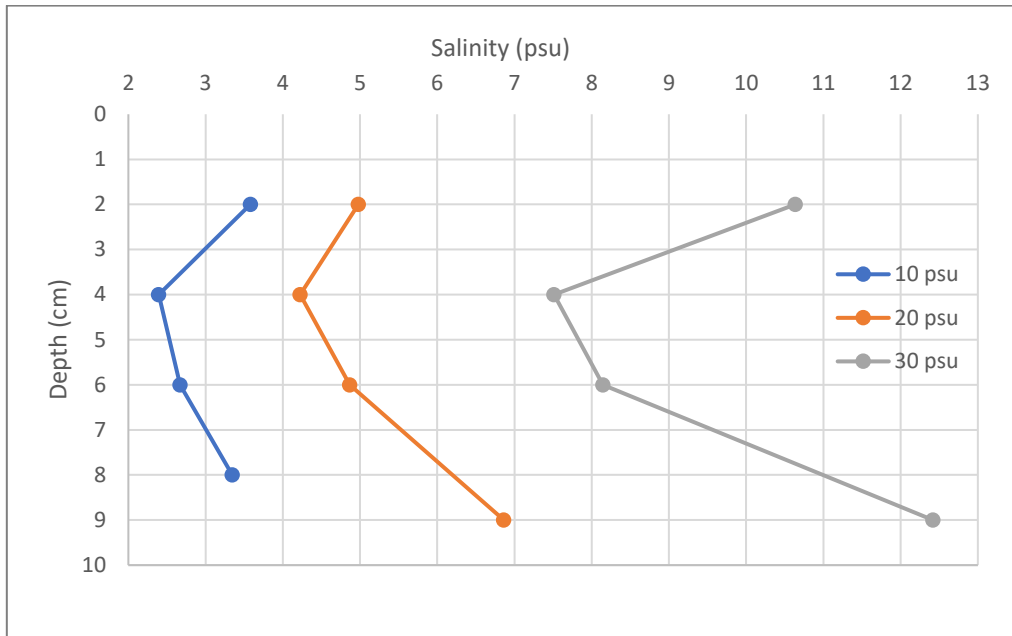


Figure 5-6 Salinity profiles for ice grown at -10°C from solutions of starting artificial ocean salinities of 10 psu, 20 psu, and 30 psu.

The salinity profiles of the ice grown at -10°C all exhibited the ‘C-type’ curves for all samples with the “C” much more defined for the 30 psu than the 10 psu and 20 psu samples. The curvature of the salinity profile and the higher salinity at the top of 30 psu sample could be explained by the dependence of both the freezing temperature and the temperature of maximum density on the salinity (Petrich and Eicken, 2017). Below 25 psu, the temperature of maximum density water decreases, however, it remains above the solution freezing point. The water stratifies and freezing is immediate after the freezing point is reached. Above 25 psu, the temperature of maximum density water decreases below the solution freezing point, meaning that the freezing point is reached before the temperature of maximum density water. Thus, the whole water column will be cooled and mixed before freezing begins. Therefore, the

freezing in the 30 psu is delayed and this allows more time for brine expulsion due to convection at the top and gravity drainage at the bottom of the sample (Eicken, 1992).

The 30 psu sample is more of a reflection of the expected salinity profile of first-year sea ice. Although the bulk salinity of the 30 psu sample is higher than that generally reported (Weeks and Ackley, 1982) for first-year sea ice (between 4 psu – 7 psu), this can be attributed to the starting artificial ocean salinity of 30 psu being higher for a smaller reactor volume. Although this starting salinity is close to the ocean salinity, the 3 L volume reactor might cause impedance in brine expulsion. This is due to the limited space for salt circulation in the reactor, compared to lower saline solutions in the same reactor volume, and in the ocean environment.

Brine convection also play a huge role here. Solutions of starting artificial ocean salinity below 24.7 psu have the temperature of maximum density higher than the solution freezing temperature (Maykut, 1985). Thus, water freezes and stratifies when freezing point is reached since the solution density keeps decreasing. However, the solution of starting salinity above 24.7 psu has the temperature of maximum density below the freezing temperature, hence, the solution density increases as the solution is being cooled. When the freezing temperature is reached, freezing will be delayed until the whole water column is cooled through brine convection. Since ice growth in the 3 L reactor was limited by time and space, gravity drainage was restricted, hence, more brine was retained. The 20 psu sample revealed bulk salinity comparable to that of sea ice, while the 10 psu sample revealed lower bulk salinities.

As per the findings of Wettlaufer *et al.* (1997), the critical ice thickness is smaller when the initial solution concentration is higher for a given surface temperature. This suggest that the cooling rate is lower at higher salinities due to compositional convection as explained above.

5.2.3 *Effects of varying ambient temperature on artificial sea ice growth dynamics*

To study the effects of changing temperature on artificial sea ice growth dynamics, a similar graph to the one shown in Figure 5-4 was constructed for ice grown from solutions of the same starting artificial ocean salinity of 30 psu at -20°C, -10°C, and -5°C (Appendix C). These graphs were analysed as per Section 5.2.1 and, results were summarised in Table 5.3. It was observed that ice grown at -5°C only grew to about a thickness close to 1 cm after 16 hours thus, only recording ice temperatures for the probe positioned at 1 cm below the surface.

It can be seen from Table 5.3 that the freezing point temperature is slightly different by ± 0.1 . It was expected that the freezing points be the same since these solutions have the same starting salinity. Hence, this 0.1 difference is assumed negligible. Additionally, time taken to freeze the solution increases with increasing temperature. This follows from the fact that artificial sea ice growth at a higher ambient temperature (-10°C) experiences a lower cooling rate than growth at a lower ambient temperature (-20°C).

Looking at the gradient of each profile for the two samples, it can be seen that the rate of change in temperature at the same depth of ice is greater for the sample grown at -20°C, and smaller for the sample grown at -10°C. This implies that artificial sea ice grown at a lower ambient temperature had a higher cooling rate than that growth at a higher ambient temperature.

Table 5.3 Summary of findings from the Temperature time graphs showing the growth dynamics for ice grown at -20°C and -10°C from solutions of starting artificial ocean salinity of 30 psu.

	-20°C	-10°C
Freezing point (°C)	-1.9	-1.8
Time taken to freeze (hr)	0.7	3.4
Gradient – 1 cm (°C/hr)	0.78	0.24
Gradient – 3 cm (°C/hr)	0.55	0.16
Gradient – 5 cm (°C/hr)	0.44	0.14
Growth rate (cm/hr)	0.45	0.22
Thickness after 16 hours (cm)	9	3

The estimated growth rates show that the sample grown at -20°C has a higher growth rate than the -10°C sample. This is due to the higher cooling rate experienced by this sample since at the same depth for both samples, lower temperatures were reached first by the sample grown at -20°C. Thus, implying that the ice cover advancing rate was higher for the sample grown at -20°C.

During the initial stages of ice growth, temperature was observed to be decreasing sharply for the depth 1 cm below the water line for both the -20°C and -10°C temperature profiles. This is because the heat transfer rate is higher at the onset of formation. It decreases as the ice thickness increases due to ice insulative properties (Wiese, 2012). At a depth of 14 cm below the ice, temperatures were maintained at the freezing point of the solution, $-2 \pm 0.2^\circ\text{C}$, for the most part of the experiment before decreasing towards the end of the experiment, similar to what was observed by Wettlaufer *et al.* (1997). This is because during ice formation, the salinity of the underlying water increased due to brine expulsion, thus, decreasing the solution freezing point.

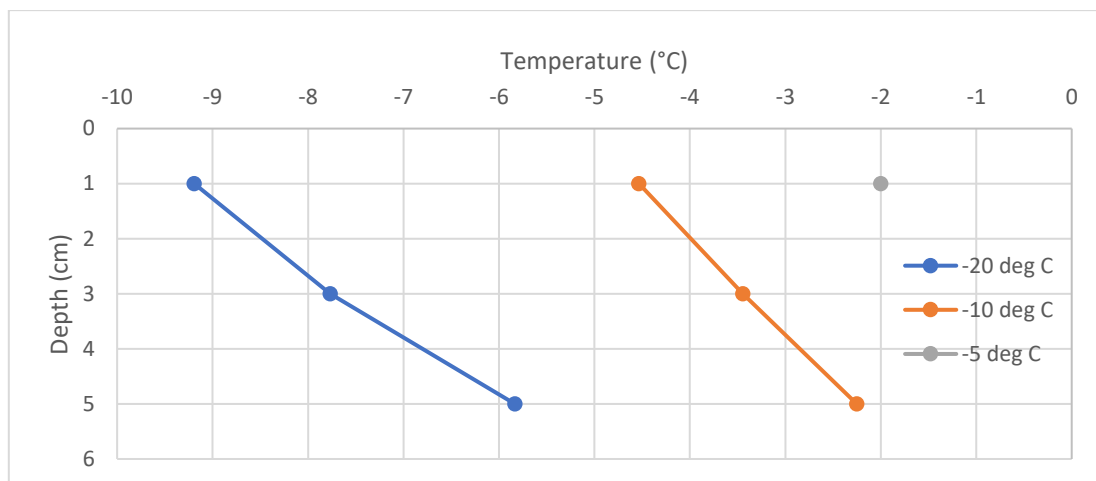


Figure 5-7 Temperature profiles for ice grown from solutions of starting artificial ocean salinity of 30 psu at -20°C, -10°C, and -5°C at the end of 16 hours.

The temperature profiles shown in Figure 5-7 were constructed using the temperature readings obtained after 16 hours of growth for ice grown from a solution of starting artificial ocean salinity of 30 psu at temperatures of -20°C, -10°C, and -5°C. The temperature 1 cm below the ice surface for ice grown at -20°C was -9.2°C, while for the sample grown at -10°C and -5°C, was -4.4°C and -2°C respectively. Both the -20°C and -10°C profiles showed a linear behaviour, while only the temperature at 1 cm below the ice surface was recorded for the sample grown at -5°C. This is attributed to the lower cooling rate delivered by -5°C ambient temperature, implying that it needed more time to grow to the same thickness as the ice grown at -20°C and -10°C at any given time.

The -20°C sample has an initial temperature lower than that of -10°C and -5°C due to the difference in ambient temperature. In natural sea ice, this difference would be interpreted as a result of sea ice sampled from different sites with different meteorological conditions. Temperature increases with ice depth because cooling is provided from the ice surface, thus, heat is moving in an upwards direction. Therefore, the ice-water interface temperatures are the freezing point temperatures of the individual solutions. The average change in temperature per unit depth for -20°C and -10°C were calculated to be 0.82 °C/cm and 0.57 °C/cm

respectively. This shows that at any given depth in ice the change in temperature of the sample grown at -20°C was larger, thus higher rate of heat transfer than the sample grown at -10°C and -5°C . Therefore, the sample grown at -20°C experienced a higher cooling rate than the samples grown at -10°C and -5°C at the same ice depth.

The relationship between sea ice growth rate and thickness (Wettlaufer, 1997; Cox and Weeks, 1988) can be used as well here. A larger ice thickness was observed for ice that had a lower surface temperature. This is because the temperature as a driving force promoted convection, thus, increasing the solid fraction (Wettlaufer, 1997). Furthermore, once the critical thickness is reached, ambient temperature was no longer the driving force, ice growth became a sole function of the ice thickness (Wettlaufer, 1997).

Salinity profiles for the three samples were plotted using the salinity readings measured from the ice melt at the end of the growth period (see Appendix D). These are shown in Figure 5-8.

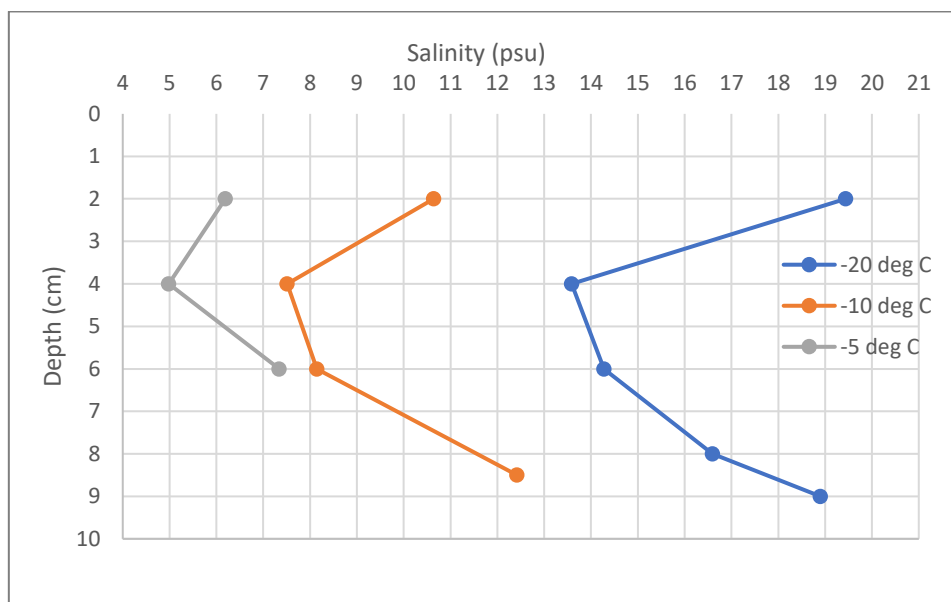


Figure 5-8 Salinity profiles for ice grown at -20°C , -10°C , and -5°C from solutions of starting artificial ocean salinity of 30 psu at the end of 16 hours.

The artificial sea ice surface salinities for the -5°C, -10°C, and -20°C are 6.19 psu, 10.6 psu, and 19.4 psu respectively, as seen from Figure 5-8. All samples show a decreasing salinity trend for the first 3 cm, however, the rate of decrease (change in salinity per change in ice thickness) is higher for the -20°C sample and lower for the -5°C sample. The salinities increase towards the bottom of the samples, and the same trend as in the rate of decrease in salinity is observed.

All three samples resemble a “C-curve” shape salinity profile. However, the “C-curve” is more defined for the sample grown at -20°C. This can be attributed to the fact that at lower ambient temperatures, ice grows such that the structure has smaller but many brine inclusions (Weeks & Ackley, 1982). Furthermore, Gow *et al.* (1987) states that the faster the growth rate the higher the bulk salinity of the sample. This is because lower ambient temperatures result in rapid ice growth, hence, the competition between brine and heat convection. Thus, -20°C sample retain more brine than the -10°C and the -5°C samples. This is also justified by the bulk salinities: 6.2 psu, 9.68 psu, and 16.6 psu for -5°C, -10°C, and -20°C respectively, showing an increase in bulk salinity with decreasing ambient temperature.

5.2.4 Effects of varying reactor volume on artificial sea ice growth dynamics

Generally, artificial sea ice studies have been performed for ice grown from large reactors, with a 50 L reactor being the smallest volume reactor reported in literature (Haas *et al.*, 1999). It is desired to study the effect of varying reactor volume on artificial sea ice growth dynamics and whether there are any growth parameters favoured in one reactor size than the other.

For the purpose of this study, artificial sea ice was grown from two different reactor volumes, 3 L and 30 L at the same ambient temperature and starting artificial ocean salinity: -20°C and 30 psu. The temperature vs. time graphs were constructed (Figure C. 3 in Appendix C) with the findings summarized in Table 5.4.

It can be seen from Table 5.4 that the freezing point temperature is the same for both reactor volumes. This was expected since these solutions have the same starting artificial ocean salinity. The time taken to freeze the solution increased with increasing reactor volume. Additionally, at any given ice depth, temperatures of the sample grown from the 3 L reactor were lower than those of the sample grown from a 30 L reactor. This can be attributed to the fact that heat transfer is enhanced in the reactor with a higher surface to volume ratio (Mukaromah *et al.*, 2016). The surface to volume ratio was calculated to be 103 cm⁻¹ for the 3 L reactor and 44 cm⁻¹ for the 30 L reactor. Thus, implying that heat transfer was enhanced in the 3 L reactor, hence the above observations suggest the ice that grew from the 3 L reactor experienced a higher cooling rate. This is supported by the average estimated growth rate as it is higher for the 3 L reactor sample.

Table 5.4 Summary of findings from the Temperature time graphs showing the growth dynamics for ice grown from the 3 L and 30 L reactor at -20°C and starting artificial ocean salinity of 30 psu.

	3 L	30 L
Freezing point (°C)	-1.8	-1.9
Time taken to freeze (hr)	0.7	1.1
Gradient – 1 cm (°C/hr)	0.74	0.72
Gradient – 3 cm (°C/hr)	0.55	0.43
Gradient – 5 cm (°C/hr)	0.44	0.32
Growth rate (cm/hr)	0.46	0.33
Thickness after 16 hours (cm)	9	4

Temperature profiles are shown in Figure 5-9 for ice grown from a solution of 30 psu at -20°C from a 3 L and 30 L reactor at the end of a 16-hours growth period. The temperature at the depth of 1 cm below the ice surface of the sample grown from the 3 L reactor was -9.2°C, while

that of the sample grown from the 30 L reactor was -8.4°C . Both profiles show a linear behaviour as expected for the temperature profile of young sea ice (Maykut, 1985).

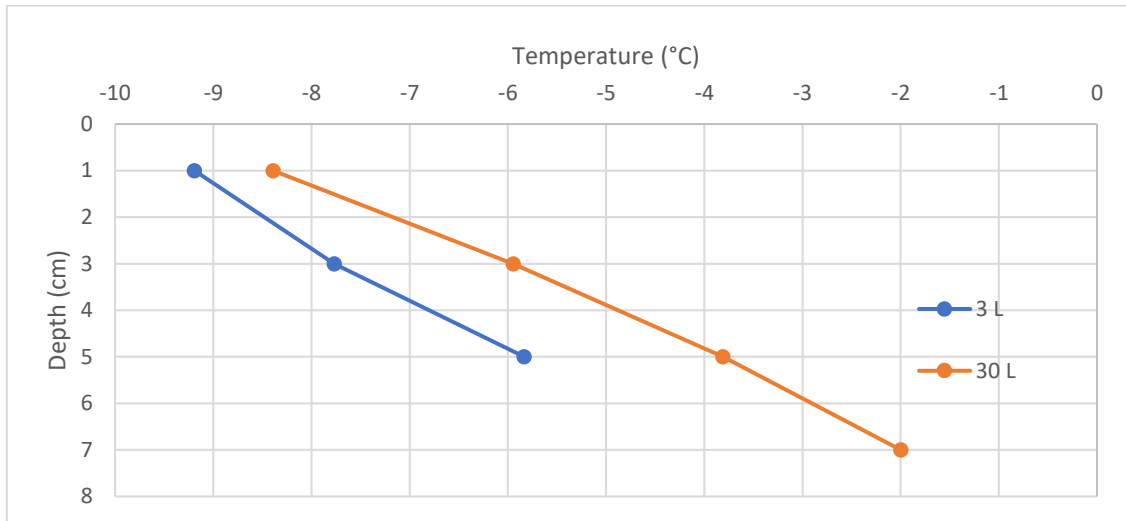


Figure 5-9 Temperature profiles for ice grown from solutions of starting artificial ocean salinity of 30 psu at -20°C from a 3 L and 30 L reactor.

Figure 5-9 also shows that at any given ice depth, the sample grown from the 3 L reactor experienced lower temperatures than that from the 30 L reactor. This is expected since findings in Table 5.4 show that the change in temperature at any given ice depth is higher for the 3 L sample than the 30 L sample. The estimated change in temperature per given ice depth for the samples grown from the 3 L and 30 L are $0.84^{\circ}\text{C}/\text{cm}$ and $1.15^{\circ}\text{C}/\text{cm}$ respectively. This is the opposite of what is expected according to the findings in Table 5.4 as it implies that the change in temperature was higher per given ice depth in the sample grown from the 30 L reactor, not from the 3 L reactor. This can be attributed to the fact that once the critical thickness in the 3 L reactor has been reached, the growth rate slows down due to the slow rate of conduction over that of convection. In the 30 L reactor however, the critical thickness is reached later, hence, the effects of conduction were experienced later.

The salinity measurements within the first 2 cm of the samples grown from the 3 L and 30 L reactors were 19.5 psu and 12 psu respectively, as seen in Figure 5-10 (see Appendix D for salinity measurements).

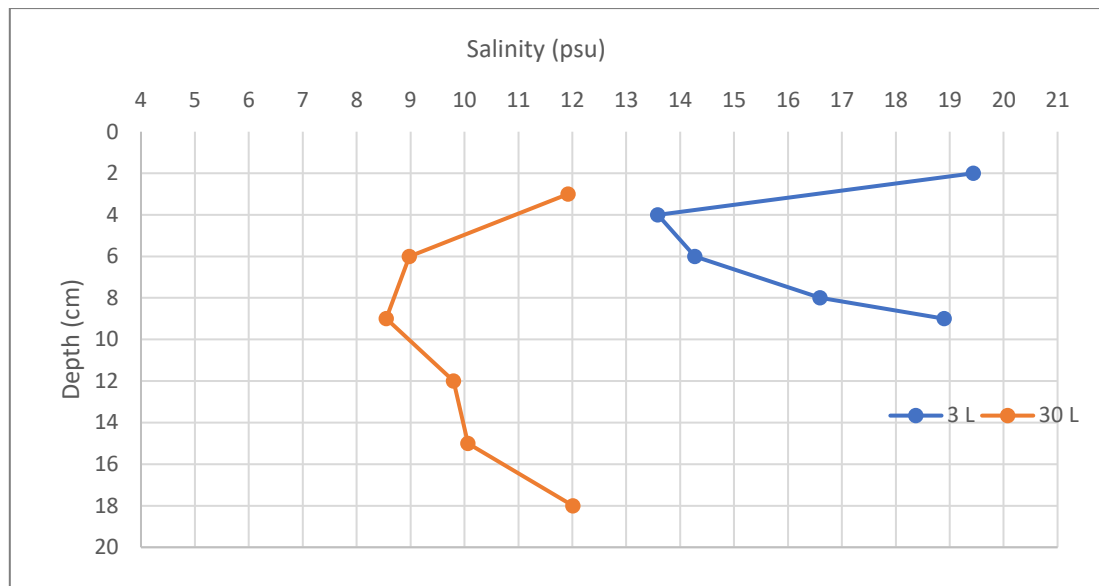


Figure 5-10 Salinity profiles for ice grown from solutions of starting artificial ocean salinity of 30 psu at -20°C from a 3 L and 30 L reactor.

For both samples, there is a decrease in salinity for the top 3 cm of the ice, a further decrease for the next 2 cm in the 30 L sample, and an increase for the remainder of the ice length for both samples. The estimated rate of salinity decrease, and increase are higher for the 3 L reactor sample (2.93 psu/cm and 1.27 psu/cm respectively) than for the 30 L sample (0.56 psu/cm and 0.39 psu/cm respectively).

Both sample salinity profiles exhibit a “C-curve” shape, with the “more defined” C profile showing that the sample grown from the 3 L reactor retained more brine. This can be attributed to the higher cooling rate experienced by this sample (Figure 5-4 and Figure 5-9), thus, offering insufficient time for brine expulsion. The underlying water salinity was 14.1 psu and 11.0 psu for 3 L and 30 L respectively, indicating higher brine expulsion in the 3 L reactor. Similar to the effect of decreasing ambient temperature, the observed high salt retention on the 3 L reactor

sample is due to the higher growth rate (Table 5.4), which in turn accelerates the desalination processes. The normalised bulk artificial sea ice salinities were found to be 11.5 psu and 10.9 psu for 3 L and 30 L respectively, indicative of more brine trapped in the 3 L reactor sample.

5.2.5 Effects of the presence of EPS on artificial sea ice growth dynamics

To study the effects of the presence of EPS on artificial sea ice growth dynamics, a temperature vs. time graph was plotted for ice grown from a 30 psu solution at -10°C with and without the addition of EPS (Appendix C). These graphs were analysed as per Section 5.2.1 and, results were summarised in Table 5.5.

It can be seen from Table 5.5 that the freezing point temperature of the two samples is different: -1.8°C and -2.2°C for the sample with no EPS and the one with EPS respectively. Although the starting artificial ocean salinity is the same, Table 5.5 shows that the growth dynamics are different. Additionally, time taken to freeze the solution increases almost twice in the presence of EPS. Implying that the presence of EPS causes a further depression to the freezing temperature on top of the depression caused by the solution having a high starting artificial ocean salinity as seen in Table 5.2.

The rate of change in temperature per given ice depth is slightly higher for the sample without EPS, implying that slightly more cooling is experienced in the sample without EPS than that with EPS. The average growth rate of the sample with EPS is 0.18 cm/hr, slightly lower than that of the sample without EPS (Table 5.5), indicating the delayed growth rate. The two samples, however, grew to the same thickness over a growth period of 42 hours. This can be explained by the small difference between the gradients of corresponding probes from the reactor with and without EPS. These differences are 0.08, 0.02, and 0.05 for the probe positioned 1 cm, 3 cm, and 5 cm from the water surface, respectively, and are also reflected in the small difference (0.04 cm/hr) between the growth rates. This implies that although the

presence of EPS increases salt concentration in the reactor (Krembs et al., 2011), it does not significantly decrease the overall growth rate towards the end of the growth period.

Furthermore, since the addition of EPS delayed freezing and resulted only in slightly slower growth dynamics, this could be due to the solution recognising EPS as an “impurity”, thus, increasing the rate of nucleation (Lewis *et al.*, 2015), simultaneous to the decreasing growth rate. This assumption is made based on the fact that the 3 L reactor offers a very small volume for growth dynamics. Thus, any changes to the system may have noticeable consequences.

Table 5.5 Summary of findings from the Temperature time graphs showing the growth dynamics for ice grown at -10°C from solutions of starting artificial ocean salinity of 30 psu with and without EPS.

	No EPS	EPS
Freezing point (°C)	-1.8	-2.2
Time taken to freeze (hr)	3.4	6
Gradient – 1 cm (°C/hr)	0.24	0.16
Gradient – 3 cm (°C/hr)	0.16	0.14
Gradient – 5 cm (°C/hr)	0.14	0.09
Growth rate (cm/hr)	0.22	0.18
Thickness after 42 hours (cm)	9	9

The temperature profiles shown in Figure 5-11 were constructed using the temperature readings obtained after 42 hours of growth for ice grown from a solution of 30 psu at -10°C with and without EPS. Both profiles show a linear behaviour. The profiles are very close to each other. This implies that at any given ice depth, the cooling rates experienced by both samples are not far from each other. This agrees with the estimated rate of change in temperature per given depth in ice, given in Table 5.5.

The estimated average change in temperature per unit depth for the sample without EPS and the one with EPS is 0.42 °C/cm and 0.48 °C/cm respectively. This is expected since the rate of change of temperature per given ice depth is almost the same throughout the length of the sample. This also shows that the growth dynamics for the sample with EPS were slower at the beginning of ice growth and increased towards the end of the growth period. Thus, explaining both ice grown with and without EPS reaching the same thickness after 42 hours of the growth period (Table 5.5).

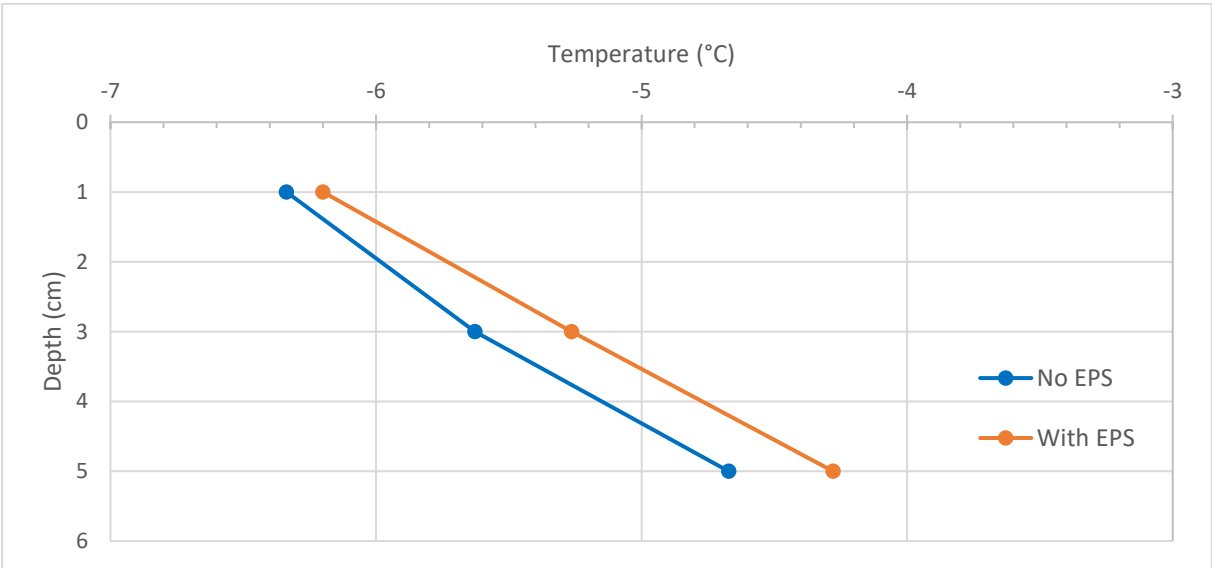


Figure 5-11 Temperature profiles for ice grown at -10°C from solutions of starting artificial ocean salinity of 30 psu with and without EPS.

Figure 5-12 shows the salinity profiles for both samples grown with and without EPS. The salinities within the top 2 cm of the samples were 10.6 psu and 24.4 psu for sample with no EPS and the one with EPS respectively. Although the samples both grew from solutions of same starting artificial ocean salinity, the sample with EPS has a higher starting salinity and overall brine retention. This is also evident in the observed depression in the freezing temperature and delayed taken to freeze (Table 5.5).

The sample without EPS shows a decrease in salinity in the top 4 cm of the ice, and an increase in the remaining 5 cm at the bottom of the sample. The sample with EPS, however, shows a decrease in the salinity throughout the sample. Therefore, exhibiting a “C-curve” and a “J-curve” salinity profile for sample without and with EPS, respectively. The estimated rate of salinity decreases and increases for the sample without EPS is 1.55 psu/cm and 0.87 psu/cm respectively, while the decreasing rate for the sample with EPS is 1.53 psu/cm.

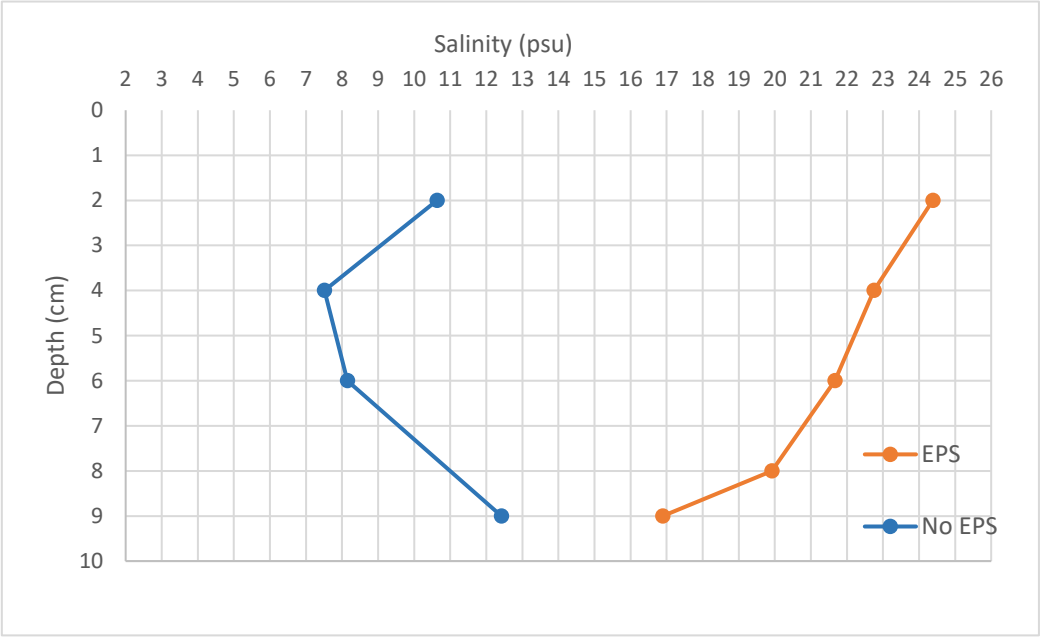


Figure 5-12 Salinity profiles for ice grown at -10°C from solutions of starting artificial ocean salinity of 30 psu with and without EPS.

This estimated rate of salinity decrease from Figure 5-12 shows that the rate of brine expulsion is similar for top part of both samples. The sample with EPS does not show an increasing profile at the bottom of the sample, thus, it can be assumed that most brine is retained in this sample.

5.3 Artificial sea ice textural analysis

5.3.1 Method of analysis

Artificial sea ice crystal structure and size were analysed through cross polarisation technique as outlined in Section 4.3.1. Crystal sizes were measured (as seen in Figure 5-13 A) using an image processing tool - imageJ. For each texture, at least 20 crystals were identified and measured. A table with individual crystal sizes was created by the imageJ interface and it was used to develop a table such as Table 5.6. Additionally, a graph like Figure 5-14, showing the mean crystal size for each texture was developed for each sample.

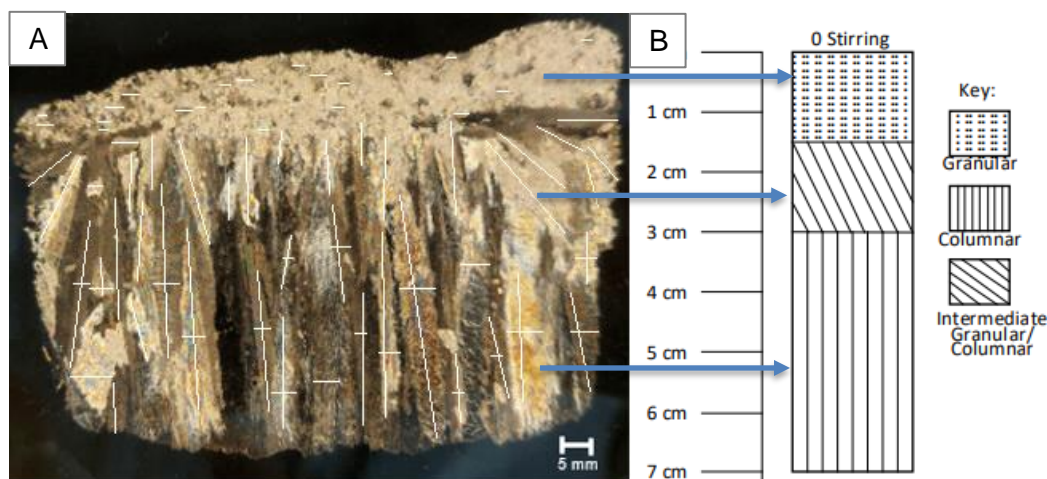


Figure 5-13 Cross polarisation results of ice grown at -20°C from a 10 psu solution showing the (A) process of crystal measurement and (B) the corresponding stratigraphy diagram.

Table 2.1 was used to determine the ice texture according to crystal sizes obtained from imageJ. An area with crystal sizes less than 10 mm was classified as granular zone. According to Table 2.1, an area with crystal size ranging between 10 mm to 100 mm is classified as intermediate between granular and columnar. The crystals in this zone are slightly elongated, indented and interlocked. In this work, however, it was observed that slightly elongated, indented, and interlocked crystals have mean sizes from 5 mm. Thus, the intermediate zone will be taken as a range between 5 mm to 100 mm. Lastly, an area with crystal sizes between

10 mm to/greater than 100 mm is termed the columnar zone due to crystals being elongated and having a column shape.

Weeks and Ackley (1982) list four different mechanisms that could explain the presence of frazil ice in cores. Firstly, freezing as a result of contact between the melt water from the ice surface and the water underneath the ice. Thus, forming a pool of two water bodies of different salinities and different freezing point. Secondly, adiabatic decompression which is primarily associated with platelet ice growth. This results in supercooling of water flowing under ice shelves. Thirdly, thermohaline convection associated with congelation ice growth in leads and polynyas. This results in surface cooling and freezing where brine released into underlying water creates frazil ice as the sinking water is subjected to supercooling by double diffusion process. Lastly, the wind and wave induced turbulence. This is the reason Jeffries *et al.* (1994) used to explain frazil ice observed directly below the snow ice of cores collected at the end of summer in the eastern Ross Sea and the Amundsen Sea. Thus, he suggested that frazil ice formation is the initial ice growth stage.

The first two mechanisms do not apply for artificial sea ice grown for this study since there was no melting during the experimental process. The columnar zone in metal ingots is defined as a zone with strong crystal elongation parallel to the direction of heat flow (Weeks and Ackley, 1982). These crystals grow during calm conditions and are characterised by pronounced orientation and increasing crystal size. The formation of columnar crystals is as a result of a geometric selection process where crystals with horizontal c-axes outgrow those with c-axes off the horizontal since ice grows faster in the basal plane.

The intermediate or transitional zone can be described as disordered columnar zone which results from congelation of supercooled water at the ice/water interface. It is associated with larger degree of interlocking between the crystals because grains displace and impinge on one another during growth. Eicken and Lange (1989) list the possible reasons for growth of crystals

in this zone as follows: (1) incorporation of frazil ice through nucleation of new grains, (2) enhanced growth rates due to increased intensity of cooling and (3) modification of ice-water interface due to highly dynamic ocean conditions such as wave actions.

Once different textures were identified from analysing imageJ results, a stratigraphy diagram was drawn for each sample as seen in Figure 5-13 B, showing the artificial sea ice textures as per their arrangement on the sample, as well as their corresponding lengths. For Sections 5.3.2 to 5.3.5, only the sample stratigraphy, the mean crystal size table and the corresponding graph will be shown with the corresponding cross polarisation images found in Appendix E.

Table 5.6 illustrates the percentage of each texture in the sample, the mean crystal size in the corresponding texture and the 95% confidence interval of the mean crystal size. For ice grown at -20°C from a 10 psu solution at a speed of 0 rpm for example, the granular texture made up 22.9% of the sample with crystals having a mean crystal size of 2.39 ± 0.74 mm. Of this mean crystal size, 95% of the true mean crystal size lie within this range: 2.04 mm and 2.73 mm. Additionally, this 22.9% granular section makes up the top 1.5 cm of the sample as can be seen in Figure 5-13 B.

Table 5.6 Fraction of the artificial sea ice texture and the corresponding crystal size for samples obtained at -20 °C from a solution of starting artificial ocean salinity of 10 psu for 0 rpm stirring.

Sample	Granular		Intermediate		Columnar	
	%	Crystal size (mm)	%	Crystal size (mm)	%	Crystal width (mm)
0 rpm	22.9	2.39 ± 0.74	21.4	12.47 ± 5.72	55.7	4.65 ± 1.80
95% Confidence	$2.04 \leq x \leq 2.73$		$9.79 \leq x \leq 15.1$		$3.81 \leq x \leq 5.50$	

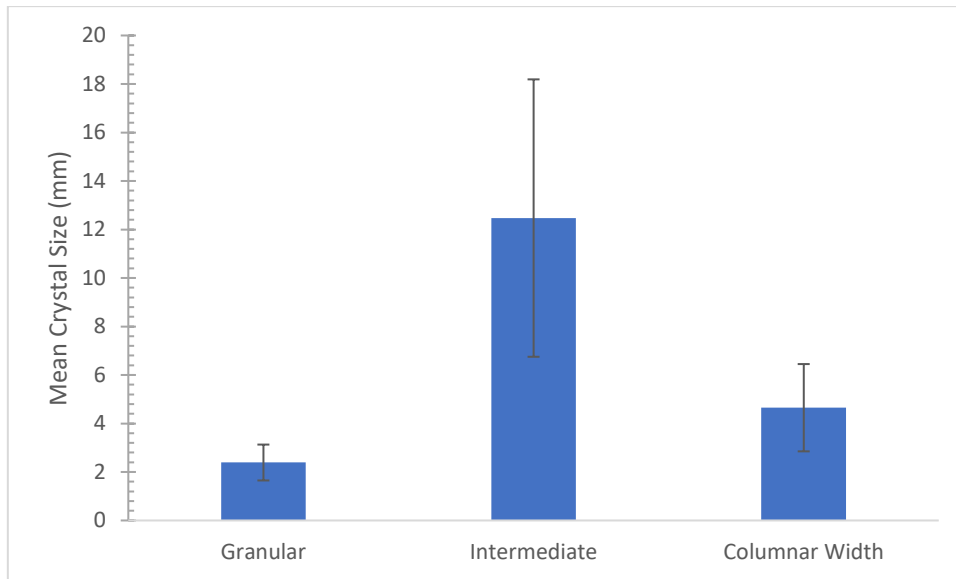


Figure 5-14 Graph illustrating ice textures and corresponding mean crystal sizes for ice grown at -20°C from a solution of starting artificial ocean salinity of 10 psu for 0 rpm stirring.

5.3.2 Effect of varying the starting artificial ocean salinity on artificial sea ice crystal structure

In the effort to understand the effect of starting artificial ocean salinity on artificial sea ice crystal structure, artificial sea ice was grown at varying starting artificial ocean salinity: 10 psu, 20 psu, and 30 psu, at the same ambient temperature of -10°C.

Following the sampling procedure as detailed in Appendix B and the cross polarisation technique in Section 4.3.1, the artificial sea ice crystal structure was analysed.

The samples grown at 10 psu and 20 psu exhibited the granular and columnar texture, while the 30 psu sample showed the granular, transitional, and columnar texture (Figure 5-15). Furthermore, the 30 psu sample revealed more intergranular spaces and larger grains compared to the 10 psu and 20 psu samples (Figure E. 1 in Appendix E).

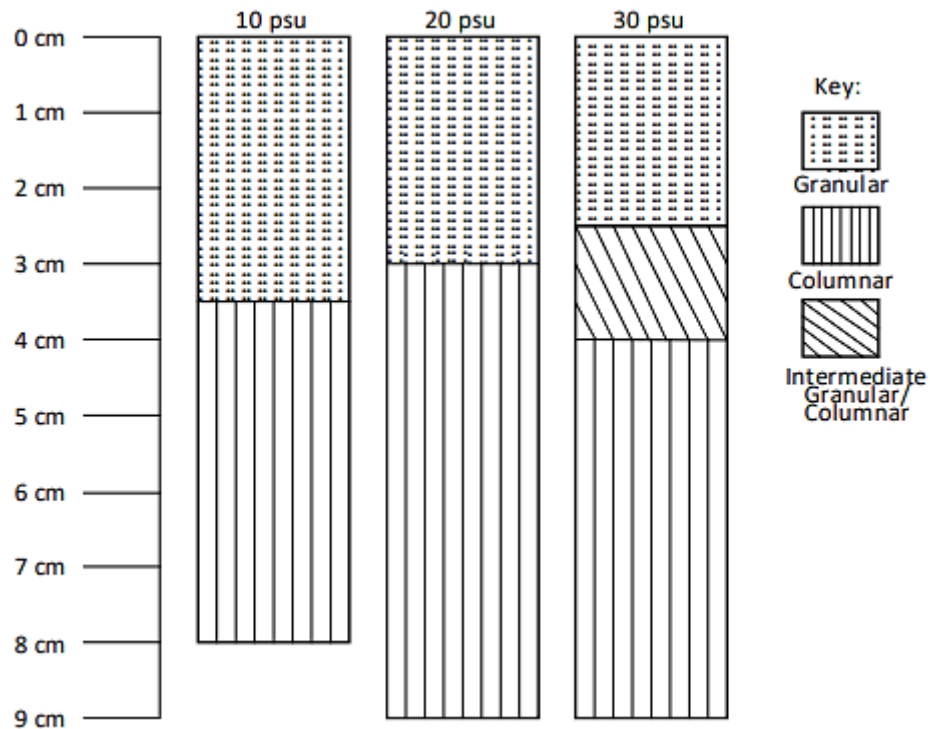


Figure 5-15 Stratigraphy diagrams for ice grown at -10°C from solutions of starting artificial ocean salinities of 10 psu, 20 psu and 30 psu.

The percentage of the granular (Figure 5-15, Table 5.7) is higher for the 10 psu sample and lower for the 30 psu sample. This observation is supported by the percentage of granular texture for all three samples in Table 5.7. The intermediate zone on the 30 psu reflects the zone where crystals were changing from granular to columnar texture. This decrease in the granular zone can be attributed to the fact that increasing salinity depresses the freezing point and decreases the artificial sea ice growth rate as seen in Table 5.2. A slower artificial sea ice growth rate allows for the formation of bigger crystals, thus, less brine inclusions (Weeks & Ackley, 1982). Therefore, this agrees with the observed decreasing percentage of granular zone from the 10 psu to 30 psu sample since this zone is characteristic of smaller crystals with more brine inclusions formed as a result of a faster growth rate (Table 5.2 in Section 5.2.2).

Figure 5-5 shows that the 30 psu sample had a lower cooling rate compared to the 10 psu and 20 psu, thus having a slower growth rate. However, the salinity profile of these samples as

seen in Figure 5-6, show the 30 psu sample retained the most brine. According to Weeks and Ackley (1982), the sample having a lower cooling rate has less brine retention, which is not the case here. This could be caused by the fact that the 30 psu sample did not have enough room for brine expulsion due to its higher starting artificial ocean salinity. In addition, all samples were grown at the same ambient temperature, with salinity being the varied variable. Hence, the effect of the kinetics due to varying the starting artificial ocean salinity were more dominant, thus the 30 psu sample retained more brine. Furthermore, the higher starting artificial ocean salinity sample resulted in a slowed growth rate. This allowed existing crystals to grow bigger and elongate, thus favouring the formation of columnar crystals as seen in Figure 5-15.

Table 5.7 and Figure 5-16 show that while the percentage of the granular texture decreased with increasing salinity, the columnar texture did not show a definite trend. First, it increased with increasing salinity from 10 psu to 20 psu, then decreased from 20 psu to 30 psu (Table 5.7). This decrease however, could be attributed to the presence of the intermediate texture on the 30 psu sample. Since the intermediate texture is referred to as the disordered columnar texture, it can be deduced that the columnar texture increased with increasing starting artificial ocean salinity.

Table 5.7 Fraction of the artificial sea ice texture and the corresponding crystal size for samples obtained at -10 °C from solutions of starting artificial ocean salinities of 10 psu, 20 psu and 30 psu.

Sample	Granular		Intermediate		Columnar	
	%	Crystal size (mm)	%	Crystal size (mm)	%	Crystal width (mm)
10 psu	43.8	3.03 ± 1.05			56.3	2.94 ± 0.83
20 psu	33.3	2.99 ± 0.97			66.6	3.01 ± 0.98
30 psu	27.8	2.14 ± 0.53	16.7	5.24 ± 1.41	55.5	6.74 ± 3.87
95% Confidence	2.32 ≤ x ≤ 3.12		4.23 ≤ x ≤ 6.25		3.62 ≤ x ≤ 5.25	

Overall, the average crystal size decreased in the granular zone and increased in the columnar zone. These crystals follow the trend of their respective textures. This can be explained by an assumption that the phasing out of granular texture forces the granular crystals to decrease in size. Additionally, the slower growth rate in the 30 psu solution favoured crystal growth, while in the 10 psu solution, nucleation was favoured (Section 2.2).

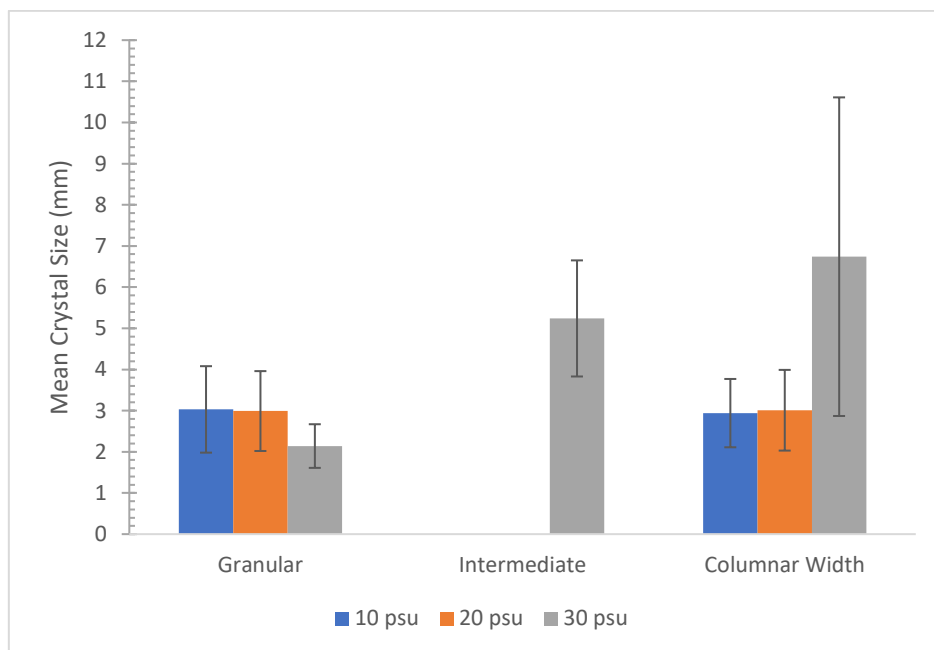


Figure 5-16 Graph illustrating ice textures and corresponding mean crystal sizes for ice grown at -10°C from solutions of starting artificial ocean salinities of 10 psu, 20 psu and 30 psu.

5.3.3 Effect of varying the ambient temperature on artificial sea ice crystal structure

To understand the effect of ambient temperature on the crystal structure of sea ice, artificial sea ice was grown at varying ambient temperatures: -20°C, -10°C, and -5°C, from solutions of the same starting artificial ocean salinity of 30 psu.

The sample grown at -20°C exhibit the granular texture from the top to the bottom of the sample, while the sample grown at -10°C and -5°C show the granular, transitional, and

columnar textures as seen in Figure 5-17. The red dashed-line show sea ice thickness at the end of 16 hours of growth. The comparison of the crystal structure over 16 hours of growth was done so that the changes due to varying temperature can be compared over a fixed growth period. Although the -20°C and -10°C samples grew to the same thickness, this was over 16 hours and 42 hours respectively. It was desired to grow the -5°C sample to 9 cm as well, however, growth in this reactor stopped at a thickness of 5 cm even with prolonged freezing. Thus, 16 hours is a controlled variable for comparison across all samples.

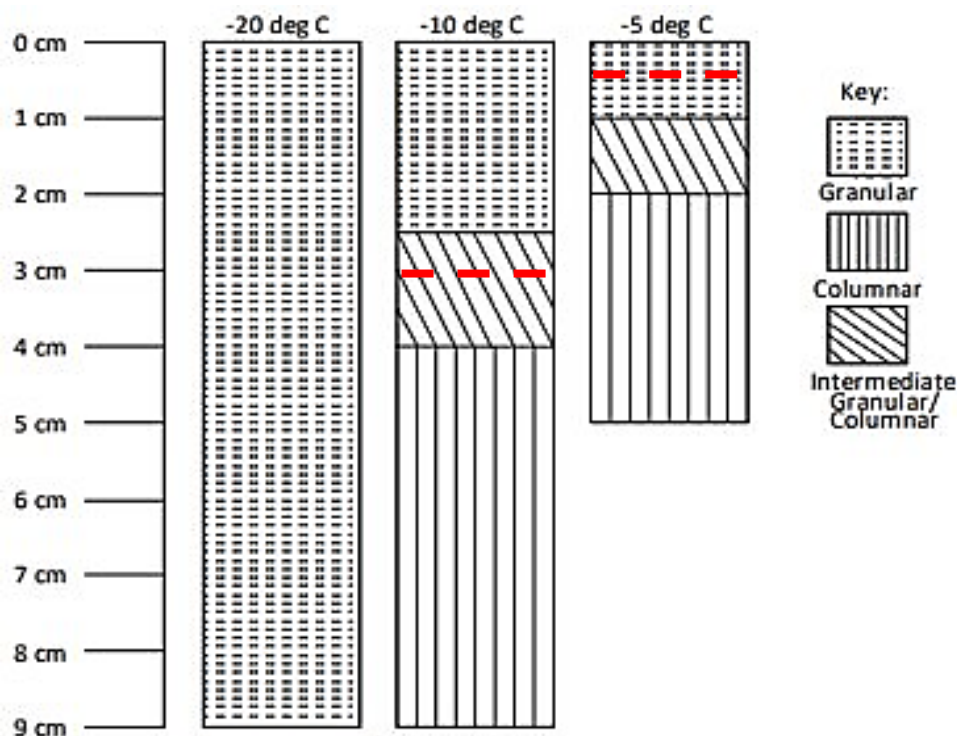


Figure 5-17 Stratigraphy diagrams for ice grown from solutions of starting artificial ocean salinity of 30 psu at -20°C , -10°C and -5°C (thickness of ice at the end of 16 hours shown by red dashed-line)

The percentage of the granular texture decreased with increasing temperature. The columnar texture, as explained in Section 5.3.2, can be assumed to have increased with increasing temperature. It should be noted that an assumption is made that with increased growth time, the sample grown at -5°C would have grown thicker and would have exhibited the columnar texture from 2 cm, all the way down through its length.

At lower ambient temperatures, i.e, higher cooling rate, the time taken to freeze was shorter, the rate of change in temperature was higher per given depth in ice, and the growth rate was higher, as seen in Table 5.2. It also follows from Figure 5-5 that at the end of 16 hours of the experiment, the sample grown at -20°C experienced a higher cooling rate compared to samples grown at -10°C and -5°C . Therefore, the granular texture observed for the sample grown at -20°C (Figure 5-17) is due to the lower cooling rate as suggested by Weeks and Ackley (1982). Thus, the crystals in this sample had an advantage of nucleating to form many more new crystals than the growth and elongation of the crystals already formed. Thus, this sample had many brine inclusions between its smaller crystals, while the samples grown at -10°C and -5°C had bigger, vertically elongated columnar crystals with fewer brine inclusions. The assumption about the presence of many brine inclusions is supported by Figure 5-8, the salinity profiles of all three samples, and is further discussed in Section 5.4.3.

Gow and Tucker (1991) stated that analyses of crystalline structure of the Arctic ice floes have shown ice textures predominantly of columnar origin with small amounts of granular in the upper parts of ice. While, most research on the crystal structure of the Antarctic Sea ice shows the multiple layering of frazil ice, especially during winter (Jeffries *et al.*, 1994). The difference in the crystal structure is attributed to the geographics. The Arctic Ocean is surrounded by land, while the Antarctic continent is surrounded by an open ocean. Thus, sea ice grows under calm conditions in the Arctic, and turbulent conditions due to winds and waves in the Antarctic (Gow and Tucker, 1991; Jeffries *et al.*, 1994). Therefore, in this case, it is seen from Figure 5-17 that the samples grown at -10°C and -5°C revealed columnar crystals associated with growth under calmer conditions. In contrast, the sample grown at -20°C only revealed a granular texture. In this project, turbulent conditions, or rather, less calm conditions could be attributed to dynamic thermohaline convection due to growth at a higher cooling rate and higher starting artificial ocean salinity.

It is seen from Table 5.8 that the granular texture percentage decreased with increasing ambient temperature, and the intermediate and columnar textures increased with increasing ambient temperature. This trend is in support of the fact that increasing ambient temperature favours the growth and dominance of columnar crystals.

Table 5.8 Fraction of each ice texture and corresponding crystal size for samples obtained from ice grown from solutions of starting artificial ocean salinity of 30 psu at -20°C, -10°C and -5°C.

Sample	Granular		Intermediate		Columnar	
	%	Crystal size (mm)	%	Crystal size (mm)	%	Crystal width (mm)
-20 °C	100	2.65 ± 0.50	-	-	-	-
-10 °C	27.8	2.14 ± 0.53	16.7	10.04 ± 2.51	55.5	4.34 ± 1.54
-5 °C	20.0	1.93 ± 0.49	20.0	6.67 ± 2.82	60.0	4.02 ± 1.33
95% Confidence	2.00 ≤ x ≤ 2.47		6.79 ≤ x ≤ 9.91		3.51 ≤ x ≤ 4.86	

Figure 5-18 shows that the average crystal size decreased with increasing ambient temperature for the granular, intermediate and columnar textures. This is opposite to what was expected as it was established that increasing ambient temperature favours crystal growth (Section 2.7.1). It is assumed that this is because the crystals in the sample grown at -5°C did not have enough time to grow after nucleation since the sample thickness was 0.5 cm after 16 hours. Subsequently, since the growth rate could not be estimated, this assumption cannot be validated.

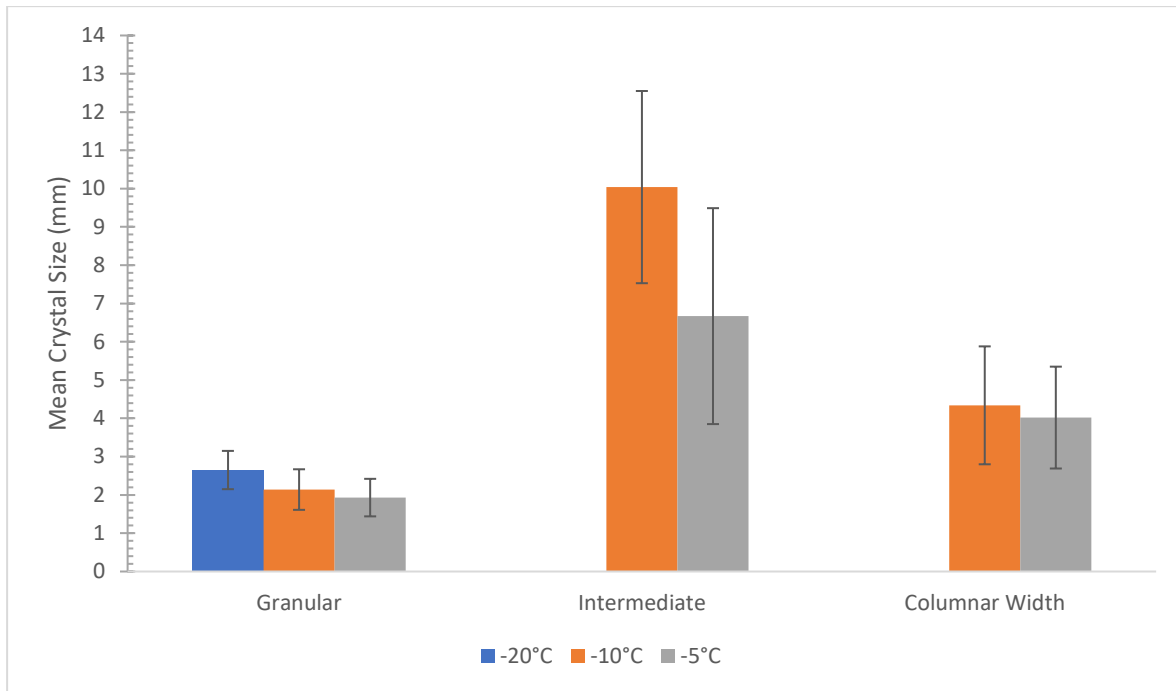


Figure 5-18 Graph illustrating ice textures and corresponding mean crystal sizes for ice grown from solutions of starting artificial ocean salinity of 30 psu at -20°C, -10°C and -5°C

5.3.4 Effect of varying the reactor volume on artificial sea ice crystal structure

The effect of reactor volume on artificial sea ice structure was studied through artificial sea ice growth at an ambient temperature of -20°C and a starting artificial ocean salinity of 30 psu from reactors of varying volume: 3 L and 30 L. Artificial sea ice was grown to a height approximately half of the initial solution height in both reactors (10 cm for 3 L, and 18 cm for 30 L).

Figure 5-19 shows that ice grown from a 3 L reactor has a granular texture throughout the sample, while ice grown from a 30 L reactor shows a smaller fraction of granular at the top, then columnar texture throughout. The upper part of the red line on the stratigraphy diagram of the 30 L sample is the thickness which will be compared to the whole thickness of the 3 L sample of Figure 5-19. Hence, comparison of texture for varying reactor volume is done over a constant growth period of 16 hours for both samples.

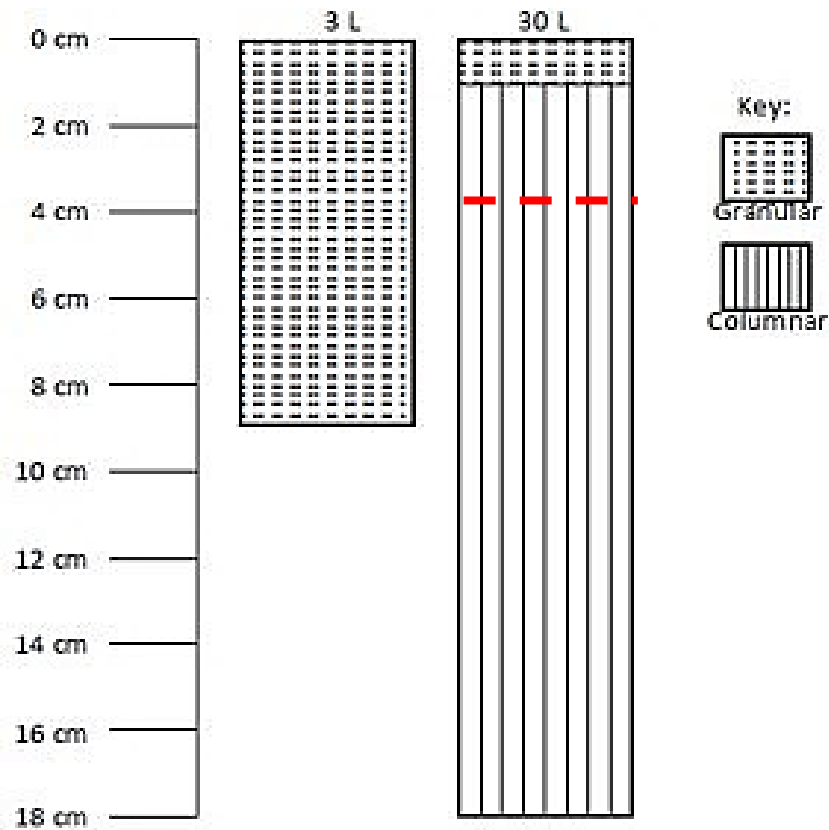


Figure 5-19 Stratigraphy diagram of ice grown at -20°C from solutions of starting artificial ocean salinity of 30 psu from a 3 L and 30 L reactor (with the red line showing the thickness of the 30 L sample after 16 hours).

Since the 3 L reactor sample experienced a higher cooling rate due to having a higher surface-to-volume ratio (Mukaromah *et al.*, 2016), crystals did not have sufficient time to grow. The 30 L reactor sample had enough time for the growth of geometrically preferred, bigger and elongated crystals in the columnar zone. This is because the 30 L reactor is big enough to allow for crystal growth in the preferred shape and dimension.

It is also evident from the growth dynamics, temperature and salinity profiles of these two samples as seen in Table 5.4, Figure 5-9 and Figure 5-10, that the growth rate was higher for the sample grown from the 3 L reactor. Thus, more brine was retained in this sample since it had more brine inclusions within its smaller granular crystals.

The percentage of the granular texture decreased with increasing reactor volume. In addition, the mean crystal size decreased with increasing reactor size as seen in Table 5.9 and Figure 5-20. There is no columnar zone in the sample grown from the 3 L reactor, hence there is only one bar in Figure 5-20 for the columnar width.

Table 5.9 Fraction of each ice texture and corresponding crystal size for samples grown from a 3 L and 30 L reactor at -20°C from starting artificial ocean salinity of 30 psu.

Sample	Granular		Intermediate		Columnar	
	%	Crystal size (mm)	%	Crystal size (mm)	%	Crystal width (mm)
3 L	100	2.65 ± 0.5	-	-	-	-
30 L	5.9	2.40 ± 0.56	-	-	94.1	5.39 ± 0.83
95% Confidence	2.51 ≤ x ≤ 2.27		-		4.82 ≤ x ≤ 5.77	

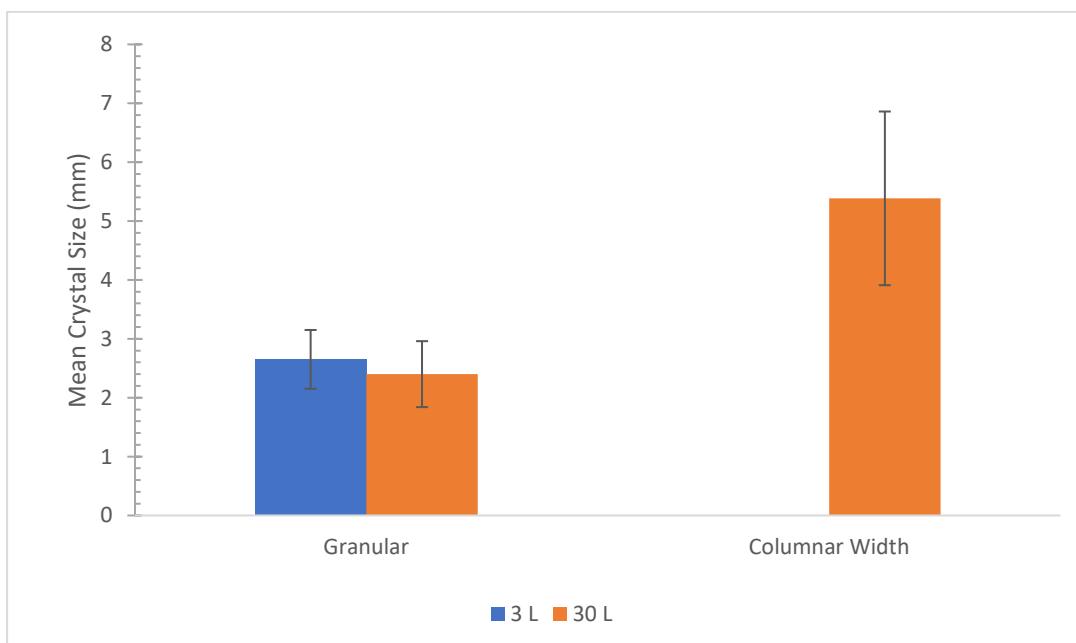


Figure 5-20 Graph illustrating ice textures and corresponding mean crystal sizes for ice grown at -20°C and starting artificial ocean salinity of 30 psu from a 3 L and 30 L reactor.

5.3.5 Effect of the presence of EPS addition on artificial sea ice crystal structure

The effect of the presence of EPS on artificial sea ice crystal structure was studied by growing artificial sea ice at an ambient temperature of -10°C and a starting artificial ocean salinity of 30 psu, from solutions with and without the addition of EPS.

During analysis, the granular and columnar textures were clearly distinguished from the two samples, with both samples having similar granular texture percentage as seen in Figure 5-21.

The sample without EPS shows 1.5 cm of a transitional texture between the granular and the columnar textures. In the sample with EPS however, the crystals look poorly ordered with many tiny features that are not well-defined. These could either be grains or pores as seen in Figure E. 4 in Appendix E. These could have superimposed the crystals in the transitional zone. Hence, it cannot be concluded that the area of intermediate crystals is not present.

Krembs *et al.* (2011) also made similar observations in their study of artificial sea ice grown at -10°C with the addition of fresh *Melosira* EPS. Fine-grained congelation ice with mostly intergranular brine inclusions was observed (Figure 2-8). This ice had irregular convoluted shape crystals and a poorly ordered arrangement, closely resembling natural sea ice.

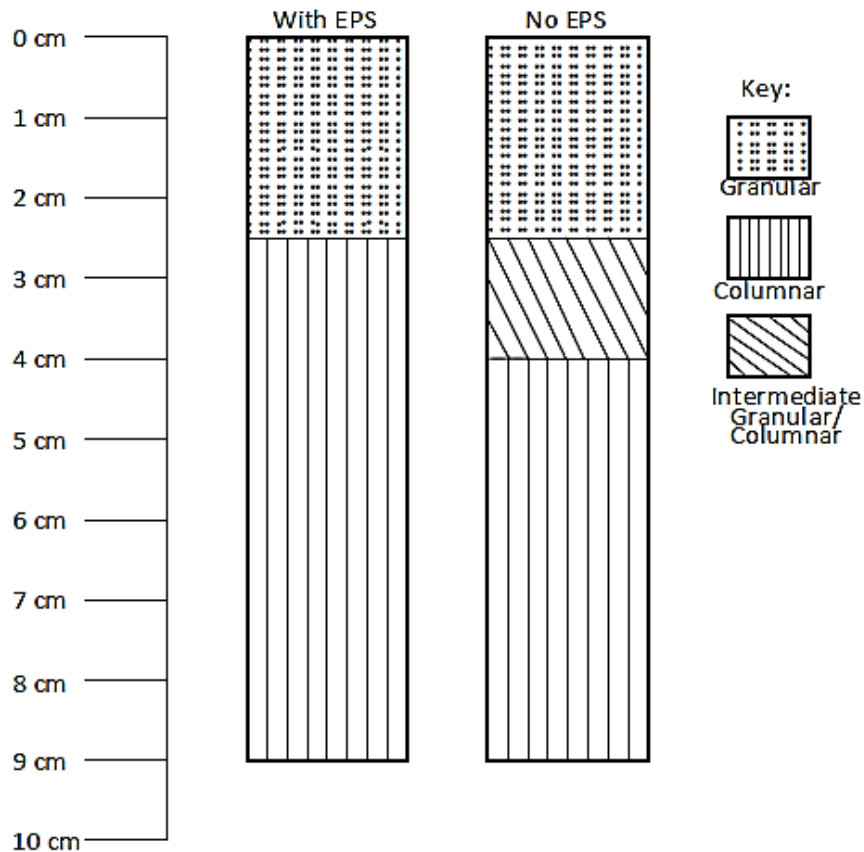


Figure 5-21 Stratigraphy diagrams for ice grown from solutions of starting artificial ocean salinity of 30 psu at -10°C with and without EPS.

Crystals in the sample without EPS are well defined with different textures clearly visible. The column-shaped crystals can be clearly distinguished from each other and from the air or brine inclusions (black spots in Figure E. 3 A in Appendix E). In contrast, the sample with EPS shows small rounded and oval shaped crystals in the granular zone. Some of these uncharacterized rounded grains are shown at the bottom of the sample. Crystals in the columnar zone are not clearly distinguished from each other, they are blurred and blotchy (see Figure E. 3 B in Appendix E).

The addition of EPS depressed the freezing temperature and slightly increased the rate of change in temperature per given ice depth (as seen in Table 5.5 and Figure 5-11). This qualifies an assumption that the presence of EPS increases the crystal sizes since it also retained more brine as seen in Figure 5-12.

It can be seen in Table 5.10 and Figure 5-22 that the percentage of the granular texture did not change with the addition of EPS. However, the percentage of the columnar texture increased since the presence of the intermediate zone in the sample without EPS reduced the columnar zone fraction. This agrees with trends observed in Section 5.3.2 to 5.3.4, showing that the sample at the lowest cooling rate results in the average growth of columnar crystals.

Table 5.10 Fraction of each ice texture and corresponding crystal size for samples obtained at -10 °C from solutions of starting artificial ocean salinity of 30 psu with and without EPS.

Sample	Granular		Intermediate		Columnar	
	%	Crystal size (mm)	%	Crystal size (mm)	%	Crystal width (mm)
No EPS	27.8	2.14 ± 0.53	16.7	5.24 ± 1.41	55.5	6.74 ± 3.87
EPS	27.8	2.46 ± 0.65	-	-	72.2	4.11 ± 1.33
95% Confidence	2.02 ≤ x ≤ 2.56		4.23 ≤ x ≤ 6.25		4.21 ≤ x ≤ 6.64	

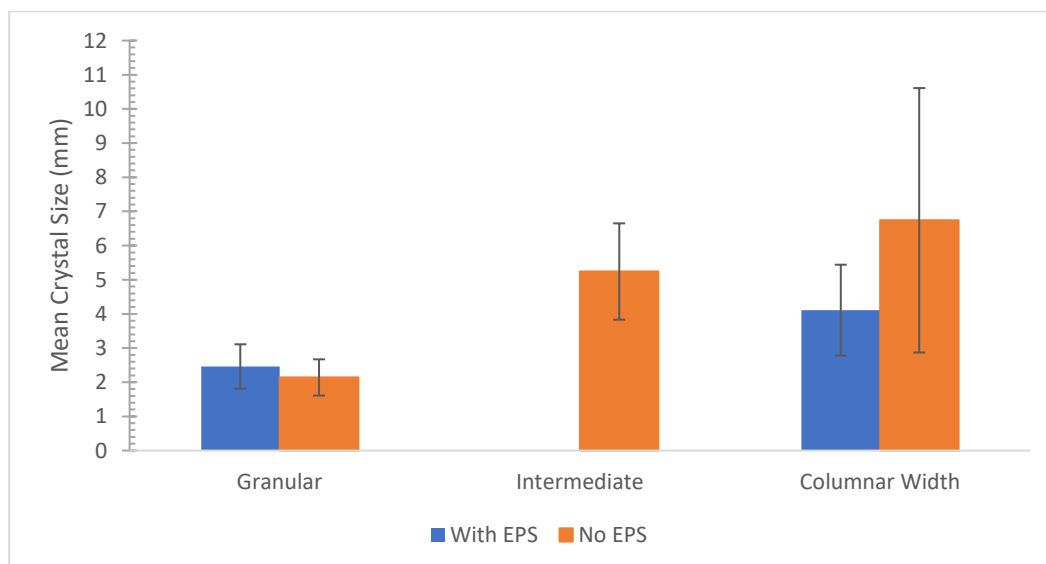


Figure 5-22 Graph illustrating ice textures and corresponding mean crystal sizes ice grown at -10°C from a solution of starting artificial ocean salinity of 30 psu with and without EPS.

5.4 Artificial sea ice brine analysis

5.4.1 Method of analysis

Artificial sea ice samples were scanned using the micro-CT technique as outlined in Section 4.3.2 to analyse the brine, air and ice phases. The results are both qualitative and quantitative, and allow for 2D and 3D visualisation of each sample as shown in Figure 5-23 A&C and Figure 5-23 B&D, respectively. In Figure 5-23 A&B, the white shaded area represent brine, the black area represents the air/voids, and the grey area represents the ice. Brine and air channel size can each be visualised through colour coding as the example in Figure 5-23 C and D, only showing the brine channels since the viewer allows for visualisation of either brine or air inclusions at a time. Figure 5-23 C&D show brine volume, where the red colour are channels with volumes greater than 1812 mm³ and the blue colour show those less than 453 mm³.

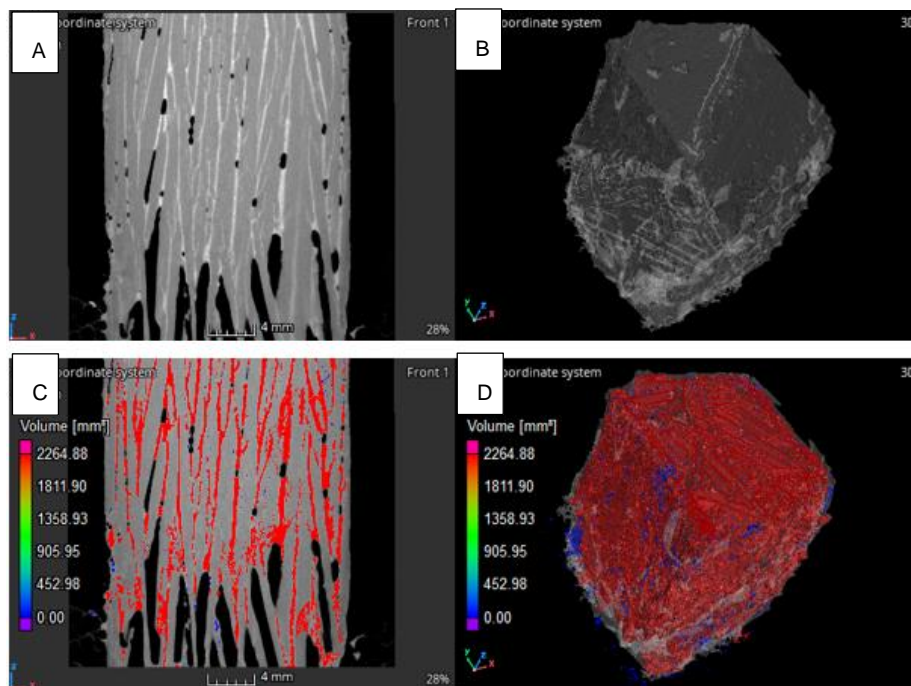


Figure 5-23 Visual result showing the process of brine and air pockets analysis from CT-scanning for ice grown at -10°C from a 30 psu solution with (A) and (B) showing the brine, air and ice in white, black and grey respectively, and (C) and (D) showing brine volume through colour coding.

The CT-scan visuals were all obtained at a scanning temperature of -10°C . The artificial sea ice samples grown at -10°C from a starting artificial ocean salinity of 10 psu are shown in Figure 5-24. The grey shaded area on the visuals represents the ice, while the white and black represent the brine and voids respectively. The colour-coded visuals showing the brine and air pocket volume distribution on the sample can be seen in Appendix F.

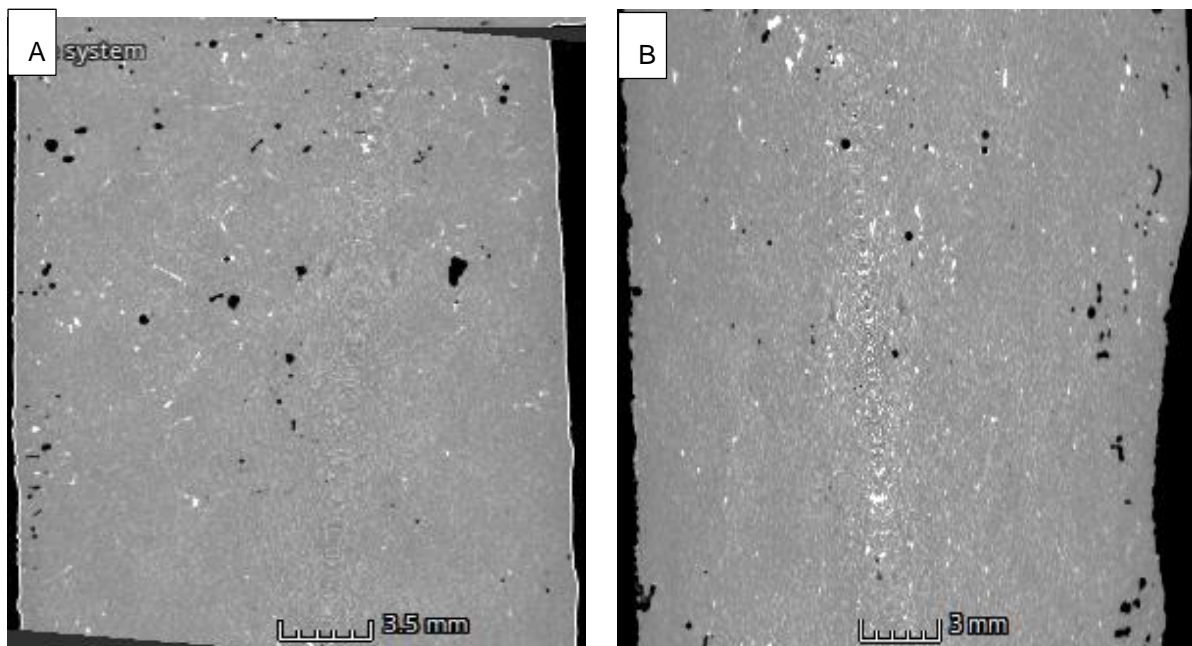


Figure 5-24 Micro-CT scan visuals for the (A) top and (B) bottom section of ice grown at -10°C from a solution of 10 psu starting artificial ocean salinity.

To describe the shape of each phase, parameters such as the diameter, surface area, volume, and sphericity are provided by the micro-CT scan interface for individual brine and air inclusions. The average diameter, surface area, and sphericity of brine and air inclusions were computed and reported as information relating to inclusion size (Table 5.11), while the sum of the volumes of individual inclusions was calculated and reported as porosity of the sample.

The average brine diameter and surface area increases from the top to the bottom of the sample as seen in Table 5.11. The sphericity of the inclusions however decreases from the

top to the bottom. This implies that the shape of brine inclusions at the top is closer to spherical, but at the bottom, the inclusions assume irregular shapes. A similar trend is observed for the air inclusion, however, the magnitude of increase for each parameter is more for brine inclusions than for the air inclusions.

Table 5.11 Size description of brine and air inclusions for the top part of ice grown at -10°C from a solution of starting artificial ocean salinity of 10 psu.

	Brine		Air	
	Top	Bottom	Top	Bottom
Diameter (mm)	0.77	0.81	0.53	0.65
Surface Area (mm)	1.11	1.08	0.65	1.01
Sphericity	0.33	0.28	0.60	0.56

The porosity of each sample was determined by the sum of the total volume of brine and air inclusions. For example, the total volume of brine was calculated by adding the volume of brine from all brine inclusions in the sample. The same was done for the air inclusions. The sum of the two volumes was then reported as the porosity of the sample due to brine and air inclusions. Figure 5-25 shows the porosity of ice grown at -10°C from a 10 psu solution.

It can be seen from Figure 5-25 that the artificial sea ice porosity increases from the top to the bottom of the sample, with brine being the main contributing factor to porosity. This corresponds to the results in Table 5.11, showing smaller inclusions at the top and bigger ones at the bottom, subsequently showing a higher overall ice porosity at the bottom of the sample compared to the top (Figure 5-25).

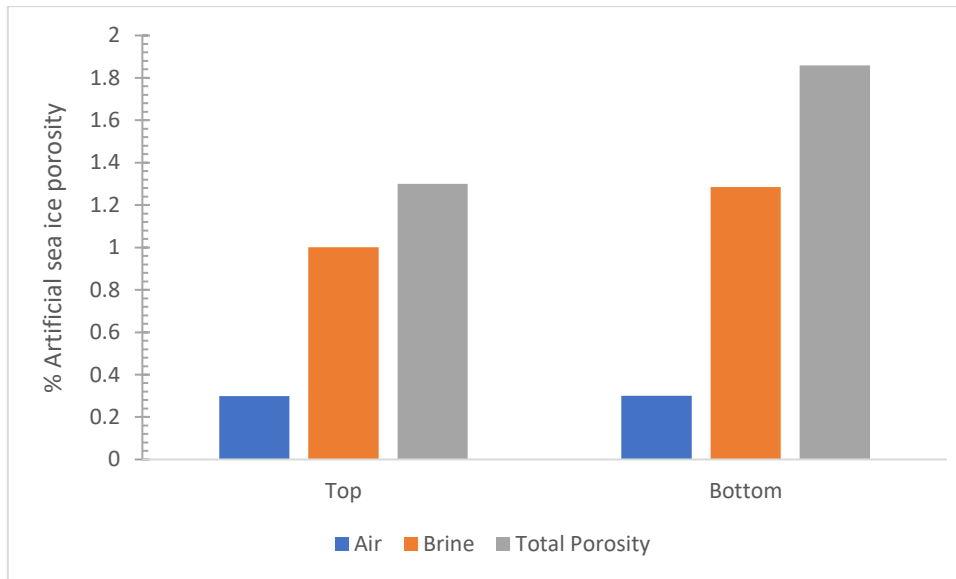


Figure 5-25. Artificial sea ice porosity of ice grown at -10°C from a solution of starting artificial ocean salinity of 10 psu.

5.4.2 Effect of varying the starting artificial ocean salinity on artificial sea ice porosity

The effect of varying the starting artificial ocean salinity on the porosity of artificial sea ice was studied by analysing the micro-CT scan visuals. Furthermore, the corresponding brine and air inclusion data of artificial sea ice grown at -10°C from varying starting artificial ocean salinity of 10 psu, 20 psu, and 30 psu was also analysed.

Increasing the starting artificial ocean salinity increases the size of brine and air inclusions within the artificial sea ice sample. At higher starting artificial ocean salinity, the freezing point is depressed, and freezing is delayed. Thus, the cooling rate of a sample growing from a solution of higher starting artificial ocean salinity is lower at any given point compared to that of ice grown at a lower starting artificial ocean salinity (Figure 5-5). Therefore, ice grown at higher starting artificial ocean salinity has a lower growth rate (Table 5.2). Hence larger brine inclusions are observed compared to the samples grown at lower starting artificial ocean salinity (Figure 5-16 and Figure 5-6). The brine and air inclusions of each sample were

analysed from the micro-CT scan visuals seen in Figure 5-26, where brine volume distribution can be seen in Figure F. 1 in Appendix F.

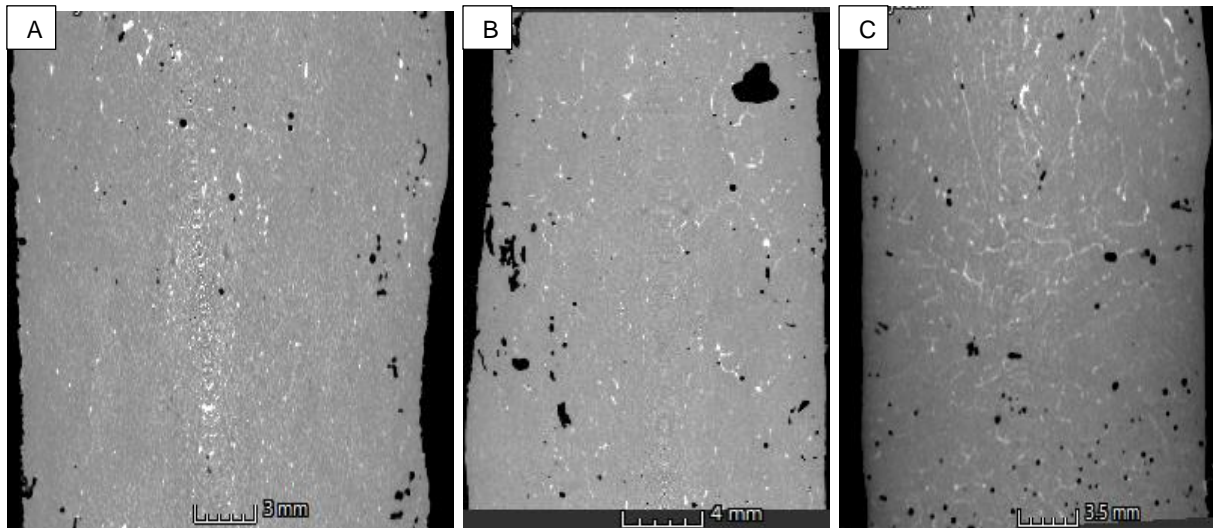


Figure 5-26 Micro-CT scan visuals for the top part of ice grown at -10°C from solutions of starting artificial ocean salinities of (A) 10 psu, (B) 20 psu, and (C) 30 psu.

It can be seen from Figure 5-26 that the brine inclusions in the sample grown at 10 psu and 20 psu were smaller and round, with a few air pockets compared to the samples grown at 30 psu. Although all samples show more brine at the top, the 30 psu sample show very small and less brine inclusions at the bottom, as well as more air inclusions. Additionally, it was noted that the air pockets in the sample grown at 20 psu were larger than the ones in the sample grown at 10 psu and 30 psu. The sample might have possibly melted during scanning. This would result in bigger air inclusions as the sample would have experienced drainage, similar to the observation made by Eicken *et al.* (2000) and Lieb lappen (2016) in their thermal evolution of sea ice experiments. Lieb Lappen (2016) further mentions that the air pockets on multi-year ice are significantly more than those in the first-year ice, and likely to be drained brine channels as they were plate-like shaped.

It was expected that inclusions in the sample grown at 10 psu and 20 psu be smaller (than the 30 psu) and comparable in size since they had similar growth dynamics (Table 5.2). This assumption follows from the fact that growth rate of the 10 psu and 20 psu ice was greater than that of the 30 psu ice. The 30 psu solution only started freezing once the whole solution body was cooled and convective, while that of the 10 psu and 20 psu solution was stratified since temperature of maximum density was higher than the freezing temperature at any point. Thus, the high-density saline water at the bottom of the 10 psu and 20 psu ice restricted brine expulsion once the critical ice thickness was reached (Toth and Lerman, 1975), hence, there are fewer air pockets in these samples.

The structural analysis of brine and air inclusions was performed for all three samples and the results are seen in Table 5.12.

Table 5.12 Size description of brine and air inclusions for the top part of ice grown at -10°C from solutions of starting artificial ocean salinities of 10 psu, 20 psu, and 30 psu.

	Brine			Air		
	Top					
	10 psu	20 psu	30 psu	10 psu	20 psu	30 psu
Diameter (mm)	0.67	0.67	0.72	0.53	0.55	0.65
Surface Area (mm)	1.01	0.77	3.40	0.65	1.05	0.88
Sphericity	0.44	0.42	0.44	0.60	0.61	0.55
	Bottom					
Diameter (mm)	0.81	0.82	0.68	0.65	0.94	0.85
Surface Area (mm)	1.08	1.10	1.48	0.29	1.84	2.62
Sphericity	0.51	0.40	0.50	0.56	0.51	0.50

Increasing the starting artificial sea ice salinity increases the average diameter and surface area of inclusions as seen in Table 5.12. Additionally, the inclusions are more spherical in shape at lower starting artificial ocean salinity. This is because the higher cooling rate experienced, by virtue of lower salinity, does not form elongated inclusions as growth is rapid. The similar trend is observed for both the top and bottom sections of the samples (Wettlaufer, 1977).

The effect of the starting artificial ocean salinity on the porosity of artificial sea ice is shown in Figure 5-27.

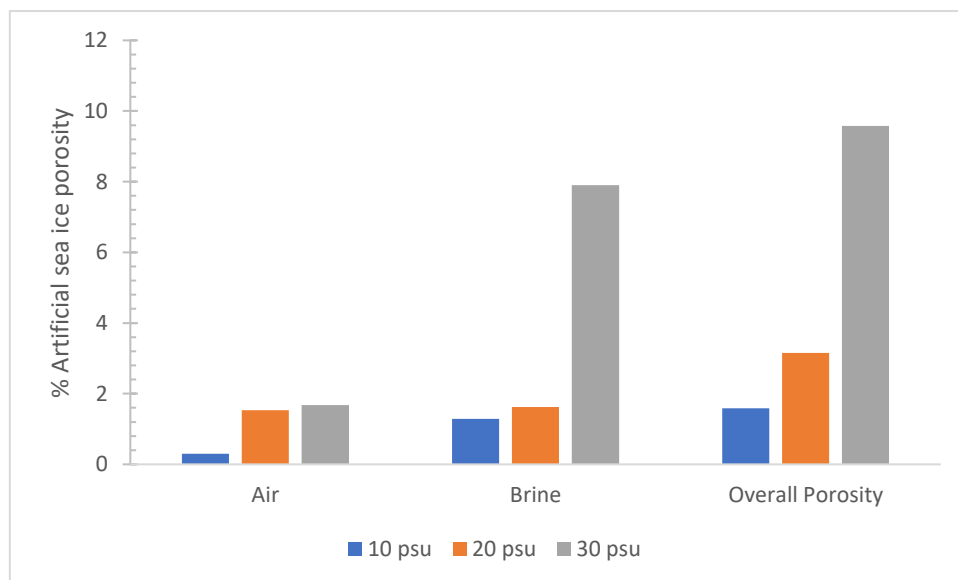


Figure 5-27. Porosity of artificial sea ice grown at -10°C from solutions of starting artificial ocean salinities of 10 psu, 20 psu, and 30 psu.

Increasing the starting artificial ocean salinity increases the size of brine and air inclusions (Table 5.12), however, the number density of inclusions remains small compared to those of ice grown from a lower starting salinity solution. As a result, the sample grown from a solution of lower starting artificial ocean salinity should be more porous. The percentage of ice porosity due brine increases from 1.3% at 10 psu, 1.6% at 20 psu, and 7.9% at 30 psu. Subsequently,

the percentage of ice porosity due to air pockets show an increase from 0.3% at 10 psu to 1.5% at 20 psu, and 1.7% at 30 psu. Although the air inclusion volume for the 20 psu sample is less than that of the 30 psu, it is still larger than expected considering the growth dynamics. Overall, the artificial sea ice porosity increased with increasing starting artificial ocean salinity.

5.4.3 Effect of varying the ambient temperature on porosity

The effect of ambient temperature on the porosity of artificial sea ice was studied by analysing the micro-CT scan visuals, and the corresponding brine and air inclusion data of ice grown from a solution of starting artificial ocean salinity of 30 psu at varying ambient temperatures of: -20°C, -10°C, and -5°C.

At a higher ambient temperature, the freezing process was delayed. Thus, the sample experienced a lower cooling rate during growth at any given point as seen in (Figure 5-7). Therefore, ice grown at a higher ambient temperature had a lower growth rate (Table 5.3), and crystals formed were bigger and columnar shaped with less brine inclusions.

In contrast, the crystals formed at a lower ambient temperature were smaller grains with a lot of smaller brine inclusions since the cooling rate was too high to favour the growth of bigger crystals. As a result, less brine inclusions are expected as the ambient temperature increases since the big crystal size does not allow room for many inclusions (Weeks and Ackley, 1982).

Figure 5-28 shows the micro-CT scan visuals of artificial sea ice grown from a solution of starting artificial ocean salinity of 30 psu at -20°C, -10°C, and -5°C with brine volume distribution shown in Figure F. 3.

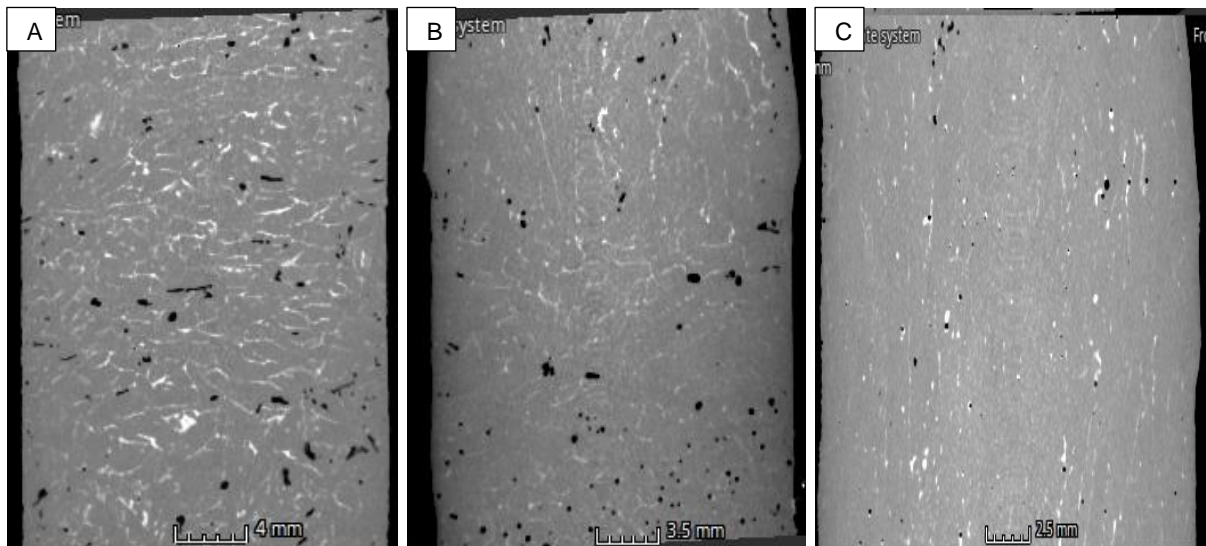


Figure 5-28 Micro-CT scan visuals for the top part of ice grown from solutions of starting artificial ocean salinity of 30 psu at (A) -20°C , (B) -10°C , and (C) -5°C .

It can be seen from Figure 5-28 that the brine content in the sample grown at -20°C is higher than that of the samples grown at -10°C and at -5°C . This is displayed by the presence of more white shaded areas, indicative of high brine volume. The brine inclusions in the -20°C appear to be horizontal in shape with more air pockets, while, in the -5°C , the brine inclusions were elongated, with less air pockets. This observation is supported by the findings of Eicken *et al.* (2000), which suggests that at higher ambient temperatures the mean inclusion size and elongation increase while number density decrease as inclusions merge.

The scale on Figure 5-28 A is larger (4 mm) than that of Figure 5-28 B and C, hence the inclusions seem bigger at first glance. The structural analysis of brine and air inclusions for all three samples is shown in Table 5.13, where inclusion' sizes can be seen.

Table 5.13 Size description of brine and air inclusions for the top part of ice grown from solutions of starting artificial ocean salinity of 30 psu at -20°C, -10°C, and -5°C.

	Brine			Air		
	Top					
	-20°C	-10°C	-5°C	-20°C	-10°C	-5°C
Diameter (mm)	0.58	0.72	0.78	0.91	0.65	0.59
Surface Area (mm)	13.87	3.40	0.88	1.85	0.88	0.83
Sphericity	0.48	0.44	0.44	0.61	0.55	0.53
	Bottom					
Diameter (mm)	0.64	0.68		0.85	0.85	
Surface Area (mm)	2.35	1.48		1.71	2.62	
Sphericity	0.52	0.50		0.56	0.50	

Increasing the ambient temperature increased the average diameter and decreased the surface area of inclusions as seen from the samples grown in Table 5.13. The increasing average size of inclusions with increasing ambient temperature in this case did not increase the overall brine content as it was the case in the findings of Eicken *et al.* (2000). This could be attributed to the number density of brine inclusions which is presumed to be high enough in the sample grown -20°C to increase the total brine content. It is assumed that the increased growth period and thus, ice thickness for the sample grown at -5°C, would have better reflected the effect of the growth dynamics on this sample. Hence, the structural analysis of the bottom section of the -5°C sample, and its brine volume would have improved conclusions put forward with regards to the effect of ambient temperature on inclusion structure and ice porosity. Additionally, Table 5.13 shows that the sphericity of brine inclusions decreased with increasing ambient temperature. This is expected as the inclusions in the sample grown at higher ambient temperature (-5°C) show elongation, moving away from the spherical shape.

Overall, increasing the ambient temperature decreased the brine and air volume. Thus, decreasing the ice porosity as seen in Figure 5-29. Increasing the ambient temperature decreased the number density and increased the size of inclusions (Eicken *et al.* 2000). As a result, the structure of the sample grown at a higher ambient temperature had a lower overall ice porosity as seen in Figure 5-29. The percentage of ice porosity due to brine decreased from 8.6% at -20°C to 7.9% at -10°C, and 1.4% at -5°C. Similarly, the percentage of ice porosity due to air also decrease from 1.6% at -20°C and -10°C, to 0.2% at -5°C.

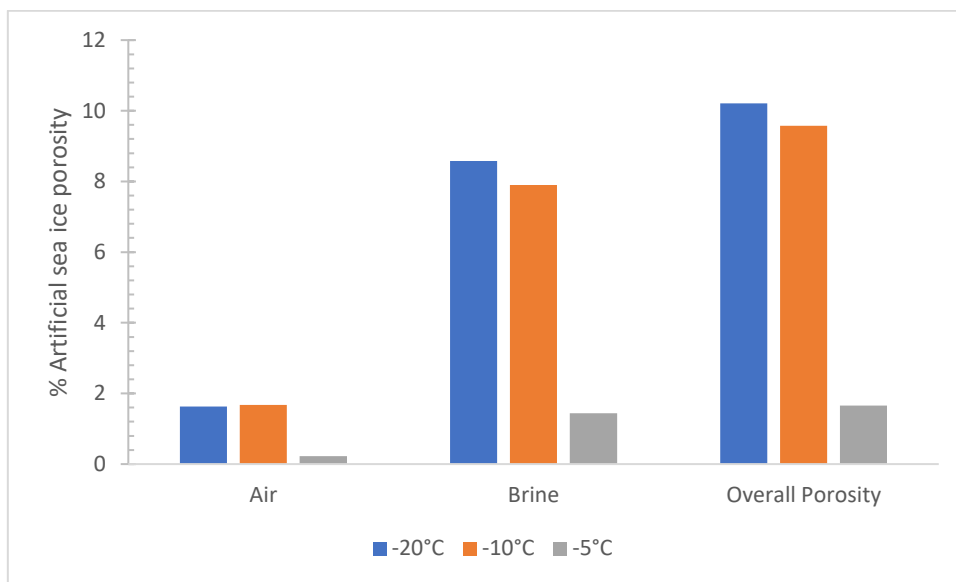


Figure 5-29. Porosity of artificial sea ice grown from solutions of starting artificial ocean salinity of 30 psu at -20°C, -10°C, and -5°C.

5.4.4 Effect of the presence of EPS addition on porosity

The effect of the presence of EPS on the porosity of artificial sea ice was studied by analysing the micro-ct scan visuals, and the corresponding brine and air inclusion data of ice grown from a solution of starting artificial ocean salinity of 30 psu at an ambient temperature of -10°C. EPS was added in one reactor and omitted in another.

It can be seen from Figure 5-30 that brine inclusions were much bigger, interconnected, and vertically elongated for the sample with EPS. The white colour on these visuals show the high brine volume with its colour distribution shown in Figure F. 5. The sample without EPS show both comparable amounts of the white and black inclusions, with the total brine volume (top and bottom sections) approximated at 3289 mm³. In contrast, the sample with EPS show white inclusions with the total brine volume approximated at 4199 mm³, 1.3 times greater than that without EPS. This difference in brine volume is attributed to the fact that EPS has its own salt concentration contributing to overall increase in the starting solution salinity (Krembs *et al.*, 2011).

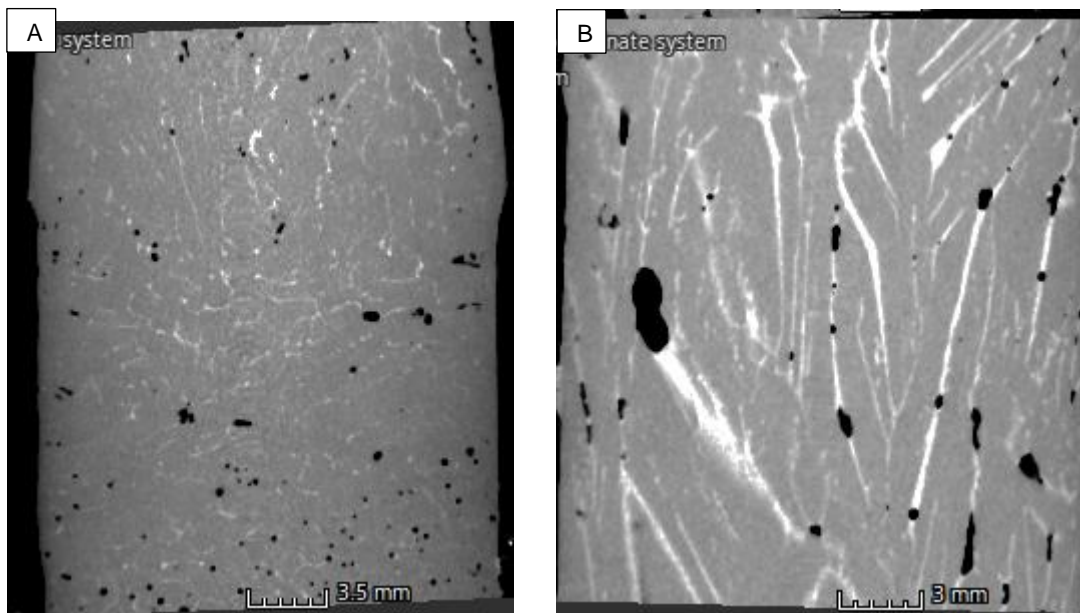


Figure 5-30 Micro-CT scan visuals for the top part of ice grown at -10°C from solutions of starting artificial ocean salinity of 30 psu (A) without EPS, (B) with EPS.

It should be noted that the method followed for preparing the EPS solution also significantly increased the starting solution salinity as EPS was added to a solution of a starting artificial ocean salinity of 30 psu. This is slightly different to the method used by Krembs *et al.* (2011),

where EPS and salt were both added to the water to make an overall solution of a starting artificial ocean salinity of 30 psu, significantly increasing the salt concentration.

Table 5.14 shows the structural analysis of brine and air inclusions for samples grown with and without EPS. The presence of EPS significantly increased the average diameter and surface area of both brine and air inclusions as expected. This can be attributed to the fact that the addition of EPS decreased the cooling rate of the sample as salinity increased, thus, increasing brine retention in the sample with EPS (Figure 5-11 and Figure 5-12). This is also supported by results in Table 5.5, showing that at any depth in ice during growth, the rate of change in temperature will be less for the ice sample grown in the presence of EPS compared to that grown without EPS.

Thus, the decreased cooling rate resulted in decreased number density of inclusions as they merged and elongated, increasing in average inclusion size (Eicken *et al.*, 2000). Furthermore, the decreased number density and increasing size of inclusions in this case also revealed an overall brine increase, the opposite of what was observed in Section 5.4.2 and 5.4.3. This is due to the significantly high starting artificial ocean salinity due to the addition of EPS. This suggests that the effect of EPS on brine volume is greater than that of the effect of decreased cooling rate, which resulted in decreased brine volume for increasing ambient temperature and increasing starting artificial ocean salinity.

Table 5.14 Size description of brine and air inclusions for the top part of ice grown from solutions of starting artificial ocean salinity of 30 psu at -10°C with and without EPS.

	Brine		Air	
	Top			
	Without EPS	With EPS	Without EPS	With EPS
Diameter (mm)	0.72	0.82	0.65	0.65
Surface Area (mm)	3.40	32.65	0.88	1.31
Sphericity	0.44	0.45	0.55	0.61
	Bottom			
Diameter (mm)	0.68	0.68	0.85	0.71
Surface Area (mm)	1.48	18.64	2.62	3.17
Sphericity	0.50	0.48	0.50	0.61

Since the presence of EPS increased the brine and air volume, the overall porosity of the artificial sea ice sample subsequently increased as seen in Figure 5-31. It can be seen that the addition of EPS increased ice porosity due to brine volume from 7.9% on the sample without EPS to 10.2% on the one with EPS. Additionally, the air inclusion volume also increased from 1.7% on the sample without EPS to 3.1% on the one with EPS. Thus, overall increasing ice porosity by 3.7%.

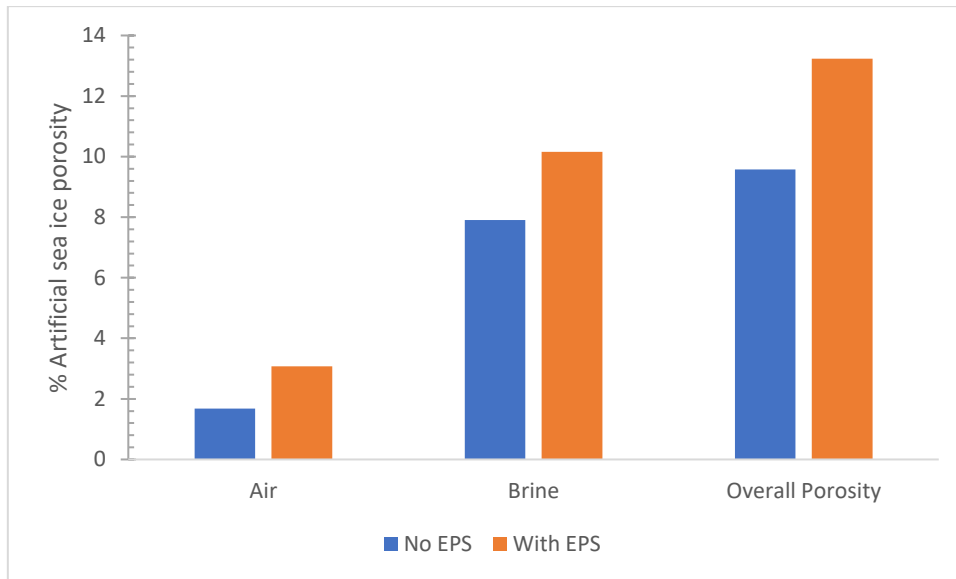


Figure 5-31 Porosity of artificial sea ice grown from solutions of starting artificial ocean salinity of 30 psu at -10°C with and without EPS.

It is not easy to deduce from these findings whether the sample permeability increased with the addition of EPS as the sample porosity increased. This is because porosity is the ability of the sample to hold or contain a fluid in its structure, while permeability is how easy the fluids flow through the structure of the sample. Krembs *et al.* (2011) alluded to the fact that an increase in ice porosity and brine retention does not necessarily increase the ice permeability. It was suggested that increased tortuosity could result in the overall effect of the presence of EPS being the reduced permeability and increased brine retention (Krembs *et al.*, 2011). This is attributed to the clogging effect of EPS which eventually plug the brine channels and hinder desalination processes. This explains the high brine retention for the sample with EPS as observed in Figure 5-12.

5.5 Analysis of artificial sea ice porosity computed from micro-CT scanning data vs. Frankenstein & Garner (1967) equations

Sea ice porosity is an important parameter used as one of the properties determining the strength of sea ice. Previous studies have suggested that the strength of sea ice increases with decreasing brine volume (Assur, 1960; Frankenstein and Garner, 1967). While brine volume is important for sea ice strength analysis, it is not very useful for determining the porosity of less saline ice such as multiyear ice since it has undergone desalination (Cox and Weeks, 1982). Thus, in this case, air volume determine porosity.

In this chapter, equations developed by Cox and Weeks (1982) from the basic equations reported by Frankenstein and Garner (1967) were used to calculate brine volume as seen in Appendix G. Assur (1960), in his work on determining the brine volume equations, states that the definition put forward by Zubov (1945) for brine content (the ratio of the salinity of ice and the salinity of brine) was incorrect. Additionally, the presence of solid salts was not considered. Assur (1960) adds that Anderson and Weeks (1958), later based their work of brine volume calculations on Zubov (1945), thus their findings were not sufficiently accurate. Furthermore, Assur (1960) state that Schwerdtfeger (1963) was the first to develop sea ice air volume calculations. However, these equations did not account for lower temperature conditions. Assur (1960) adds that Schwerdtfeger (1963) also assumed that the brine volume was equal to the volume of pure water (Cox and Weeks, 1982), which Assur (1960) did not agree .

Therefore, the equations reported by Frankenstein and Garner (1967) for calculating brine in sea ice were developed by considering what the other researchers omitted. In addition to this, Frankenstein and Garner (1967) provided equations with the temperature boundary limits as seen in Table G. 2.

The equations in Table G. 2 (Frankenstein and Garner, 1967) were used to calculate the brine volume for a temperature range of -8.2°C to -22.9°C, and verified using brine volume equation in Table G. 3 (Cox and Weeks, 1982). The calculated specific brine volume from both equations had a difference of approximately 5 - 10%.

The first column in Table G. 5 is the ice *in-situ* temperature, used to calculate the brine salinity (column 3) in the FG equations (Table G. 2) and ice density (column 4) according to the equation given in Table G. 3 (Cox and Weeks, 1982; Frankenstein and Garner, 1967). The ice bulk salinity was calculated using the effective distribution coefficient and the salinity of the starting solution as discussed in Section 2.5, see Table G. 5. The fifth and sixth columns in Table G.5 are the brine salinity multiplied by the ice density as correction suggested by Cox and Weeks (1982), and the FG brine volumes respectively. The specific brine volume is thus the ratio of the brine volume and brine density - from the work of Cox and Weeks (1982). The ninth column, shows the brine salinity calculated from Cox and Weeks equations (Table G. 3) with the constant used in the temperature range between -2°C and -22.9°C (Table G. 4). The specific brine, ice, and air volumes are calculated in column 10, 11, and 12 respectively, using Cox and Weeks equations (Table G. 3).

5.5.1 Effect of varying the starting artificial ocean salinity on artificial sea ice porosity

The volumes of air and brine were calculated for artificial sea ice grown at an ambient temperature of -10°C from solutions of varying starting artificial ocean salinity: 10 psu, 20 psu, and 30 psu. The specific brine and air volumes corresponding to -10°C in Tables G. 6, G. 7, and G. 8 were used to compute the overall ice porosity as shown in Figure 5-32. This figure shows the effect of varying the starting artificial ocean salinity on the artificial sea ice theoretical porosity. The difference between the ice porosity computed using theoretical methods and experimental methods, through ct-scanning, is discussed in this section.

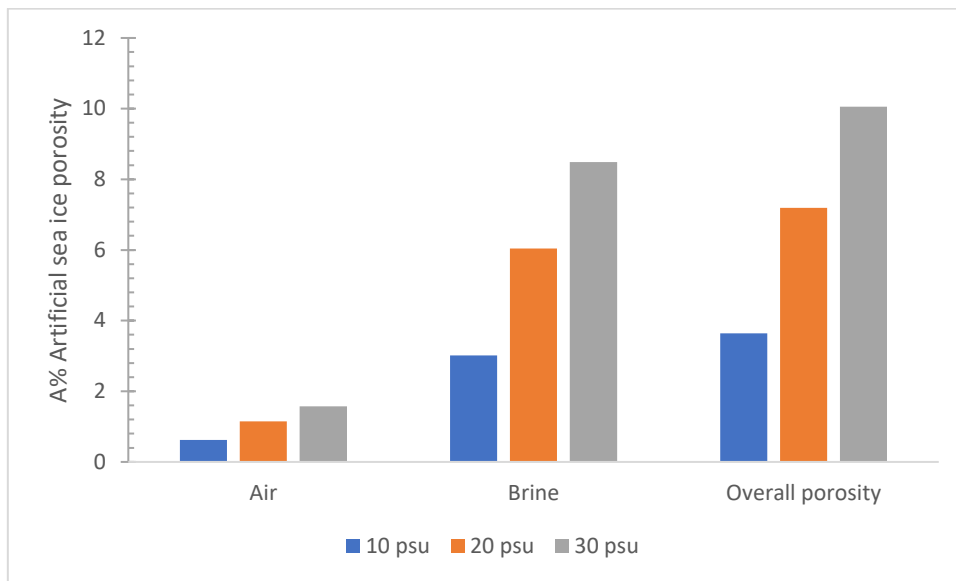


Figure 5-32 Theoretical porosity of artificial sea ice grown at -10°C from solutions of starting artificial ocean salinities of 10 psu, 20 psu, and 30 psu calculated from FG methods.

The overall artificial sea ice theoretical porosity increases with increasing starting artificial ocean salinity, as a result of the increasing brine and air volume as shown in Figure 5-32. The reasons for this increasing behaviour are as expected and explained in Section 5.4.2. It is also noted that although the trends are the same, the volumes obtained from the Frankenstein and Garner (FG) method yielded slightly higher volumes compared to those computed from the micro-CT data (Figure 5-27). The overall porosity computed from the micro-CT data and FG method is seen in Figure 5-33. Only the brine volumes were used for the comparison between the theoretical and experimental ice porosity of artificial sea ice since the contribution of brine is more significant to the porosity calculations than that of air.

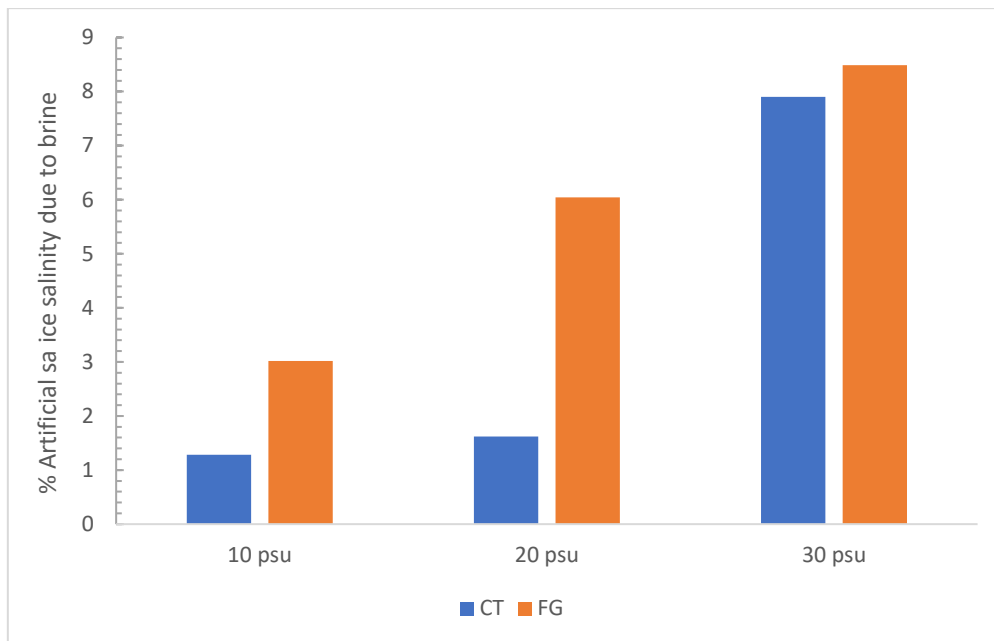


Figure 5-33 Graph showing the comparison between artificial sea ice porosity computed from micro-CT data and from Frankenstein and Garner (FG) methods for ice grown at -10°C from solutions of varying starting artificial ocean salinity.

The significant difference in brine volumes is seen on the sample grown from a 20 psu starting artificial ocean salinity solution, with the FG brine volume being approximately 73% more than the ct-scan computed volume. The smaller brine volume from the ct-scan data can be attributed to the factors affecting the scanning process such as the possible melting that was mentioned Section 5.4.2, as this might have caused brine drainage, resulting in the larger air pockets seen in Figure 5-26 B. The spatial resolution is also likely to have contributed to some smaller brine inclusions not being identified by the scanner as the smallest brine inclusion size that was recorded is 0.05 mm from a sample size of 20 mm x 20 mm x 20 mm (length x width x height). This implies that even if the sample contained a lot of inclusions smaller than 0.05 mm, they were not depicted by the scanner, hence the CT-scan volumes for the 10 psu and 20 psu samples are almost equal, while that of 30 psu is higher since it has more larger inclusions in size.

5.5.2 Effect of varying the ambient temperature on porosity

The volume of air and brine was calculated for artificial sea ice grown from a starting artificial ocean salinity of 30 psu at varying ambient temperatures: -20°C, -10°C, and -5°C. Table G. 6 shows the results of these calculations (Cox and Weeks, 1982).

Figure 5-34 shows the effect of increasing ambient temperature on the artificial sea ice theoretical porosity. It can be seen that increasing the ambient temperature decreased both the air and brine volume, thus decreasing the overall ice porosity. The difference between the porosity due to air volumes across the three samples at varying growth temperatures, ranges between 0.2 to 0.6, similar to the differences in the porosity due to air volumes of samples grown at varying solution salinities (Section 5.5.1). The striking difference between the results from varying the starting artificial ocean salinity and varying ambient temperature is the larger differences in the brine volumes at varying artificial ocean salinity. This implies that the starting artificial ocean salinity has more dominating effects to the brine content of the sample, and hence, to the overall porosity, compared to the effect of the ambient temperature.

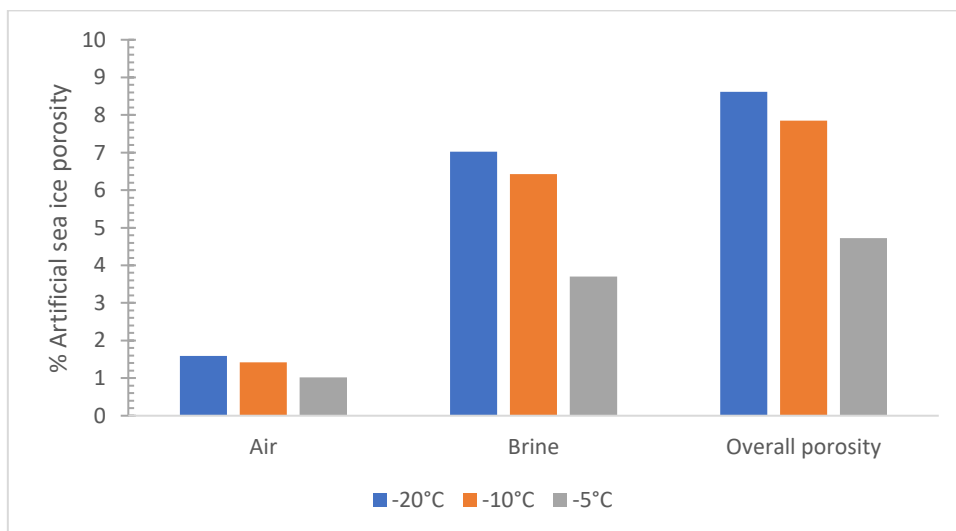


Figure 5-34 Theoretical porosity of artificial sea ice grown from solutions of starting artificial ocean salinity of 30 psu at -20°C, -10°C, and -5°C calculated from Frankenstein and Garner (FG) methods.

A comparison of artificial sea ice overall porosity as a function of ambient temperature for artificial sea ice calculated from the micro-CT data and FG methods is shown in Figure 5-35. As ambient temperature increases, the artificial sea ice porosity due to brine calculated from both the ct-scan data and FG methods decreased. However, the porosity calculated from FG methods decreased slightly by 0.6 between ambient temperatures of -20°C and -10°C, and 2.7 between -10°C and -5°C. While the differences in ice porosities computed from the ct-scan data were 0.7 between -20°C and -10°C, and 6.5 between -10°C and -5°C (Figure 5-35).

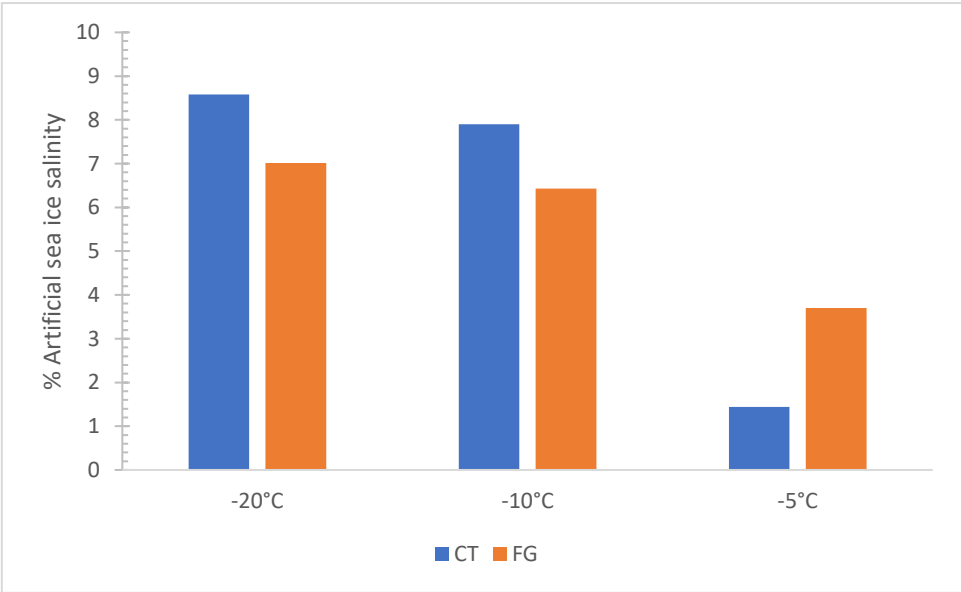


Figure 5-35 Graph showing the comparison between artificial sea ice porosity computed from micro-CT data and from Frankenstein and Garner (FG) methods for ice grown from solutions of starting artificial ocean salinity of 30 psu at varying ambient temperatures.

This shows that both the ct-scan data and FG methods yields similar results and trends for growth at lower and higher ambient temperatures. The significant difference from porosities between -10°C and -5°C can be attributed to a very low cooling rate at -5°C, hence the lower ice bulk salinity (Figure 5-8) and subsequent lower brine volume.

Section 5.5.1 show that ice porosities due to brine and air volumes computed using the CT-scan data and FG methods are comparable mostly at higher starting artificial ocean salinity for

ice grown from solutions of varying starting artificial ocean salinity. The discrepancy lies in the lower ct-scan data computed ice porosity resulting in differences of about 50% and 70% between the two methods for ice grown from solutions of 10 psu and 20 psu, respectively. In contrast, section 5.5.2 suggests ice porosities computed from ct-scan data and FG methods are not far off from each other for ice grown at varying ambient temperatures, with an 18% difference observed across all samples.

The lower percentage porosities computed from the ct-scan data can be attributed to the shortcomings introduced by image processing in CT-scanning. Image processing involve segmentation thresholding as a way to focus on area of interest in the image. Segmenting can result in some slush being classified as the brine phase, thus, overestimating the brine volume (Lieb-Lappen, 2016). Alternatively, segmenting slush with ice, which potentially underestimates the brine volume, thus, introducing inaccuracies in the brine and air volumes of sea ice. Lieb-Lappen (2016) recommends specifying segmentation thresholds that best splits the phases to avoid such errors.

The relationship between sample size and image resolution is also of importance on the analysis of brine and air inclusions. The study by Lieb-Lappen (2016) investigated the effect of increasing the scanned sample size on the resolution. They observed a 50% disagreement between the results due to a decrease in image resolution from 15 μm to 25 μm , indicating significant errors introduced in the overall analyses. For this study, a 2 cm x 2 cm x 2 cm size sample was chosen as the optimal size small enough to allow for high image resolution (Lieb-lappen, 2016; Pringle *et al.*, 2009), and large enough to be able to scan at least two sections from ice grown from a 3 L reactor (9 cm thick) and 4 sections from 30 L reactor (18 cm thick) to best represent the whole ice thickness

6 Overall Discussion

Sea ice growth patterns and behaviour have been reported to be largely affected by climate change (International Panel on Climate Change, 2014). This is evident through the decreasing ice extent and rising sea levels observed over the past years. *In-situ* studies on sea ice morphology and factors influencing sea ice growth are expensive, and present the challenge of studies being long term, with restricted control in terms of isolating variables of interest. Thus, laboratory experiments simulating the ocean environment to grow artificial sea ice offer an advantage of controlling the system and significantly reduces the period of the study.

The gap identified in the previous sea ice studies lies in the limited knowledge of the effect of different growth conditions on the growth and texture of sea ice. The aim of this research was to investigate factors such as ambient temperature and the starting artificial ocean salinity, as well as the presence of microorganism's secretions on sea ice morphology. The findings are intended to offer better understanding of the observed differences in the structure of sea ice grown from different environments, and how the structure of sea ice can interact with its environment.

6.1 Varying starting artificial ocean salinity

First-year and Multi-year ice were used to understand the effect of salinity on sea ice morphology because of their salinity difference. However, the limitation to this application was that the crystal structure differences between first-year and multi-year (Timco and Weeks, 2010) cannot be used to interrogate the crystal structure observed in this study. This is because the crystal structure in first-year and multi-year ice is due to mechanical deformation and thermal growth, not varying starting ocean salinity as far as this study is concerned. Multi-year ice is characterised by low salinities typically 0.5 psu to 5 psu, as it has survived two or

more summer melt seasons. Thus, it is less porous, with less brine inclusions. In contrast, first-year ice salinities range from 4 psu to 6 psu (Weeks and Ackley, 1982). This ice is usually less thick and mechanically weak because of the brine inclusions within the structure since it has not undergone desalination due to melting (Timco and Weeks, 2010).

The striking difference between the two types of ice is the relationship between the strength of ice (as a physical property) and the ice salinity. This depends on brine inclusions within the ice structure, which, in this case, was analysed through brine volume quantification. The findings from this study suggests that ice grown from a higher starting artificial ocean salinity had a lower cooling rate due to the freezing point depression phenomenon that occurs when the salinity of the solution is increased. Hence, this ice had high brine retention as a result of more brine inclusions in its structure, similar to Timco and Weeks (2010) description of first-year ice. Thus, explaining the lower growth rate estimated for ice grown from a solution of high starting artificial ocean salinity. Additionally, the crystal structure of this sample revealed bigger elongated and integrated brine inclusions, which are between elongated columnar crystals. In contrast, the sample grown from a solution of low starting artificial ocean salinity had smaller brine inclusions within its columnar crystals. There is no clear trend to the average crystal size with varying starting artificial ocean salinity. Furthermore, the overall ice porosity of the sample grown from a solution of high starting artificial ocean salinity was high, implying that the mechanical strength of this ice is weaker than that of the sample grown from a solution of low starting artificial ocean salinity.

6.2 Varying ambient temperature

Timco and Weeks (2010) mention that increasing ambient temperatures to approximately -8°C result in the solids salts present at low temperatures dissolving into liquid phase. The brine pockets grow bigger in size and merge to form brine drainage channels. This increases the porosity of sea ice. Eicken *et al.* (2000) reported the same findings, stating that the number

density of inclusions decreases with increasing ambient temperatures because of merging of inclusions during growth at higher ambient temperatures. Similarly, in this study elongated brine inclusions were observed with increasing ambient temperature from -20°C to -5°C. The structure of ice grown at a lower ambient temperature revealed a granular texture with more brine inclusions compared to the ice grown at a higher ambient temperature, which was dominated by columnar crystals and less brine inclusions. The average crystal sizes in all textures decreased with increasing ambient temperature. The growth rate of ice grown at a higher ambient temperature was low, thus explaining the presence of bigger columnar crystals.

The overall artificial sea ice porosity decreased with increasing ambient temperature. This observation was opposite to the findings of Cox and Weeks (1982) and Eicken *et al.* (2000), who reported an overall increase in ice porosity at high temperatures. This could be explained by the fact that the Eicken *et al.* (2000) investigated the thermal evolution of microstructure of sea ice between scanning temperatures of -25°C and -2°C. Implying that temperature gradients were imposed on natural sea ice samples collected and stored at approximately -25°C for later analysis. These were then kept in a cooling chamber, which allowed temperature manipulation, during data acquisition. In this study, however, ice was grown at varying ambient or atmospheric temperatures of -20°C, -10°C, and -5°C, stored at -18°C, and analysed at -10°C. It is assumed that warming of ice samples as done by Eicken *et al.* (2000), leads to melting, thus, increasing the size of brine inclusions as the sample drains. However, ice grown at a higher ambient temperature will be less porous due to the slower growth rate and hence, less salt entrapment. Thus, there will be fewer brine and air inclusions. This suggests that thermal evolution on any pre-grown ice will yield similar findings as Eicken *et al.* (2000), rather than results obtained in this study for ice grown from varying ambient temperature.

6.3 Varying reactor volume

Previous studies have reported artificial sea ice growth from reactors as small as 50 L, to larger test basins about 180 000 L (Nomura *et al.*, 2006 and Tison *et al.*, 2002). Studies of the sea ice crystal structure, however, have been limited to natural sea ice, and artificial sea ice growth from larger reactors as these offer an advantage of ease of sampling. Unlike most artificial sea ice studies investigating parameters that do not involve structural analysis, such as sea ice thermodynamics and gaseous fluxes, sea ice crystal structure and brine analysis studies require ice to be removed from its growth medium and sectioned for different analysis. Thus, this study explored the growth of artificial sea ice from a reactor volume as small as 3 L, where the ice was successfully sampled, sectioned, and analysed for crystal structure and porosity.

From comparison with ice grown at similar conditions from a 30 L reactor, it was found that ice grown from a 3 L reactor revealed a granular texture throughout, while, the latter revealed a columnar texture overlain by a small portion of granular at the top. Although the average granular crystal size decreased from the sample grown from the 3 L reactor to that of the 30 L reactor, overall, larger columnar crystals observed on the sample grown from a 30 L are evidence that the average crystal size increased with increasing reactor volume. Additionally, a higher brine retention was observed for the ice grown from the 3 L reactor due to a higher cooling rate experienced, hence a higher growth rate. This high cooling rate is a result of the 3 L reactor having a high surface-to-volume ratio, which enhances the heat transfer rate (Mukaromah *et al.*, 2016).

6.4 Presence of EPS

Krembs *et al.* (2011) investigated the effects of algal EPS on the microstructure and brine retention of artificial sea ice from ice grown from saline solutions containing EPS.

Photomicrographs obtained from this study at -10°C under polarized light revealed a structure with columnar crystals having brine inclusions between them. These crystals, however, were poorly ordered with no distinctive arrangement. In contrast, ice grown without EPS revealed ellipsoidal brine inclusions between columnar crystals, which appeared coarser than those in the ice with EPS (Krembs *et al.*, 2011). A similar observation was made in this study.

Both samples revealed granular (at the top) and columnar (at the bottom) textures, with the intermediate texture only exhibited in the sample grown without EPS. The intermediate texture could have been present, however, due to the sample with EPS looking blotchy with disordered crystals, it could have been hidden. Similar to Krembs's *et al.* (2011) observation, the columnar crystals in sample with EPS were smaller than those of the sample without EPS. This could be due to the presence of the bigger, interconnected brine inclusions, which significantly increased the sample brine content.

It was found that the sample with EPS retained more brine, thus expelling less into the underlying water. This could be explained by the small rounded features that could not be visually identified either as granular crystals, brine inclusions or EPS at the bottom of the cross polarisation EPS sample image. It is, therefore, assumed that these features could have hindered brine expulsions. The average size of air inclusions also increased with the addition of EPS. The above suggests that the presence of microorganisms in the ice matrix has a decreasing effect to the mechanical strength of ice. The high brine content and air inclusions increased the overall ice porosity. However, this does not imply direct proportionality with permeability since EPS plugs the brine channels and impedes desalination (Krembs *et al.*, 2011).

6.5 Theoretical vs. experimental methods for brine analysis

Frankenstein and Garner (1967) and Cox and Weeks (1982) equations were used to estimate brine and air volumes for each sample and quantify overall ice porosity due to brine and air thereafter. It was found that ice porosity increased with increasing starting artificial ocean salinity and decreased with increasing ambient temperature. This is similar to what was found through experimental methods (ct-scan data). The brine and air volume values from the theoretical methods were comparable to those from experimental methods. A difference of approximately 18% exists between artificial sea ice porosities computed using experimental methods and FG methods for ice growth at varying ambient temperatures. While, significant differences of about 50% between artificial sea ice porosities computed using the two methods are realised for ice grown from solutions of lower starting artificial ocean salinities (10 psu and 20 psu).

7 Conclusions and Recommendations

The following conclusions were drawn from this study:

- The growth rate increased with decreasing starting artificial ocean salinity, decreasing ambient temperature, as well as decreasing reactor volume.
 - Ice grown from a solution of a higher starting artificial ocean salinity had a lower cooling rate due to the freezing point depression phenomenon and delayed brine convection.
 - Since the solution density decreases with decreasing temperature, a higher cooling rate and, thus, freezing, are favoured by further lowering of the ambient temperature.
 - Heat transfer was enhanced in ice grown from a reactor with a high surface-to-volume ratio, thus, the smaller reactor had a high cooling rate.

- Varying ambient temperature and reactor volume revealed significant differences in artificial sea ice texture. However, there were minor differences in the textures as a result of varying starting artificial ocean salinity as well as the addition of EPS.
 - Besides the intermediate texture observed only from the sample grown from a solution of higher starting artificial ocean salinity, the average crystal size in both granular and columnar textures did not show any trend with varying starting artificial ocean salinity.
 - Varying ambient temperature and reactor volume revealed only the granular texture at a low ambient temperature and for ice grown from a smaller reactor. A smaller percentage of granular at the top and a dominating columnar texture at higher ambient temperatures, and for ice grown from a larger reactor, were observed respectively.
 - The textures identified, and their arrangement on the sample without EPS were present in the sample with EPS. However, due to the disordered arrangement of crystals and the blotchiness on the sample with EPS, the intermediate texture was not identified, and crystal dimensions could not be properly measured.

- The overall artificial sea ice porosity increased with increasing starting artificial ocean salinity, decreasing ambient temperature, and with the addition of EPS.
 - There was a shift in the ice temperatures and salinity profiles towards the warmer ambient temperatures and higher salinities, respectively, with increasing starting artificial ocean salinity. Thus, increasing the ice porosity.
 - Since there were many small rounded granular crystals in ice grown from reactors with higher surface-to-volume ratio and at low ambient temperatures, the brine volume increased due to many brine inclusions between crystals, thus increasing the porosity of the ice.
 - There was more brine retained in the sample with EPS, thus, the overall ice porosity significantly increased.

- Theoretical methods for brine analysis yielded comparable volumes to the volumes calculated using experimental data from the CT-scan results. However, significant differences (50%) were observed between the two methods for ice grown from solutions of lower starting artificial ocean salinities, and only a difference of 18% for ice grown at varying ambient temperatures. Brine volumes computed from the ct-scan data were lower for ice grown from solutions of lower starting artificial ocean salinity.

It is in the nature of every study to have some aspects identified to be improved for future work.

Thus, the following recommendations are made:

- The growth period of the -5°C experimental run should be extended to more than 336 hours since it only grew to a thickness of 5 cm in 168 hours. This will be important as evidence of the assumption made about the columnar texture percentage increasing with increasing ambient temperature.

- Smaller temperature probes (probe diameter approximately 1 mm) should be installed in the 3 L reactor to allow fitting of more probes, and thus, maximising resolution.
- The ct-scan data for ice grown from solutions of starting artificial ocean salinities of 10 psu and 20 psu should be investigated further for validation of comparison of the overall ice porosities computed from both the theoretical calculations and ct-scan data. This will confirm whether, there is a difference between computing brine and air inclusions using theoretical and experimental methods or not.

8 References

- Ackley, S. F. and Weeks, W. F. (1990) 'Sea ice Properties and Processes', in. United States of America.
- Assur, A. (1960) 'Composition of Sea Ice and its Tensile Strength', *SIPRE Research Report*, 44, p. 54.
- Aussillous, P., Sederman, A., Gladden, L., Huppert, H. and Worster, M. (2006) 'Magnetic resonance imaging of structure and convection in solidifying mushy layers', *Journal of Fluid Mechanics*, 552, pp. 99–125. doi: 10.1017/S0022112005008451.
- Bancroft JD. and Gamble M. Theory and practice of histological techniques ed. 6, Churchill Livingstone Inc. 2008. Edinburgh.
- Butler, B., Papadimitriou, S., & Kennedy, H. (2016). The effect of mirabilite precipitation on the absolute and practical salinities of sea ice brines. *Marine Chemistry*, 184, 21–31. <https://doi.org/10.1016/j.marchem.2016.06.003>
- Brierley, A. S. and Thomas, D. N. (2002) *Ecology of Southern Ocean pack ice, Advances in Marine Biology*. doi: 10.1016/S0065-2881(02)43005-2.
- Campbell, H. R. B. G. M., Klinck, R. J., MacNeil, J. A., and Boyd, S. K.: Automatic Segmentation of Cortical and Trabecular Compartments Based on a Dual Threshold Technique for In Vivo Micro-CT Bone Analysis, *Bone*, 41, 505–515, 2007.
- Chester, C. and Langway, J. (1958) *Ice Fabrics and the Universal Stage*.
- Cottier, F. and Wadhams, P. (1999) 'Linkages between salinity and brine channel distribution in young sea ice', *Polar Research*, 104, pp. 859–871.
- Cox, G. F. N and Weeks, W. F. (1975) 'Brine drainage and initial salt entrapment in sodium chloride ice', (345)
- Cox, G. F. N. and Weeks, W. F. (1982) 'Equations for Determining the Gas and Brine Volumes in Sea Ice Samples.', *CRREL Report (US Army Cold Regions Research and Engineering Laboratory)*, 29(102), pp. 306–316. doi: 10.3189/s0022143000008364.

- Doble, M. J., Coon, M. D. and Wadhams, P. (2003) 'Pancake ice formation in the Weddell Sea', *Journal of Geophysical Research C: Oceans*, 108(7), pp. 2–1. doi: 10.1029/2002jc001373.
- Dumont, I., Schoemann, V., Lannuzel, D., Chou, L., Tison, J. and Becquevort, S. (2009) 'Distribution and characterization of dissolved and particulate organic matter in Antarctic pack ice Distribution and characterization of dissolved and particulate organic matter in Antarctic pack ice', *Polar Biology*, (June 2014). doi: 10.1007/s00300-008-0577-y.
- Durand, Gaël; Gagliardini, O.; Thorsteinsson, Throstur; Svensson, Anders; Kipfstuhl, Sepp; Dahl-Jensen, Dorthe (2006). Ice microstructure and fabric: an up-to-date approach for measuring textures. *Journal of Glaciology*, 52(179), 619–630. doi:10.3189/172756506781828377
- Eicken, H. (1992) 'Salinity Profiles of Antarctic Sea Ice: Field Data and Model Results', *Geophysical Research*, 97(92).
- Eicken, H., Bock, C., Wittig, R., Miller, H. and Poertner, H. (2000) 'Magnetic resonance imaging of sea-ice pore fluids: Methods and thermal evolution of pore microstructure', *Cold Regions Science and Technology*, 31(3), pp. 207–225. doi: 10.1016/S0165-232X(00)00016-1.
- Eicken, H. and Lange, M. A. (1989) 'Development and properties of sea ice in the coastal regime of the southeastern Weddell Sea', *Journal of Geophysical Research*, 94(C6), p. 8193. doi: 10.1029/jc094ic06p08193.
- Eicken, H. and Petrich, C. (2017) 'Overview of sea ice growth and properties', in Thomas, David N. (School of Ocean Sciences, Bangor University, U. (ed.) *Sea Ice*. Third. United Kingdom: John Wiley & Sons, Ltd.
- Frankenstein, G. and Garner, R. (1967) 'Short Note Equations for Determining the Brine Volume', *Journal of Glaciology*, 6(48), pp. 943–944.
- Fukutomi, T., K. Kusunoki and T. Tabata (1951) Study of sea ice: On chlorinity of the coastal land ice observed at Abashiri and Monbetsu in Hokkaido. *Low Temperature Science*, Series A(6).
- Gay, M. and J. Weiss. 1999. Automatic reconstruction of polycrystalline ice microstructure from

- image analysis: application to the EPICA ice core at Dome Concordia, Antarctica. *J. Glaciol.*, 45(151), 547–554.
- Genck, J. W. (1969) 'Temperature effects on growth and nucleation rates in mixed suspension crystallization'. Available at: <https://lib.dr.iastate.edu/rtd/4105>.
- Golden, K. M., Eicken, H., Heaton, A., Minor, J., Pringle, D. and Zhou, J. (2007) 'Thermal evolution of permeability and microstructure in sea ice', *Geophysical Research Letters*, 34(16), pp. 2–7. doi: 10.1029/2007GL030447.
- Gow, A. J., Ackley, S., Buck, K. and Golden, K. (1987) *Physical and structural characteristics of Weddell Sea pack ice*. United States of America.
- Gow, A. J. and Tucker, W. B. (1991) *Physical and Dynamic Properties of Sea Ice in the Polar Oceans*. Hanover, New Hampshire.
- Gow, A. J. and Weeks, W. F. (1977) 'Internal Structure of Fast Ice Near Narwhal Island, Beaufort Sea, Alaska.', *CRREL Rep*, (77–29).
- Haas, C., Cottier, F., Smedsrud, L., Thomas, D., Buchmann, U., Dethleff, D., Gerland, S., Giannelli, V., Hoelemann, J., Tison, J-L. and Wadhams, P. (1999) 'Multidisciplinary ice tank study shedding new light on sea ice growth processes', *Eos*, 80(43), pp. 507–513. doi: 10.1029/EO080i043p00507-01.
- Haas, C. (1999) 'Ice tank investigations of the microstructure of artificial sea ice grown under different boundary conditions during interice II', pp. 1–8.
- Hall, B (2019). 'Design of a Small-Scale System for the Growth of Artificial Sea Ice'. Master of Science. University of Cape Town
- Handley WS. A Method of Obtaining Uniplanar Sections with the Ordinary Rocking Microtome. *J Anat Physiol*. 1903 April; 37(Pt 3): 290-292.
- Havik, L. (2011) 'Growing Ice in a Tank: Young Sea Ice Evolution and Turbulence in the Under Ice Boundary Layer (DRAFT)', (November).
- Hopkins, F. F., I. L. Morgan, H. D. Ellinger, R. V. Klinksiek, G. A. Meyer, and J. N. Thompson, Industrial tomography applications, *IEEE Trans. Nucl. Sci.*, NS-28, 1717-1720, 1981
- International Panel on Climate Change (2014) *Climate Change 2014: Synthesis Report*.

- Contribution, Contribution of Working Groups I, II and III to the Fifth Assessment Report of the Intergovernmental Panel on Climate Change*. doi: 10.1046/j.1365-2559.2002.1340a.x.
- Jeffries, M., Shaw, R., Morris, K., Veazey, A. and Krouse, H. (1994) 'Crystal structure, stable isotopes, and development of sea ice in the Ross, Amundsen, and Bellingshausen seas, Antarctica', 99(93), pp. 985–995.
- Johnson, S (2020). 'Evaluation of the Changes in the Crystal Structure of Antarctic Sea Ice from the Marginal Ice Zone during Winter and Spring'. Master of Science. University of Cape Town
- Kawamura, T. (1988) 'Observations of the internal structure of sea ice by X ray computed tomography', *Journal of Geophysical Research*, 93(C3), p. 2343. doi: 10.1029/jc093ic03p02343.
- Kawamura, T. (1990) 'Nondestructive, Three-Dimensional Density Measurements of Ice Core Samples by X-Ray Computed Tomography', *Geophysical Research*, 95(B8), pp. 407–412. doi: 10.1029/jb095ib08p12407.
- Kovacs, A. (1996) 'Sea Ice Part I . Bulk Salinity Versus Ice Floe Thickness', *CRREL Report*, 7(June), pp. 1–23.
- Krembs, C., Eicken, H. and Deming, J. W. (2011) 'Exopolymer alteration of physical properties of sea ice and implications for ice habitability and biogeochemistry in a warmer Arctic', 108(9), pp. 3653–3658. doi: 10.1073/pnas.1100701108.
- Kuehn, G. A., Lee, W.A. and Schulson E.M. (1987) 'The Structure and Tensile Behavior of First Year Sea Ice and Laboratory-Grown Saline Ice by', 1987(September).
- Landis, E. N. and Keane, D. T.: X-Ray Microtomography, *Mater. Charact.*, 61, 1305–1316, 2010.
- Langway, C.C., Jr. 1958. Ice fabrics and the universal stage. SIPRE Tech. Rep. 62.
- Lubatschowski H. Laser Microtomy. WILEY-VCH Verlag GmbH, Biophotonics. 2007; 49-51.
- Lepparanta, M. (1993) 'A review of analytical models of sea-ice growth', *Atmosphere - Ocean*, 31(1), pp. 123–138. doi: 10.1080/07055900.1993.9649465.
- Lewis, A., Seckler, M., Kramer, H. and van Rosmalen, G. (2015a) 'Crystal growth', in *Industrial*

- Crystallization: Fundamentals and Applications*. Cambridge University Press, pp. 12–15.
doi: 10.1002/j.2326-1951.1966.tb00236.x.
- Lewis, A., Seckler, M., Kramer, H. and van Rosmalen, G. (2015b) 'Nucleation', in *Industrial Crystallization: Fundamentals and Applications*. Cambridge University Press. Available at: <https://www.cambridge.org/core/terms>. <https://doi.org/10.1017/CBO9781107280427.005>.
- Lieb-lappen, R. (2016) *How sea ice microstructure influences the polar transport of salts from the ocean into the atmosphere*. Dartmouth College.
- Løset, S., Shkhinek, K., Gudmestad, O. and Høyland, K. (2006) *Actions from ice on Arctic offshore and coastal structures*. St. Petersburg, Moscow, Krasnodar.
- Mohammed, Arishiya, Mohamed. Microtomes Review Article and Microtome Knives – A Review and Proposed Classification. *Annal Dent Univ Malaya* 2012; 19(2): 43–50.
- Marks, Amelia A., Lamare, M. L. and King, M. D. (2017) 'Optical properties of sea ice doped with black carbon -An experimental and radiative-Transfer modelling comparison', *Cryosphere*, 11(6), pp. 2867–2881. doi: 10.5194/tc-11-2867-2017.
- Maslanik J, Stroeve J, Fowler C and EmeryW(2011) Distribution and trends in Arctic sea ice age through spring 2011. *Geophys. Res. Lett.*, 38(13), L13502 (doi: 10.1029/2011GL047735)
- Maykut, G. A. (1985) *An introduction to ice in the polar oceans*.
- Middleton, C. A., Thomas, C., De Wit, A and Tison, J-L. (2016) 'Visualizing brine channel development and convective processes during artificial sea-ice growth using Schlieren optical methods', *Journal of Glaciology*, 62(231), pp. 1–17. doi: 10.1017/jog.2015.1.
- Mukaromah, A. H., Kadja, G., Mukti, R., Pratama, I., Zulfikar, M. and Buchari. (2016) 'Surface-to-volume ratio of synthesis reactor vessel governing low temperature crystallization of ZSM-5', *Journal of Mathematical and Fundamental Sciences*, 48(3), pp. 241–251. doi: 10.5614/j.math.fund.sci.2016.48.3.5.
- Nakawo, M.; Sinha, N. K (1981). Growth Rate and Salinity Profile of First-Year Sea Ice in the High Arctic. *Journal of Glaciology*, 27(96), 315–330. doi:10.1017/S0022143000015409
- Nelson, K. H., & Thompson, T. G. (1954). Deposition of salts from sea water by frigid

- concentration, Technical Report 29 (30 pp.). Seattle, WA: Office of Naval Research.
- Nomura, D., Yoshikawa-Inoue, H. and Toyota, T. (2006) 'The effect of sea-ice growth on air-sea CO₂ flux in a tank experiment', *Tellus, Series B: Chemical and Physical Meteorology*, 58(5), pp. 418–426. doi: 10.1111/j.1600-0889.2006.00204.x.
- Notz, D., J. S. Wettlaufer, and M. G. Worster (2005), A non-destructive method for measuring the salinity and solid fraction of growing sea ice in situ, *J. Glaciol.*, 51(172), 159–166.
- Notz, Dirk; Worster, M. Grae (2009). Desalination processes of sea ice revisited. *Journal of Geophysical Research*, 114(C5), C05006–. doi:10.1029/2008jc004885
- Palermo, J. A. and Grove, C. S. (1964) 'Some variables affecting the rate of crystal growth in aqueous solutions', *AIChE Journal*, 10(3), pp. 351–356. doi: 10.1002/aic.690100314.
- Papadimitriou, S., Kennedy, H., Kattner, G., Dieckmann, G and Thomas, D. (2004) 'Experimental evidence for carbonate precipitation and CO₂ degassing during sea ice formation', *Geochimica et Cosmochimica Acta*, 68(8), pp. 1749–1761. doi: 10.1016/j.gca.2003.07.004.
- Perovich, D. K. and Gow, A. J. (1991) 'A statistical description of the microstructure of young sea ice', *Journal of Geophysical Research*, 96(C9), p. 16943. doi: 10.1029/91jc01594.
- Perovich, D. K. and Gow, A. J. (1996) 'A quantitative description of sea ice inclusions', *Journal of Geophysical Research C: Oceans*, 101(C8), pp. 18327–18343. doi: 10.1029/96JC01688.
- Petrich, C. and Eicken, H. (2017) 'Overview of sea ice growth and properties', in Thomas, D. N. (ed.) *Sea Ice*. Third. Chichester, UK: John Wiley & Sons, Ltd, pp. 1–37. doi: 10.1002/9781118778371.
- Pringle, D., J. Miner, R. Glantz, M. Hilpert, and H. Eicken (2006), Temperature-dependent pore space of sea ice: X-ray computed tomography and dual model network analysis, *Eos Trans. AGU*, 87(52), Fall Meet. Suppl., Abstract H51F– 0545.
- Prodanovic, M., W. B. Lindquist, and R. S. Seright (2006), Porous structure and fluid partitioning in polyethylene cores from 3D X-ray microtomographic imaging, *J. Colloid Interface Sci.*, 298, 282–297.

- Rozmanov, D. & Kusalik, P. G., 2011. Temperature dependence of crystal growth of hexagonal ice (I-h). *Physical Chemistry Chemical Physics*, September
- Schulson, E. M., Renshaw, C. E. and Snyder, S. A. (2015) 'Effect of Deformation Damage on the Mechanical Behavior of Sea Ice : Ductile-Brittle Transition , Elastic Modulus and Brittle Compressive Strength', (July).
- Shekunov, B. Y., Aulton, M., Adama-Acquash, R. and Grant, D. (1996) 'Effect of temperature on crystal growth and crystal properties of paracetamol', 1(c), pp. 439–444.
- Stock, S. R. (2008). Recent advances in X-ray microtomography applied to materials. , 53(3), 129–181. doi:10.1179/174328008x277803
- Svensson, A. (2004) *Mapping the crystal structure of ice*. Available at: http://www.iceandclimate.nbi.ku.dk/research/drill_analysing/cutting_and_analysing_ice_cores/crystal_structure/ (Accessed: 28 April 2020).
- Thorsteinsson, T. 1996. Textures and fabrics in the GRIP ice core, in relation to climate history and ice deformation. *Ber. Polarforsch./ Rep. Pol. Res.* 205.
- Timco, G. W. and Weeks, W. F. (2010) 'Engineering Properties of Sea Ice: A review of the engineering properties of sea ice', *Cold Regions Science and Technology*. Elsevier B.V., 60(2), pp. 107–129. doi: 10.1016/j.coldregions.2009.10.003.
- Tison, J-L., Haas, C., Sleewaegen, S. and Bernard, A. (2002) 'Tank study of physico-chemical controls on gas content and composition during growth of young sea ice', *Journal of Glaciology*, 48(161), pp. 177–190. doi: 10.3189/172756502781831377.
- Toth D. and Lerman A. (1975). Stratified Lake and Oceanic Brines: Salt Movement and Time Limits of Existence. *Limnology and Oceanography*, 20(5), 715–728. doi:10.2307/2834955
- Tucker, W. B., Perovich, D., Gow, A., Weeks, W. and Drinkwater. (1992) 'Physical properties of sea ice relevant to remote sensing', *Geophysical Research*, 68, pp. 9–28. doi: 10.1029/gm068p0009.
- Underwood, E.E. 1970. Quantitative stereology. Reading, MA, Addison-Wesley Publishing.
- United Nations (2020) *Sustainable Development Goal 13: Climate Action*. Available at: <https://www.unoosa.org/oosa/en/ourwork/space4sdgs/sdg13.html#:~:text=Sustainable>

Development Goal 13 urges, today and even more tomorrow. (Accessed: 25 October 2020).

Vancoppenolle, M., Madec, G., Thomas, M., & McDougall, T. J. (2019). Thermodynamics of sea ice phase composition revisited. *Journal of Geophysical Research: Oceans*, 124, 615–634. <https://doi.org/10.1029/2018JC014611>

Weast, R.C. (1971). *Handbook of chemistry and physics. Fifty-second edition*. Cleveland, OH, Chemical Rubber Co.

Weeks WF (2010) On Sea-Ice. University of Alaska Press, Fairbanks, Alaska, 144–190, 520–540

Weeks, W. . and Ackley, S. . (1982) *The growth, structure, and properties of sea ice*. Hanover, New Hampshire.

Weeks, W. F. and Cox, G. (1988) *REPORT 88-1 3 Profile properties of undeformed first-year sea ice*.

Wei, M., Polojarvi, A., Cole, D. and Prasanna, M. (2020) 'Strain response and energy dissipation of floating saline ice under cyclic Strain response and energy dissipation of floating saline ice under cyclic compressive stress', (2015). doi: 10.5194/tc-14-2849-2020.

Weissenberger, J., Dieckmann, G., Gradinger, R. and Spindler, M. (1992) 'Sea ice: A cast technique to examine and analyze brine pockets and channel structure', *Limnology and Oceanography*, 37(1), pp. 179–183. doi: 10.4319/lo.1992.37.1.0179.

Wettlaufer, J. S., Worster, M. G. and Huppert, H. E. (1997) 'Natural convection during solidification of an alloy from above with application to the evolution of sea ice', *Journal of Fluid Mechanics*, 344, pp. 291–316. doi: 10.1017/S0022112097006022.

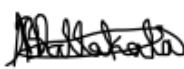
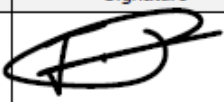

Wiese, M. (2012) 'Laboratory experiments on the thermodynamics of melting sea ice', (September), p. 72.

Wilén, L. A. (2000) 'A new technique for ice-fabric analysis', 46(1984).

Yun, Wang; Azuma, Nobuhiko (1999). A new automatic ice-fabric analyzer which uses image-analysis techniques. *Annals of Glaciology*, 29(1), 155–162. doi:10.3189/172756499781821021

Appendices

A. Study Ethics Clearance

Application for Approval of Ethics in Research (EIR) Projects Faculty of Engineering and the Built Environment, University of Cape Town				
ETHICS APPLICATION FORM				
Please Note: Any person planning to undertake research in the Faculty of Engineering and the Built Environment (EBE) at the University of Cape Town is required to complete this form before collecting or analysing data. The objective of submitting this application <i>prior</i> to embarking on research is to ensure that the highest ethical standards in research, conducted under the auspices of the EBE Faculty, are met. Please ensure that you have read, and understood the EBE Ethics in Research Handbook (available from the UCT EBE, Research Ethics website) prior to completing this application form: http://www.ebe.uct.ac.za/ebe/research/ethics1				
APPLICANT'S DETAILS				
Name of principal researcher, student or external applicant		Boitumelo Matlakala		
Department		Engineering and Built Environment		
Preferred email address of applicant:		mtlboi008@myuct.ac.za		
If Student	Your Degree: e.g., MSc, PhD, etc.	MSc		
	Credit Value of Research: e.g., 60/120/180/360 etc.	180		
	Name of Supervisor (if supervised):	Tokoloho Rampai		
If this is a research contract, indicate the source of funding/sponsorship		National Research Foundation (NRF)		
Project Title		Factors affecting sea ice morphology		
<p>I hereby undertake to carry out my research in such a way that:</p> <ul style="list-style-type: none"> • there is no apparent legal objection to the nature or the method of research; and • the research will not compromise staff or students or the other responsibilities of the University; • the stated objective will be achieved, and the findings will have a high degree of validity; • limitations and alternative interpretations will be considered; • the findings could be subject to peer review and publicly available; and • I will comply with the conventions of copyright and avoid any practice that would constitute plagiarism. 				
APPLICATION BY		Full name	Signature	Date
Principal Researcher/ Student/External applicant		Boitumelo Matlakala		05/05/2020
SUPPORTED BY		Full name	Signature	Date
Supervisor (where applicable)		Tokoloho Rampai		06/05/20
APPROVED BY		Full name	Signature	Date
HOD (or delegated nominee) Final authority for all applicants who have answered NO to all questions in Section 1; and for all Undergraduate research (Including Honours).		Prof H von Blotnitz		10/08/2020
Chair: Faculty EIR Committee For applicants other than undergraduate students who have answered YES to any of the questions in Section 1.				

B. Standard Operating Procedures

B. 1 Artificial sea ice growth

1. Fill the reactors with deionised water to a height of 20 cm in order to make a solution of 3 L in reactor with working diameter of 14 cm.
2. Measure and mix 30 g, 60 g, and 90 g of Aquaforest Sea Salt into deionised water to make solutions of 10 psu, 20 psu, and 30 psu salinity.
3. Layer the bottom insulation (5 mm wooden and polystyrene boards), and magnetic stirrers on the bench in the polar lab. Then place the reactors on top of the magnetic stirrers.
4. Activate the fan placed 1 m away from the reactors and facing the surface of reactors, by turning the dial to 1.
5. Switch on the magnetic stirrers by turning the dial to 0.4 and insert the temperature probes mounted on the PVC scaffold for growth dynamics experiments and begin pre-cooling by decreasing the lab temperature to 1°C. For crystal structure experiments, omit the probes in the set up.
6. After 12 hours to 24 hours of pre-cooling, insulate the walls of the reactors using 15 cm isotherm covered in black plastic as seen in Figure B. 1



Figure B. 1 Experimental set-up showing reactor side and bottom insulation

7. Decrease the lab temperature to the desired growth ambient temperature and use the ice shavings to seed the solutions once the surface starts to freeze. Seeding is necessary to avoid supercooling.
8. After seeding, leave the reactors for 16 hours, 42 hours, or 160 for artificial sea ice growth at -20°C, -10°C, and -5°C respectively.
9. Post growth, collect temperature data from the logger for growth dynamics experiments and melt the ice by increasing the ambient temperature to 25°C. Otherwise, follow the next section for the sampling procedure.

B. 2 Reactor Insulation

It is required that the heat of convection (Q_c) from the top to bottom of tank be greater than the conduction heat from the tank walls (Q_w). This is because as ice thickness increases during growth, it acts as an insulator preventing effective further cooling from cold air to water in the tank (under the ice).

Heat transfer from the bottom of the tank is assumed to be very small to negligent since the tank is placed on top of a magnetic stirrer, wooden plate and a polystyrene plate.

Thus, heat transfer to the tank is from the top and the walls as follows:

$$Q_c = h_o A (T_w - T_a)$$

B. 2 - 1

$$Q_w = \frac{kA(T_w - T_a)}{L}$$

B. 2 - 2

Where: Q_c is the convective heat

Q_w is the conduction heat

h_o is the heat transfer coefficient of air for forced cooling

k is the thermal conductivity of isotherm (material of insulation)

A is the surface area of heat transfer

T_w is the wall temperature and

T_a is the air temperature

L is the insulation thickness

As stated above, it is required that $Q_c \gg Q_w$, thus

$$Q_c \gg Q_w$$

$$h_o A (T_w - T_a) \gg \frac{k A (T_w - T_a)}{L}$$

B. 2 - 3

Since the term $A(T_w - T_a)$ is the same for equation 4 and 5, it cancels out and equation 7 below

is the result:

$$h_o \gg \frac{k}{L}$$

B. 2 - 4

For $Q_c \gg 100Q_w$

$$h_o = 100 \frac{k}{L}$$

$$L = 100 \frac{k}{h_o}$$

$$L = 100 \frac{0.046 \frac{W}{m \cdot K}}{30 \frac{W}{m^2 \cdot K}}$$

$$L = 0.15 \text{ m (15 cm)}$$

For $Q_c \gg 10Q_w$

$$L = 0.015 \text{ m (1.5 cm)}$$

Thus, the range of insulation thickness to choose from is 1.5 cm to 15 cm using isotherm as material of construction.

B. 3 Artificial sea ice sampling procedure

1. Place the wooden board on the bench top to prevent slipping and melting of ice during cutting.
2. Use a heat gun on the walls of the reactor to free the ice for ease of removal.
3. Flip the reactor upside down to remove the ice and collect the underlying artificial seawater for measuring water salinity.
4. Use the thermal cutter to cut the artificial sea ice into dimensions required for analytical techniques used for visualisation of crystal structure and brine as seen in Figure B. 2

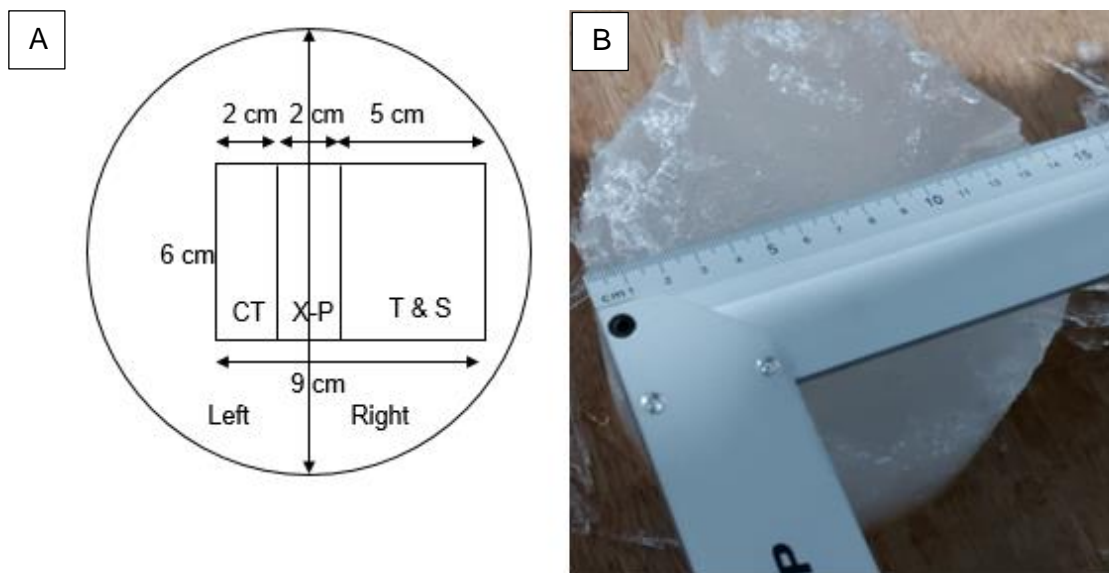


Figure B. 2 (A) Top view of reactor after ice growth experiments showing where ice specimen was sampled from the reactor (B) Top view of artificial sea ice after growth

5. Depending on how thick the artificial sea ice sample is, further cut the Salinity sample into equal sections from top down and place into well labelled plastic containers to melt overnight.
6. Use a handheld AZ 8303 Cond./Temp./Logger to record conductivity and temperature, and thus, calculate the artificial sea ice bulk salinity.
7. Cut the X-P sample into half resulting into two 1 cm x 6 cm slabs (top view) to allow for a duplicate in case one sample breaks during cutting. These should be covered in bubble wrap, label top and bottom clearly, and stored in the -18°C freezer for cross polarisation analysis the next day.
8. Further cut the CT sample into 2 cm x 2 cm x 5 cm (dimensioned required for fitting into the ct scanner chamber) and cover with bubble wrap, label top and bottom clearly, and stored in the -18°C freezer for analysis on the scheduled day.

C. Thermodynamics and Physical Properties of Artificial Sea Ice

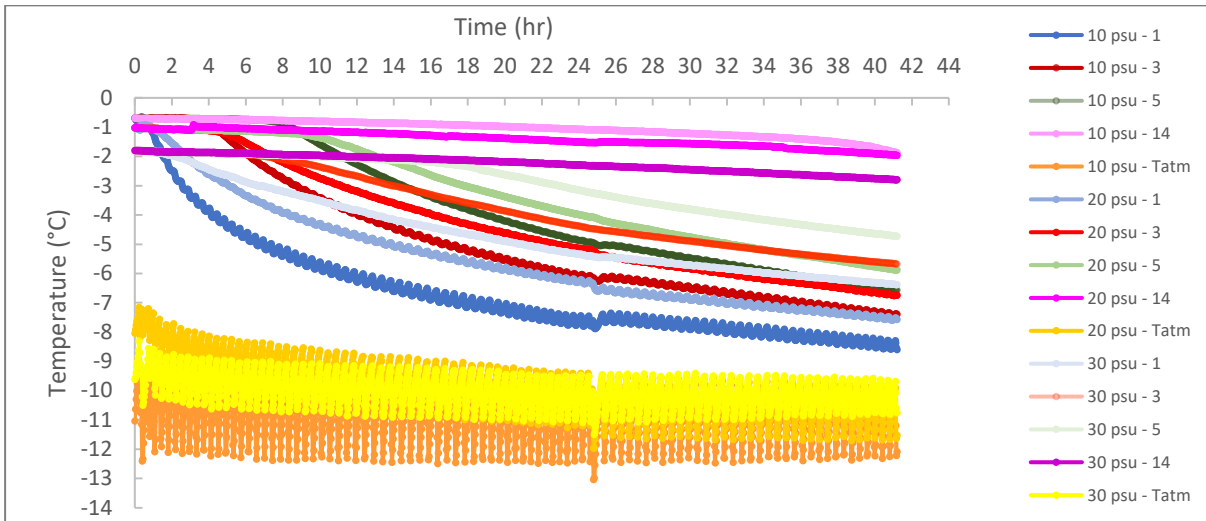


Figure C. 1 Temperature time graphs for ice grown at -10°C from solutions of starting artificial ocean salinities of 10 psu, 20 psu and 30 psu

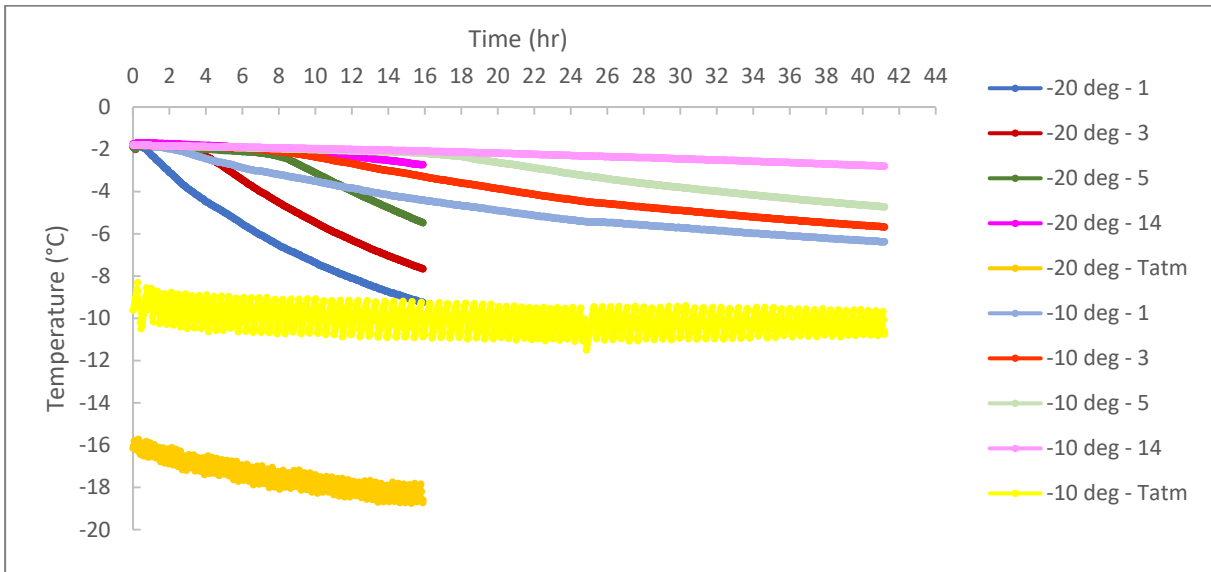


Figure C. 2 Temperature time graphs for ice grown from solutions of starting artificial ocean salinity of 30 psu at -20°C and -10°C .

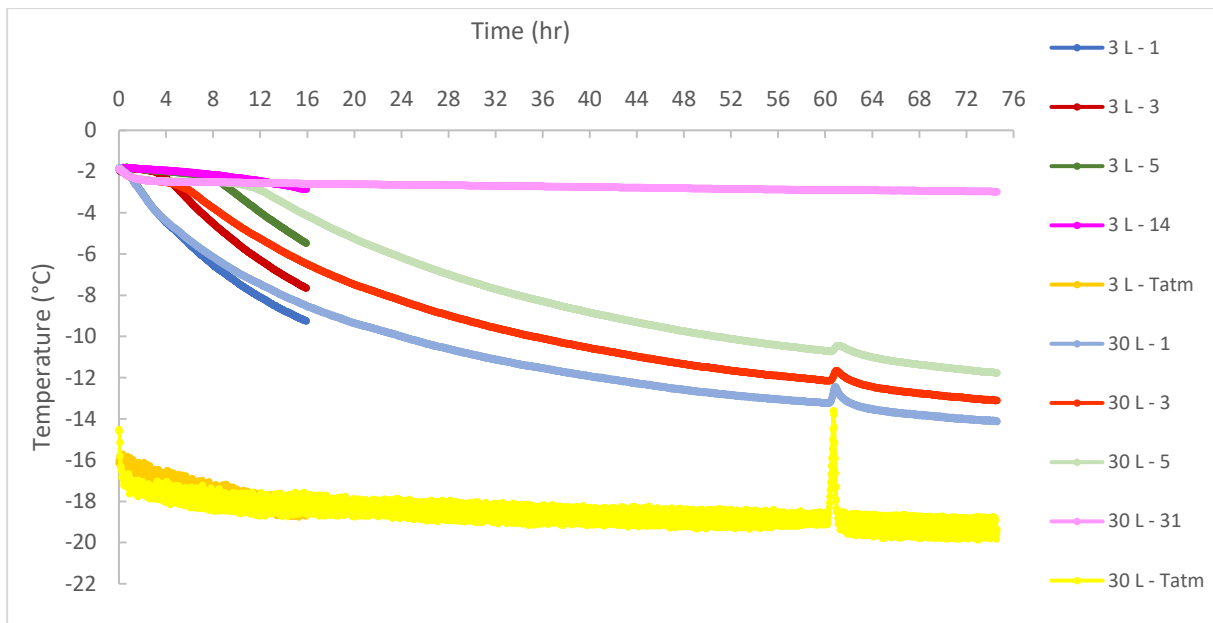


Figure C. 3 Temperature time graphs for ice grown from solutions of starting artificial ocean salinity of 30 psu from a 30 L and 3 L reactor at -20 °C.

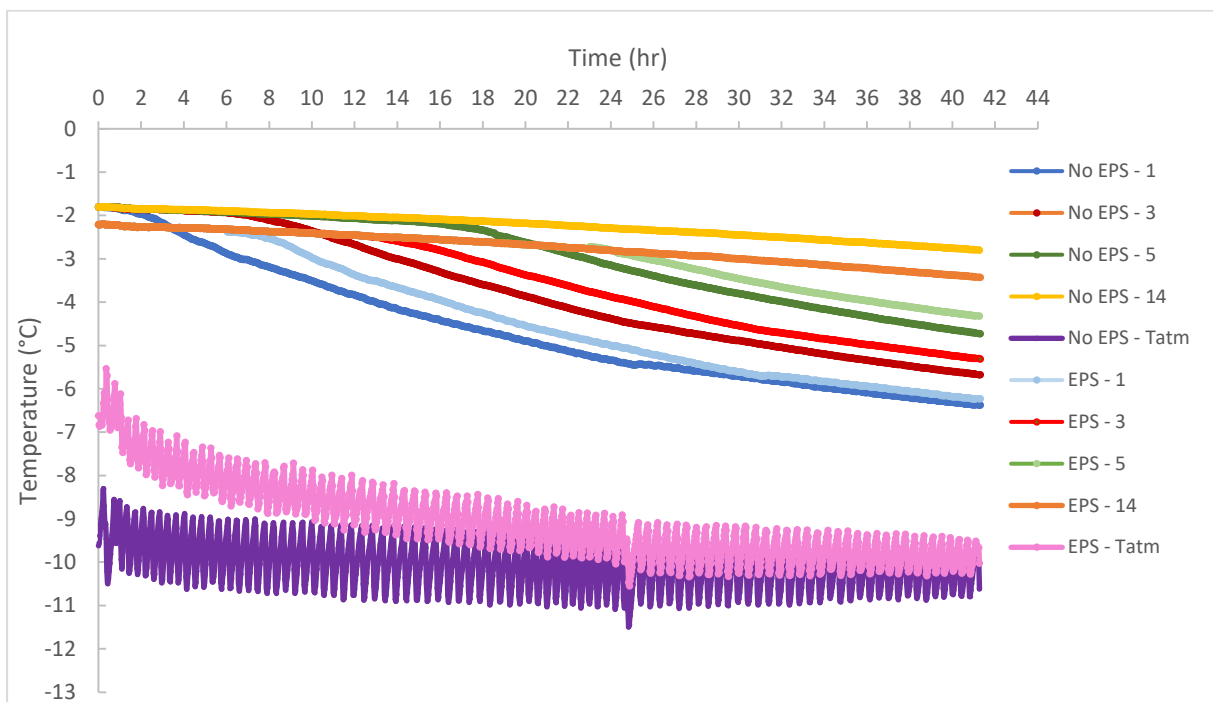


Figure C. 4 Temperature time graphs for ice grown from solutions of starting artificial ocean salinity of 30 psu at -10 °C with and without EPS.

D. Salinity data

Table D. 1 Salinity measurements for ice grown at -10°C from a solution of 10 psu

Depth (cm)	Depth (cm)	Conductivity (mm/s)	Temperature (°C)	Salinity (psu)
0 - 2	2	5.52	17.0	3.579
2 - 4	4	3.80	17.2	2.394
4 - 6	6	4.23	17.4	2.669
6 - 8	8	5.25	17.6	3.344
Salinity underwater		14.120		

Table D. 2 Salinity measurements for ice grown at -10°C from a solution of 20 psu

Depth (cm)	Depth (cm)	Conductivity (mm/s)	Temperature (°C)	Salinity (psu)
0 - 2	2	7.55	17.2	4.980
2 - 4	4	6.49	17.3	4.225
4 - 6	6	7.44	17.5	4.866
6 - 8	9	10.22	17.4	6.862
Salinity underwater		28.179		

Table D. 3 Salinity measurements for ice grown at -10°C from a solution of 30 psu

Depth (cm)	Depth (cm)	Conductivity (mm/s)	Temperature (°C)	Salinity (psu)
0 - 2	2	15.33	17.4	10.637
2 - 4	4	11.09	17.3	7.512
4 - 6	6	11.9	17.1	8.146
6 - 8	9	17.6	17.2	12.419
Salinity underwater		40.6235		

Table D. 4 Salinity measurements for ice grown at -20°C from a solution of 30 psu

Depth (cm)	Depth (cm)	Conductivity (mm/s)	Temperature (°C)	Salinity (psu)
0 - 2	2	25.4	15.3	19.439
2 - 4	4	18.9	16.7	13.587
4 - 6	6	19.82	16.8	14.274
6 - 8	8	22.6	16.5	16.597
8 - 10	9	25.5	16.6	18.896
Salinity underwater		43.750		

Table D. 5 Salinity measurements for ice grown at -5°C from a solution of 30 psu

Depth (cm)	Depth (cm)	Conductivity (mm/s)	Temperature (°C)	Salinity (psu)
0 - 2	2	9.04	16.2	6.194
2 - 4	4	7.4	16.3	4.983
4 - 6	6	10.61	16.3	7.341
Salinity underwater		41.6545		

Table D. 6 Salinity measurements for ice grown at -10°C from a 30 psu solution with EPS

Depth (cm)	Depth (cm)	Conductivity (mm/s)	Temperature (°C)	Salinity (psu)
0 - 2	2	36.2	22.1	24.382
2 - 4	4	34	22.1	22.748
4 - 6	6	32.6	22.2	21.667
6 - 8	8	30.2	22.2	19.915
8 - 10	9	26.0	22.2	16.894
Salinity underwater		31.609		

Table D. 7 Salinity measurements for ice grown from a 30 L reactor at -20°C from a solution of 30 psu

Depth (cm)	Depth (cm)	Conductivity (mm/s)	Temperature (°C)	Salinity (psu)
First sample				
0 – 3	3	15.37	17.7	10.589
4 - 6	6	13.77	17.8	9.377
7 – 9	9	13.69	17.8	9.318
10 - 12	12	13.45	17.6	9.186
13 - 15	15	14	17.6	9.594
16 - 18	18	18	17.31	12.692
Second Sample				
0 – 3	3	18.55	18.3	12.803
4 - 6	6	13.73	18.1	9.280
7 – 9	9	12.83	17.9	8.666
10 - 12	12	13.6	17.8	9.252
13 - 15	15	14.89	18.8	9.963
16 - 18	18	19.66	18.2	13.673
Third Sample				
0 – 3	3	18.22	18.9	12.375
4 - 6	6	12.36	18.1	8.283
7 – 9	9	11.45	17.9	7.663
10 - 12	12	16.08	18.3	10.961
13 - 15	15	15.43	17.7	10.634
16 - 18	18	14.04	17.4	9.670
Average				
0 – 3	3	17.380	18.3	11.923
4 - 6	6	13.287	18	8.980
7 – 9	9	12.657	17.867	8.549
10 - 12	12	14.377	17.900	9.799
13 - 15	15	14.773	18.033	10.064
16 - 18	18	17.233	17.637	12.0118
Salinity of underwater		39.499		

E. Cross polarisation

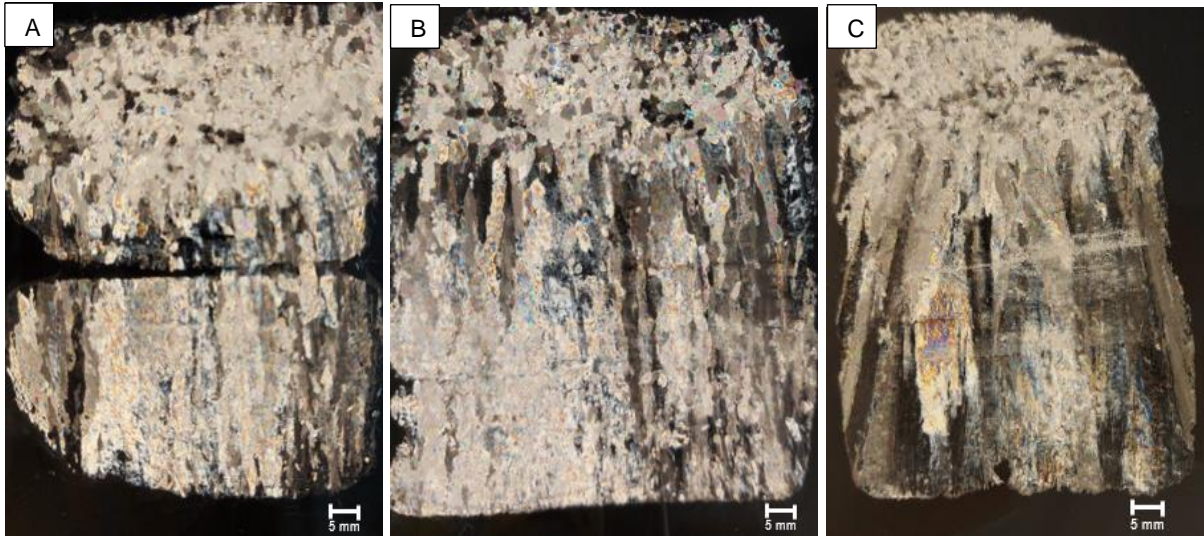


Figure E. 1 Cross polarisation results of samples grown at -10°C from solutions of starting artificial ocean salinities of (A) 10 psu, (B) 20 psu, and (C) 30 psu

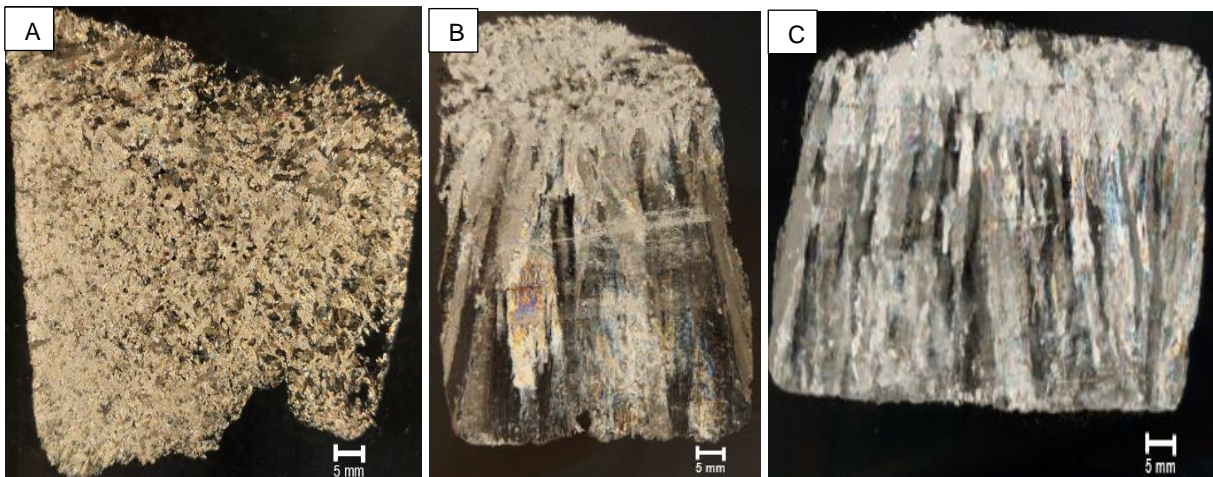


Figure E. 2 Cross polarisation results of samples grown from solutions of starting artificial ocean salinity of 30 psu at (A) -20°C , (B) -10°C , and (C) -5°C



Figure E. 3 Cross polarisation results of samples grown at -20°C from solutions of starting artificial ocean salinity of 30 psu from a (A) 3 L and (B) 30 L reactor.

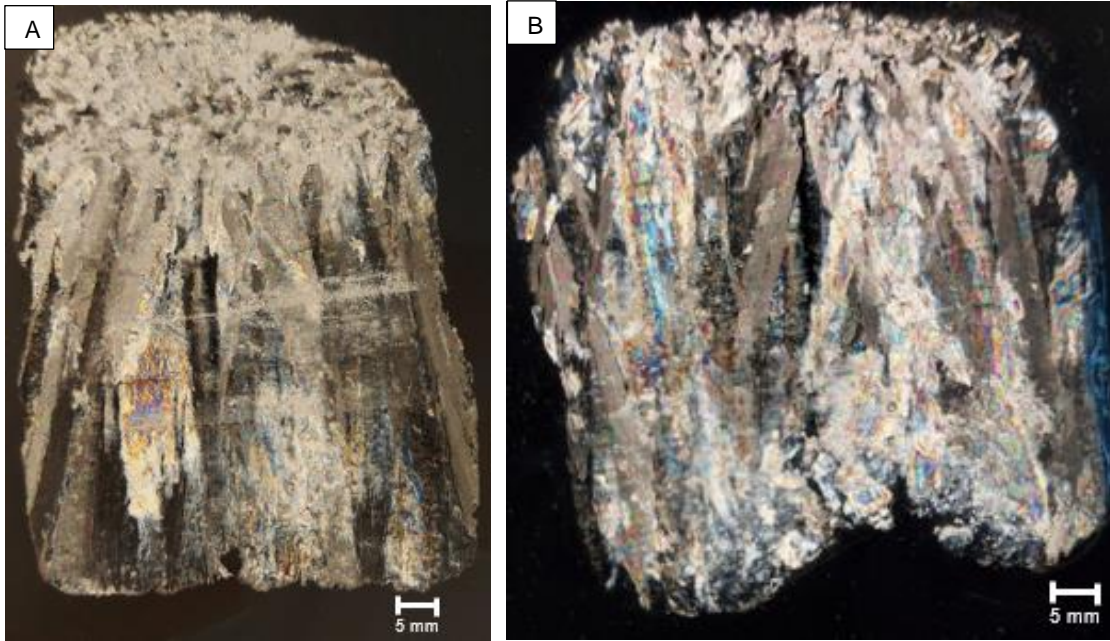


Figure E. 4 Cross polarisation results of samples grown from solutions of starting artificial ocean salinity of 30 psu at -10°C (A) with and (B) without EPS

F. CT scans

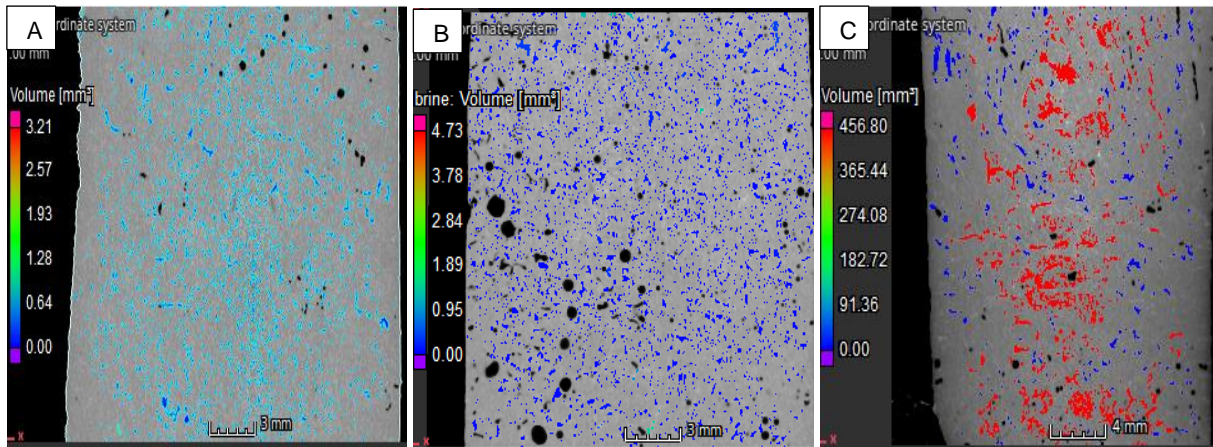


Figure F. 1 Micro-CT scan visuals for the top part of ice grown at -10°C from solutions of starting artificial ocean salinities of (A) 10 psu, (B) 20 psu, and (C) 30 psu.

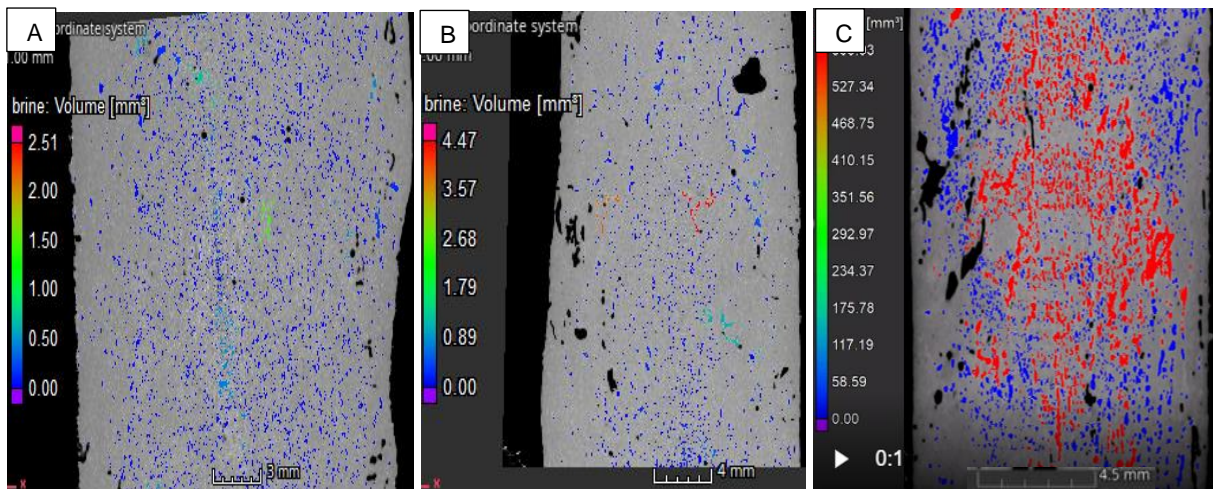


Figure F. 2 Micro-CT scan visuals for the bottom part of ice grown at -10°C from solutions of starting artificial ocean salinities of (A) 10 psu, (B) 20 psu, and (C) 30 psu.

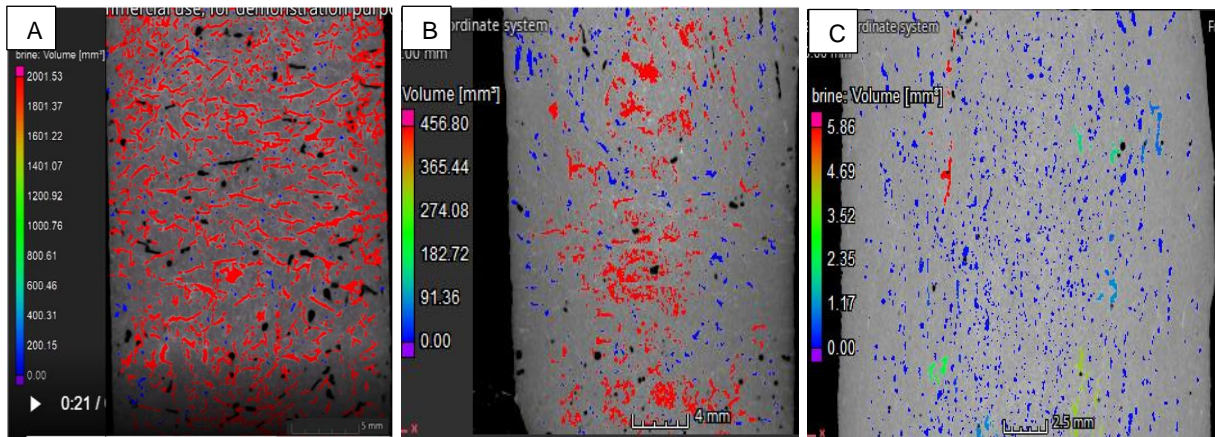


Figure F. 3 Micro-CT scan visuals for the top part of ice grown from solutions of starting artificial ocean salinity of 30 psu at (A) -20°C , (B) -10°C , and (C) -5°C

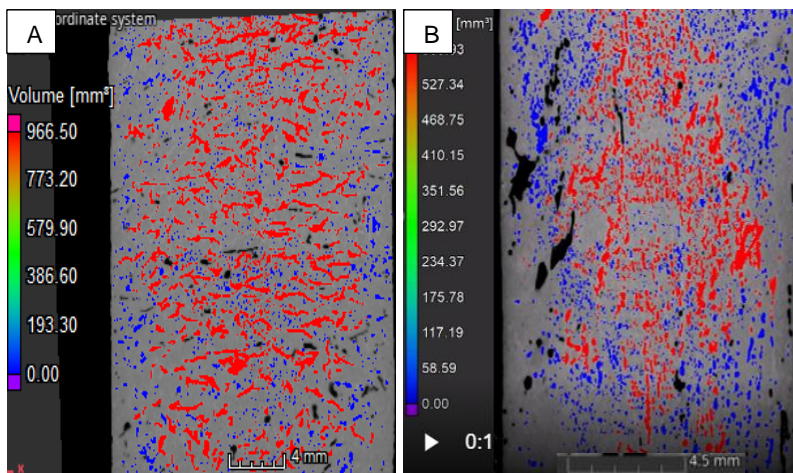


Figure F. 4 Micro-CT scan visuals for the bottom part of ice grown from solutions of starting artificial ocean salinity of 30 psu at (A) -20°C and (B) -10°C .

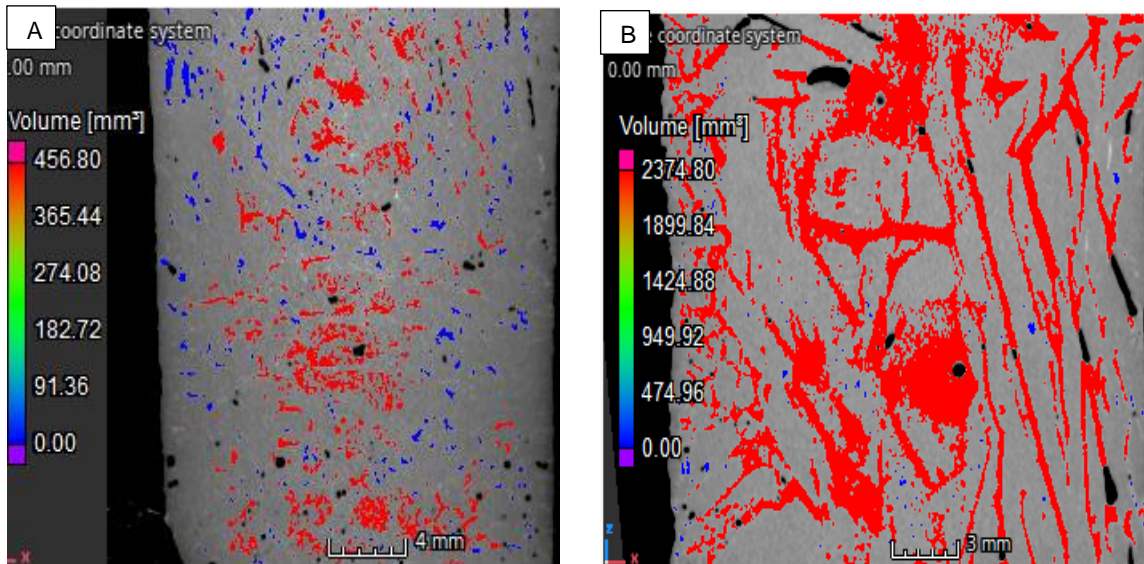


Figure F. 5 Micro-CT scan visuals for the top part of ice grown at -10°C from solutions of starting artificial ocean salinity of 30 psu (A) without EPS, (B) with EPS

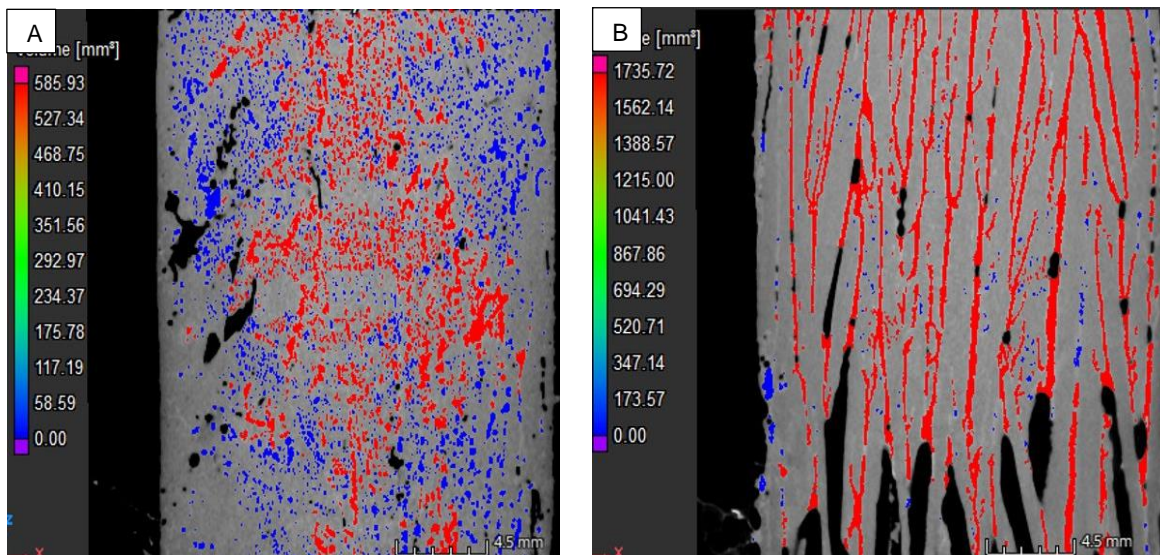


Figure F. 6 Micro-CT scan visuals for the bottom part of ice grown at -10°C from solutions of starting artificial ocean salinity of 30 psu (A) without EPS, (B) with EPS

G. Calculations with Frankenstein & Garner equations

Table G. 1 Definitions of variables used in the calculations of brine, air and ice volume

Values from Cox and Weeks (19983)		
Definitions	Value	Unit
T = ambient or atmospheric temperature		°C
S _i = bulk sea ice salinity		psu
ρ _{ice} = bulk density	926	kg/m ³
S _b = brine salinity		psu
ρ _b = brine density		kg/m ³
V _b = brine volume		
V _b /V = brine specific volume		
V _i /V = ice specific volume		
V _a /V = air specific volume		

Table G. 2 Equations used to calculate the artificial sea ice brine volume developed by Frankenstein and Garner (1967)

Equation	Boundary Limits
$v = S\left(\frac{52.56}{\theta} - 2.28\right)$	$-0.5\text{ }^{\circ}\text{C} \leq \theta \leq -2.06\text{ }^{\circ}\text{C}$
$v = S\left(\frac{45.917}{\theta} - 0.930\right)$	$-2.06\text{ }^{\circ}\text{C} \leq \theta \leq -8.2\text{ }^{\circ}\text{C}$
$v = S\left(\frac{43.795}{\theta} - 1.189\right)$	$-8.2\text{ }^{\circ}\text{C} \leq \theta \leq -22.9\text{ }^{\circ}\text{C}$
$v = S\left(\frac{49.185}{\theta} - 0.532\right)$	$-0.5\text{ }^{\circ}\text{C} \leq \theta \leq -22.9\text{ }^{\circ}\text{C}$

Where v is the brine volume

S is the salinity of ice

θ is the ice temperature

Table G. 3 Equations used in Table G. 5 for brine, air and ice volume calculations

Equations (Cox and Weeks, 1983)	Quantity calculated	Assumption
$S_i = k_{eff} S_{wi}$	Normalised salinity of ice	
$\rho_b = 1000 + 0.85S_b$ (psu)	Density of brine	
$\rho_i = 926 - 1.403 T$ (°C)	Density of ice	
$\frac{V_b}{V} = \frac{\rho S_i}{\rho_b S_b}$	Relative volume of brine	
$F_3(T) = a_3 + b_3 T + c_3 T^2 + d_3 T^3$	Salinity of brine	No solid salts
$\frac{V_i}{V} = \frac{\rho}{\rho_i} - \frac{\rho_b V_b}{\rho_i V}$	Relative volume of pure ice	
$\frac{V_a}{V} = 1 - \frac{V_i}{V} - \frac{V_b}{V}$	Relative volume of air/gas	
$\frac{1}{S_b} = 1 - \frac{54.11}{T}$	Salinity of brine from FG	

Table G. 4 Constants used for calculating $F_3(T)$, the constant used for brine volume calculation (Cox and Weeks, (1982))

	a_3	b_3	c_3	d_3	
$0 \geq T > -2$ °C		-0.03	-18.38	0.33	0.21
-2 °C $\geq T \geq -22.9$ °C		-3.99	-22.70	-1.00	-0.02
-22.9 °C $> T \geq -30$ °C		206.24	-1.89	-0.06	0.00

Table G. 5 The illustration of normalising bulk sea ice salinities (Cox and Weeks, 1988)

	Growth rate (v) (cm/h)					Growth rate (v) (cm/h)					
	3 L			30 L		3 L			30 L		
	10 psu	20 psu	30 psu			10 psu	20 psu	30 psu			
	No EPS	No EPS	No EPS	EPS	No EPS	No EPS	No EPS	No EPS	EPS	No EPS	
-20°C			0.45		0.33	-20°C			1.3E-04		9.2E-05
-10°C	0.33	0.33	0.22	0.33		-10°C	9.2E-05	9.2E-05	6.1E-05	9.2E-05	
-5°C			0.1			-5°C			2.8E-05		
	K_{eff}					$S_i = K_{eff} * S_w$					
	3 L			30 L		3 L			30 L		
	10 psu	20 psu	30 psu			10	20	30			
	No EPS	No EPS	No EPS	EPS	No EPS	psu	No EPS	No EPS	No EPS	EPS	No EPS
-20°C			0.38		0.36	-20°C			11.46		10.93
-10°C	0.36	0.36	0.34	0.36		-10°C	3.64	7.29	10.24	10.93	
-5°C			0.20			-5°C			5.90		

Table G. 6 The table used to calculate the brine, air and ice volume for ice grown at -10°C from an artificial ocean salinity of 10 psu (Cox and Weeks, 1982)

T	S _i (for 10 psu ice)	S _b (FG)	ρ_{ice}	S _b (C&W)	V _b (FG)	ρ_b (C&W)	V _b (FG)	S _b (F3(T))	V _b /V	V _{ice} /V	V _{air} /V	V _b	V _{ice}	V _{air}
°C	psu	psu	kg/m ³	corrected		kg/m ³		psu	(C&W)	(C&W)	(C&W)			
-2	3.64	0.036	926.281	33.017	84.035	1031.927	0.081	37.562	0.087	0.903	0.010	8.696	90.282	1.022
-4	3.64	0.069	926.561	63.780	44.181	1061.252	0.042	72.061	0.044	0.949	0.007	4.408	94.891	0.701
-6	3.64	0.100	926.842	92.515	30.897	1085.395	0.028	100.464	0.031	0.963	0.006	3.091	96.289	0.620
-8	3.64	0.129	927.122	119.417	24.255	1105.170	0.022	123.729	0.025	0.969	0.006	2.465	96.941	0.594
-10	3.64	0.156	927.403	144.658	20.269	1121.392	0.018	142.814	0.021	0.973	0.006	2.105	97.304	0.592
Average		0.098	926.842	90.677	40.727	1081.027	0.038	95.326	0.042	0.951	0.007	3.017	96.356	0.627

Table G. 7 The table used to calculate the brine, air and ice volume for ice grown at -10°C from an artificial ocean salinity of 20 psu (Cox and Weeks, 1982)

T	S _i (for 20 psu ice)	S _b (FG)	ρ_{ice}	S _b (C&W)	V _b (FG)	ρ_b (C&W)	V _b (FG)	S _b (F3(T))	V _b /V	V _{ice} /V	V _{air} /V	V _b	V _{ice}	V _{air}
°C	psu	psu	kg/m ³	corrected		kg/m ³		psu	(C&W)	(C&W)	(C&W)			
-2	7.29	0.036	926.281	33.017	168.301	1031.927	0.163	37.562	0.174	0.806	0.020	17.416	80.567	2.017
-4	7.29	0.069	926.561	63.780	88.484	1061.252	0.083	72.061	0.088	0.898	0.013	8.827	89.829	1.344
-6	7.29	0.100	926.842	92.515	61.879	1085.395	0.057	100.464	0.062	0.927	0.011	6.191	92.659	1.150
-8	7.29	0.129	927.122	119.417	48.576	1105.170	0.044	123.729	0.049	0.940	0.011	4.937	93.994	1.069
-10	7.29	0.156	927.403	144.658	40.594	1121.392	0.036	142.814	0.042	0.948	0.010	4.215	94.752	1.033
Average		0.098	926.842	90.677	81.567	1081.027	0.077	95.326	0.083	0.904	0.013	6.042	92.809	1.149

Table G. 8 The table used to calculate the brine, air and ice volume for ice grown at -10°C from an artificial ocean salinity of 30 psu (Cox and Weeks, 1982)

T	S _i (for 30 psu ice)	S _b (FG)	ρ_{ice}	S _b (C&W)	V _b (FG)	ρ_b (C&W)	V _b FG	S _b (F3(T))	V _b /V	V _{ice} /V	V _{air} /V	V _b	V _{ice}	V _{air}
°C	psu	psu	kg/m ³	corrected		kg/m ³		psu	(C&W)	(C&W)	(C&W)			
-2	10.24	0.036	926.281	33.017	236.406	1031.927	0.229	37.562	0.245	0.727	0.028	24.463	72.716	2.820
-4	10.24	0.069	926.561	63.780	124.291	1061.252	0.117	72.061	0.124	0.857	0.019	12.399	85.738	1.863
-6	10.24	0.100	926.842	92.515	86.919	1085.395	0.080	100.464	0.087	0.897	0.016	8.696	89.726	1.578
-8	10.24	0.129	927.122	119.417	68.233	1105.170	0.062	123.729	0.069	0.916	0.015	6.934	91.613	1.453
-10	10.24	0.156	927.403	144.658	57.021	1121.392	0.051	142.814	0.059	0.927	0.014	5.921	92.689	1.390
Average		0.098	926.842	90.677	114.574	1081.027	0.108	95.326	0.117	0.865	0.018	8.488	89.941	1.571

Table G. 9 The table used to calculate the brine, air and ice volume for ice grown at -20°C from an artificial ocean salinity of 30 psu (Cox and Weeks, 1982)

T °C	S _i (for -20°C ice) psu	S _b (FG) psu	ρ_{ice} kg/m ³	S _b (C&W) corrected	V _b (FG)	ρ_b (C&W) kg/m ³	V _b (FG)	S _b (F3(T)) psu	V _b /V (C&W)	V _{ice} /V (C&W)	V _{air} /V (C&W)	V _b	V _{ice}	V _{air}
-2	11.46	0.036	926.281	33.017	264.571	1031.927	0.256	37.562	0.274	0.695	0.032	27.378	69.469	3.153
-4	11.46	0.069	926.561	63.780	139.099	1061.252	0.131	72.061	0.139	0.840	0.021	13.876	84.046	2.078
-6	11.46	0.100	926.842	92.515	97.274	1085.395	0.090	100.464	0.097	0.885	0.018	9.732	88.513	1.756
-8	11.46	0.129	927.122	119.417	76.362	1105.170	0.069	123.729	0.078	0.906	0.016	7.761	90.628	1.611
-10	11.46	0.156	927.403	144.658	63.815	1121.392	0.057	142.814	0.066	0.918	0.015	6.626	91.836	1.537
-12	11.46	0.182	927.684	168.389	55.450	1134.874	0.049	158.676	0.059	0.926	0.015	5.893	92.609	1.498
-14	11.46	0.206	927.964	190.743	49.475	1146.432	0.043	172.273	0.054	0.932	0.015	5.373	93.150	1.477
-16	11.46	0.228	928.245	211.837	44.994	1156.879	0.039	184.564	0.050	0.936	0.015	4.970	93.564	1.466
-18	11.46	0.250	928.525	231.777	41.509	1167.029	0.036	196.505	0.046	0.939	0.015	4.627	93.912	1.461
-20	11.46	0.270	928.806	250.656	38.720	1177.698	0.033	209.056	0.043	0.942	0.015	4.310	94.233	1.457
Average		0.162	927.543	150.679	87.127	1118.805	0.080	139.770	0.091	0.892	0.017	7.019	91.388	1.593

Table G. 10 The table used to calculate the brine, air and ice volume for ice grown at -10°C from an artificial ocean salinity of 30 psu (Cox and Weeks, 1982)

T °C	S _i (for -10°C ice) psu	S _b (FG) psu	ρ_{ice} kg/m ³	S _b (C&W) corrected	V _b (FG)	ρ_b (C&W) kg/m ³	V _b (FG)	S _b (F3(T)) psu	V _b /V (C&W)	V _{ice} /V (C&W)	V _{air} /V (C&W)	V _b	V _{ice}	V _{air}
-2	10.24	0.036	926.281	33.017	236.406	1031.927	0.229	37.562	0.245	0.727	0.028	24.463	72.716	2.820
-4	10.24	0.069	926.561	63.780	124.291	1061.252	0.117	72.061	0.124	0.857	0.019	12.399	85.738	1.863
-6	10.24	0.100	926.842	92.515	86.919	1085.395	0.080	100.464	0.087	0.897	0.016	8.696	89.726	1.578
-8	10.24	0.129	927.122	119.417	68.233	1105.170	0.062	123.729	0.069	0.916	0.015	6.934	91.613	1.453
-10	10.24	0.156	927.403	144.658	57.021	1121.392	0.051	142.814	0.059	0.927	0.014	5.921	92.689	1.390
Average		0.098	926.842	90.677	114.574	1081.027	0.108	95.326	0.117	0.865	0.018	6.428	92.151	1.421

Table G. 11 The table used to calculate the brine, air and ice volume for ice grown at -5°C from an artificial ocean salinity of 30 psu (Cox and Weeks, 1982)

T	S _i (for -5°C ice)	S _b (FG)	ρ_{ice}	S _b (C&W)	V _b (FG)	ρ_b (C&W)	V _b (FG)	S _b (F3(T))	V _b /V	V _{ice} /V	V _{air} /V	V _b	V _{ice}	V _{air}
°C	psu	psu	kg/m ³	corrected		kg/m ³		psu	(C&W)	(C&W)	(C&W)			
-2	5.9	0.036	926.281	33.017	136.210	1031.927	0.132	37.562	0.141	0.843	0.016	14.095	84.267	1.638
-4	5.9	0.069	926.561	63.780	71.613	1061.252	0.067	72.061	0.071	0.918	0.011	7.144	91.757	1.099
-6	5.9	0.100	926.842	92.515	50.080	1085.395	0.046	100.464	0.050	0.940	0.009	5.010	94.042	0.948
-8	5.9	0.129	927.122	119.417	39.314	1105.170	0.036	123.729	0.040	0.951	0.009	3.995	95.116	0.888
-10	5.9	0.156	927.403	144.658	32.854	1121.392	0.029	142.814	0.034	0.957	0.009	3.411	95.724	0.865
Average		0.098	926.842	90.677	66.014	1081.027	0.062	95.326	0.067	0.922	0.011	6.731	92.181	1.088

Where

S_b is the brine salinity

S_i is the ice salinity

ρ_b and ρ_i are the densities of brine and ice respectively

V_b/V is the relative brine volume

V_i/V is the relative ice volume

V_a/V is the relative air volume

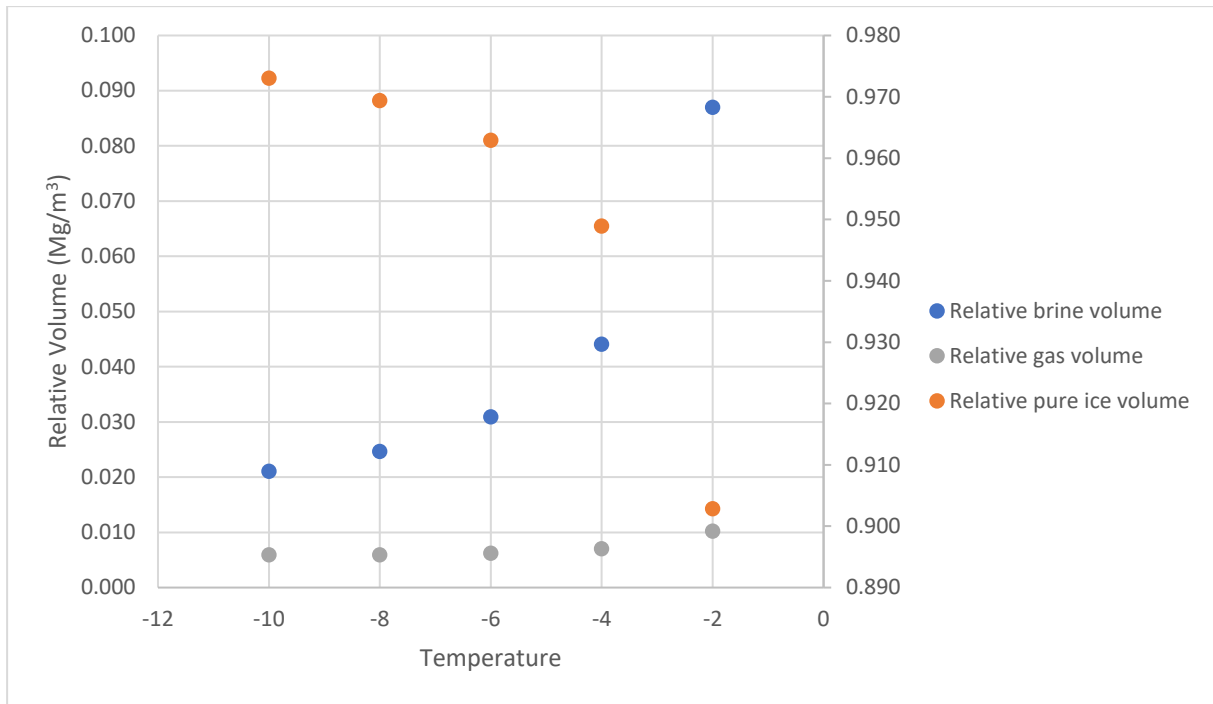


Figure G. 1 Graph showing the relationship between the relative volume of brine, air, and ice generated as per the values inputted in the Table G. 6.

Table G. 12. Data for overall porosity of artificial sea ice for varying starting artificial ocean salinity computed from FG equations and ct-scan data

	10 psu		20 psu		30 psu	
	CT	FG	CT	FG	CT	FG
Air	0.299	0.592	1.556	1.033	1.280	1.390
Brine	1.285	2.105	1.478	4.215	5.327	5.921
Overall porosity	1.584	2.696	3.034	5.248	6.607	7.311

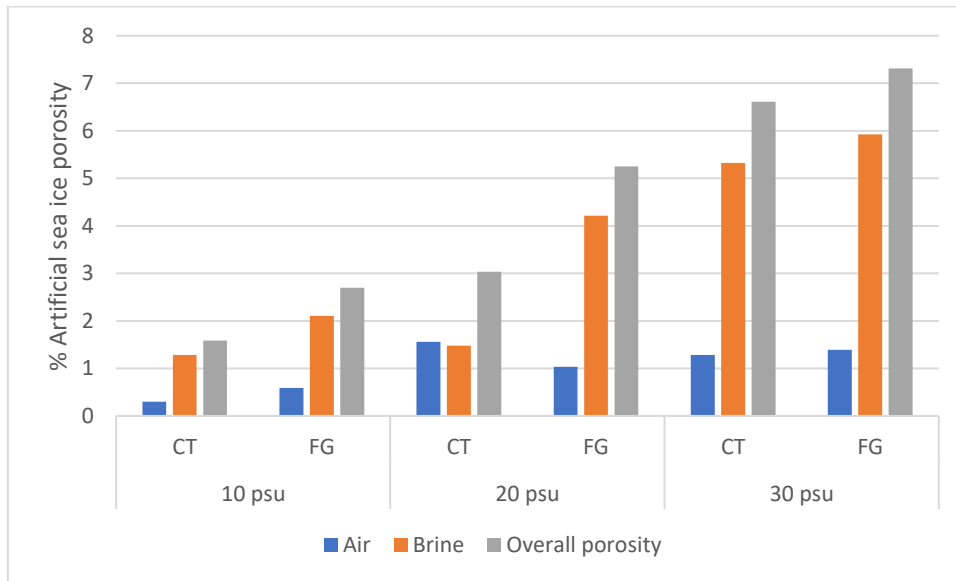


Figure G. 2 Graph of overall porosity of artificial sea ice for varying starting artificial ocean salinity computed from FG equations and CT-scan data.

Table G. 13 Data for overall porosity of artificial sea ice for varying ambient temperature computed from FG equations and CT-scan data.

	-20°C		-10°C		-5°C	
	CT	FG	CT	FG	CT	FG
Air	1.627	1.593	1.280	1.421	0.221	1.023
Brine	8.581	7.019	5.327	6.428	1.438	6.077
Overall porosity	10.208	8.612	6.607	7.849	1.658	7.101

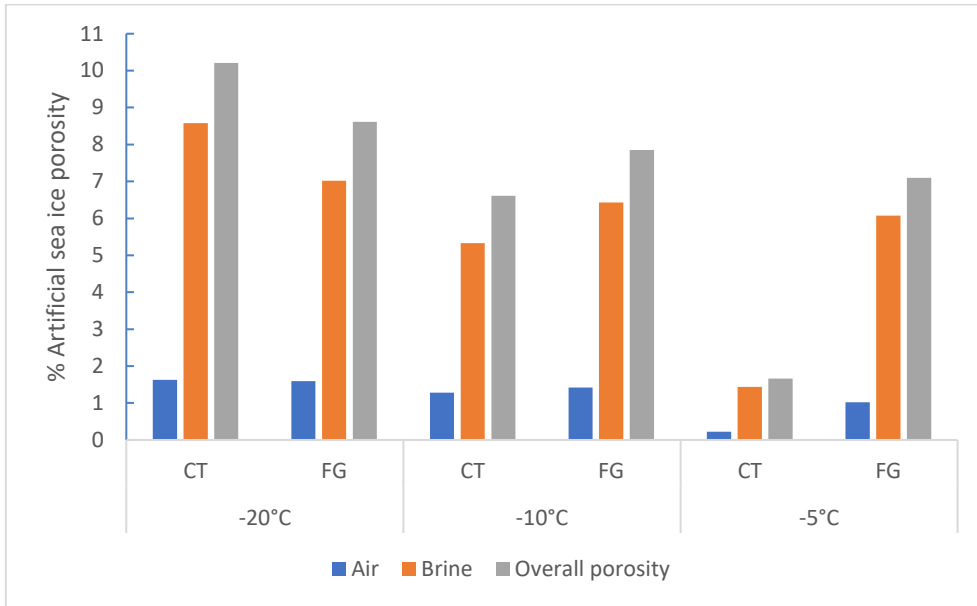


Figure G. 3 Graph of overall porosity of artificial sea ice for varying ambient temperature computed from FG equations and CT-scan data